Pro Gradu
Meteorology

Analysis of different radiation parameters and their comparison to cloud occurrence at the SMEAR II station

Salla Sillanpää

22.10.2018

Supervisors: Ditte Taipale, Ph.D.
Risto Taipale, Ph.D.

Examiners: Markku Kulmala, Prof.
Ekaterina Ezhova, Ph.D.

University of Helsinki

Institute of Atmospheric and Earth System Research

PL 64 (Gustaf Hällströmin katu 2a)

00014 Helsingin yliopisto

Tiedekunta – Fakultet – Faculty **Faculty of Science**	Laitos – Institution – Department Oppiaine – Läröämne – Subject **Institute for Atmospheric and Earth System Research** **Meteorology**	
Tekijä – Författare – Author **Salla Sillanpää**		
Työn nimi – Arbetets titel – Title **Analysis of different radiation parameters and their comparison to cloud occurrence at the SMEAR II station**		
Työn laji – Arbetets art – Level **Pro Gradu**	Aika – Datum – Month and year **October 2018**	Sivumäärä – Sidantal – Number of pages **78**

Tiivistelmä – Referat – Abstract

This study is an analysis of the different radiation parameters measured at SMEAR II station in Hyytiälä, Finland. The measurements include global radiation, diffuse shortwave radiation, reflected shortwave radiation, net radiation, photosynthetically active radiation (PAR), diffuse PAR, reflected PAR, ultraviolet-A (UV-A), ultraviolet-B (UV-B) radiation, incoming and outgoing infrared (IR) radiation and PAR below canopy measurements. Annual and inter-annual variations in different radiation parameters are investigated alongside dependencies and changes in relationships between different radiation variables. The changes in the different radiation parameters are compared to changes in the cloud occurrence at the measurement station. The cloud occurrence is based on cloud base height measurements from a ceilometer.

The monthly median values of the parameters and ratios of parameters investigated in this study did not show any statistically significant trends. Annual and seasonal variation were detected for both individual parameters and ratios of parameters. These variations result from the changes in solar zenith angle, climatic conditions, cloudiness, aerosol load of the atmosphere and surface absorbance/emittance properties.

Avainsanat – Nyckelord – Keywords
radiation, cloud occurrence, SMEAR II station

Säilytyspaikka – Förvaringsställe – Where deposited

Muita tietoja – Övriga uppgifter – Additional information

Contents

Abbreviation	Meaning	Wavelength range
Global radiation	Direct and diffuse solar radiation reaching the surface	0.3-2.8 μm
Diffuse radiation	Solar radiation that has been scattered before reaching the surface	0.3-2.8 μm
PAR	Photosynthetically Active Radiation (visible radiation)	0.4-0.7 μm
UV-A	Ultraviolet-A radiation	0.32-0.42 μm
UV-B	Ultraviolet-B radiation	0.28-0.32 μm
Incoming IR	Incoming infrared radiation	5-50 μm
Outgoing IR	Outgoing infrared radiation	5-50 μm
NIR	Near infrared radiation	0.7-2.8 μm

1. Introduction

Radiation is movement of energy in a form of particle or electromagnetic wave through a medium. All objects emit and absorb radiation including the Sun, the Earth, gas molecules, aerosols and clouds in the atmosphere. The intensity of the emitted radiation spectrum depends on the temperature and absorbance/emittance properties of the emitting object.

Radiation emitted by the Sun is important for life on the Earth as it is the major source of our energy. Solar radiation drives the weather, climate system and sea currents. It forms an electromagnetic spectrum, which covers a wide range of wavelengths from short gamma rays to long radio waves. The most important wavelengths in the energy transfer from the Sun to the Earth are ultraviolet, visible and infrared parts of the spectrum. As the electromagnetic waves travel through the Earth's atmosphere, their properties can be altered due to scattering and emitting processes by clouds, gas molecules, aerosols and dust. These processes can change the direction and wavelength of the initial electromagnetic wave. The orbital geometry between the Sun and the Earth, the composition of the atmosphere and the surface reflectance properties determine how much of the incoming solar radiation is able to reach the Earth's surface. During clear skies most of the incoming solar radiation is able to reach the surface.

Radiation emitted by the Earth's surface, clouds, gas molecules and aerosols has a longer wavelength than solar radiation, because the temperature of the emitting object is lower than the Sun's. Opposite to the transfer of solar radiation, the atmosphere is very opaque to longwave radiation emitted by the Earth's surface and atmosphere. Longwave radiation is absorbed effectively by the greenhouse gases in the atmosphere. Increased anthropogenic emissions of greenhouse gases have enforced the natural greenhouse effect, which has led to the rising surface temperatures. The incoming solar radiation and outgoing longwave radiation emitted by the Earth and atmosphere form the energy budget of the Earth.

Natural variation, climate warming and other anthropogenic effects on the ecosystem have changed and will change the climate system in the future. Analysis of long-term measurements of different radiation parameters can provide us vital information about the Sun's activity and changes occurring in the atmosphere, for example in cloud occurrence and concentrations of different greenhouse gases. Accurate measurements of different radiation parameters are important for different applications in

the society; the increase in UV-B radiation rise the risk of skin cancer and crop losses and visible radiation measurements give important information about the photosynthesis rate.

This study is an analysis of the different radiation parameters measured at SMEAR II station in Hyytiälä, Finland. After the opening of the SMEAR II station in 1995, there have been more than 20 different long-term radiation measurements. The measurements include global radiation, diffuse shortwave radiation, reflected shortwave radiation, net radiation, photosynthetically active radiation (PAR), diffuse PAR, reflected PAR, ultraviolet-A (UV-A), ultraviolet-B (UV-B) radiation, incoming and outgoing infrared (IR) radiation and PAR below canopy measurements. Annual and inter-annual variations in different radiation parameters are investigated alongside dependencies and changes in relationships between different radiation variables.

The changes in the different radiation parameters are compared to changes in the cloud occurrence at the measurement station. The cloud occurrence is based on cloud base height measurements from a ceilometer. Though the horizontal resolution of a ceilometer is narrow, it has been shown in previous studies that cloud occurrence based on ceilometer measurement corresponds well with results retrieved from satellites observations and man-made observation. Because sunlight plays a crucial role in the atmospheric photochemistry, the effect of the changes in the radiation parameters on atmospheric chemistry is discussed briefly. The aim of this study is to find dependencies between different radiation variables and study if the measured radiation parameters have changed over the years.

2. Scientific background

2.1 The Sun

2.1.1 Orbital geometry

The Earth circles around the Sun in an elliptical orbit with the mean distance of $1.496 \cdot 10^8$ km, or one astronomical unit (AU). The Earth reaches its furthest distance (~1.017 AU) from the Sun around the 4th of July. This point is called aphelion. The closest point to the Sun is called perihelion (~0.983 AU) and it is reached around the 3rd of January. The amount of incoming radiation is inversely proportional to the square of the distance between the Earth and the Sun. As a result, the incoming solar radiation varies $\pm$ 3.5 % between perihelion and aphelion (Iqbal, 1983).
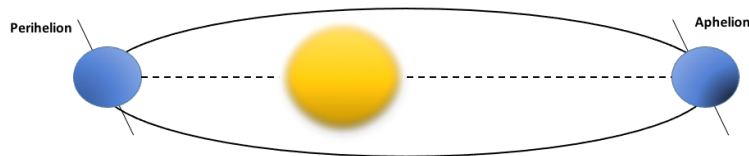

Figure 1 The relative position of the Earth to the Sun during different points of the orbit . Because the Earth's orbit around the Sun is slightly eccentric, the radiation income is smaller in July, when the Earth reaches its furthest distance from the Sun (aphelion) than in January when the Earth is closest to the Sun (perihelion).

At the same time as the Earth circles around the Sun, it also rotates around its own polar axis. Polar axis is an imaginary line between geographical north and south pole. As is illustrated in Figure 1, there is tilt of approximately 23.45° between the axis of rotation and the normal to the plane of the orbit. The tilt affects the radiation income especially at higher latitudes. The tilt of the polar axis and the Earth's relative distance from the Sun are the main reasons for seasonal changes in the amount of solar radiation (Hartmann, 2016). The rotation around the Earth's own axis causes the diurnal changes in the insolation.

2.1.2 Radiation emitted by the Sun

Blackbody is an ideal emitter and absorber of radiation. According to blackbody approximation an object emits the maximum amount of radiation at each wavelength into all directions. The shape and the intensity of the emitted spectrum depends on the temperature of the object. Blackbody approximation assumes also that the object absorbs all the incoming radiation at all wavelengths

(Iqbal, 1983). The emissive power $F(\lambda)$ of a blackbody is dependent on temperature T and wavelength λ and can be calculated with Stefan-Boltzmann law:

$$F(\lambda) = \frac{2\pi c^2 h \lambda^{-5}}{e^{ch/k\lambda T} - 1}$$ [1]

where $c = 2.997 \cdot 10^8$ ms^{-1} is the speed of the light, $h = 6.625 \cdot 10^{-34}$ J s is the Planck constant and $k = 1.380 \cdot 10^{-23}$ J K^{-1} is the Boltzmann constant. The Sun can be approximated as a blackbody. The average temperature at which the Sun emits electromagnetic radiation is around 5800 K. This is the average temperature of the photosphere, the outer most layer of the Sun. When integrating over all the wavelengths, the radiative flux density F can be calculated as

$$F = \sigma T^4 = 5.67 \cdot 10^{-8} \text{ Wm}^{-2}\text{K}^{-4} \cdot (5800 \text{ K})^4 = 6.4 \cdot 10^7 \text{ Wm}^{-2}$$ [2]

where σ is the Stefan-Boltzmann constant and T is temperature in Kelvin units (Liou, 2002). When the radiative flux density is received on a surface, it is called irradiance. The total energy flux density emitted by the Sun can be calculated by multiplying energy flux density per unit area with the area of the Sun

$$P = FA_{\text{Sun}} = 6.4 \cdot 10^7 \text{ Wm}^{-2} \cdot 6.09 \cdot 10^{18} \text{ m}^2 = 3.9 \cdot 10^{26} \text{ W}$$ [3]

The electromagnetic radiation emitted by the Sun spreads into the space spherically. The amount of radiation a perpendicular surface located $1.496 \cdot 10^8$ km (the average distance between the Earth and the Sun) from the Sun receives approximately, can be obtained from the following equation:

$$S_0 = \frac{P}{4\pi d^2} = 1361 \text{ Wm}^{-2}$$ [4]

where P is the total energy flux density and d is the average distance between the Earth and the Sun. S_0 is called the solar constant. Because the distance between the Earth and the Sun is much greater than the diameter of the Earth, the solar radiation is basically an uniform parallel beam (Hartmann, 2016). The amount of radiation the Earth receives at a certain moment is the same amount that a perpendicular circle surface with same radius and distance from the Sun as the Earth would receive. Because the area of the Earth ($4\pi a^2$) differs from the area of the perpendicular surface (πa^2), incoming radiation received by a round surface needs to be divided with the area of the Earth

$$\frac{\pi a^2 S_0}{4\pi a^2} = \frac{S_0}{4} \approx 340 \text{ Wm}^{-2}$$ [5]

This is the average amount of radiation coming to a unit area at the top of the atmosphere. In reality, due to the Earth's spherical figure the radiation is unevenly distributed over the globe and the receiving surface is often inclined with the solar beam. Because the radiation is spread over a wider region, the amount of radiation coming to a unit area is smaller than the value given by solar constant (Hartmann, 2016). The amount of radiation income at a specific point at the top of the atmosphere can be calculated with the following equation

$$Q_s = \begin{cases} S_0 (\frac{\bar{d}}{d})^2 \sin(\beta) & \text{when } \beta > 0 \\ 0 & \text{during other times} \end{cases} \qquad [6]$$

where S_0 is the solar constant, $\bar{d}$ is the mean distance between the Earth and the Sun, d is the actual distance at the moment and β is the solar zenith angle. The solar zenith angle can be obtained with the following equation

$$\sin(\beta) = \sin(\phi)\sin(\delta) + \cos(\phi)\cos(\delta)\cos(\alpha) \qquad [7]$$

where ϕ is the latitude, δ is the declination angle and α is the hour angle. Declination angle changes along the seasons. It can get values from +23.5° (northern summer solstice) to -23.5° (northern winter solstice). The hour angle, according to its name, depends on the hour of the day. α is 0° at noon and grows to 180° by midnight. Solar radiation coming to a specific point at the top of the atmosphere depends on the time of the day, season and latitude (Hartmann, 2016). Figure 2 shows the radiation
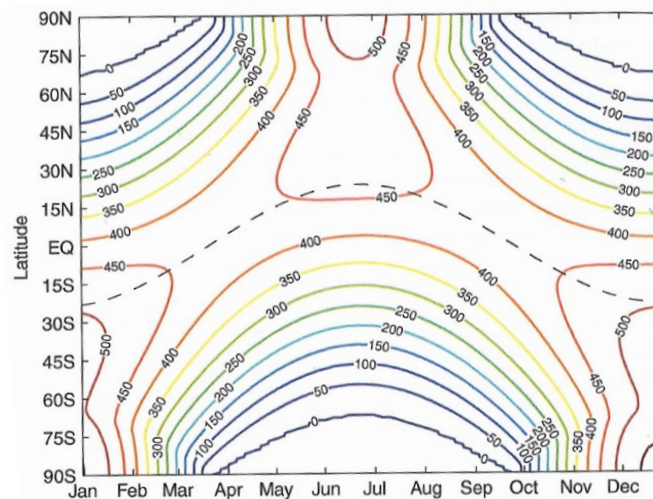

Figure 2 The average radiation income to the top of the atmosphere according to different months and latitudes in units Wm^{-2}. The dashed line shows the location of the point that is directly under the Sun at noon (Hartmann, 2016) .

income at the top of the atmosphere for different latitudes during different months. The figure shows maximum amount of radiation coming to poles during summer time. This is due to long hours of sunshine.

2.1.3 Electromagnetic spectrum

The electromagnetic radiation coming from the Sun to the Earth can be presented as a particle or as an electromagnetic wave that moves energy through the space. Electromagnetic radiation travels through the space with the speed of light, and almost with the same speed when they travel in the atmosphere. Radiation is emitted from the emitter when an electron is dropped to lower level of energy. The energy difference between the initial and final condition can be calculated with Planck's law:

$$E=hf \qquad\qquad [8]$$

where E is the energy in Joules, h is Planck's constant and f is the frequency in unit s^{-1}. Frequency describes how many vibrations take place in one second. A molecule can absorb a photon only if the energy of the photon corresponds to the energy difference between two energy levels. For an electromagnetic wave, the frequency can be used to calculate the wavelength λ:

$$\lambda = \frac{c}{f}, \qquad\qquad [9]$$

where c is the speed of the light. Wavelength and frequency are inversely proportional; high frequency corresponds to electromagnetic waves with short wavelength and vice versa (Liou, 2002).

Electromagnetic spectrum describes the electromagnetic radiation as a function of wavelength. It contains a wide range of different size wavelengths from 10^{-5} µm (gamma rays) up to 10^9 µm (radio waves). In the atmosphere the most significant spectral bands in the energy transport are ultraviolet, visible and infrared radiation bands (Hartmann, 2016). Approximately 99 % of the total insolation comes as infrared (0.7-5 µm) or visible radiation (0.4-0.7 µm). Even though ultraviolet radiation (0.28-0.42 µm) is responsible for less than one percent, it has a crucial role as ultraviolet radiation can be harmful to life on the Earth and it affects the atmospheric chemistry in the stratosphere.

The wavelength at which the maximum amount of radiation is emitted by a blackbody can be calculated with Wien's law:

$$\lambda_{\text{max}} = \frac{2.897 \cdot 10^6 \, \text{nm} \cdot \text{K}}{T} \qquad\qquad [10]$$

where *T* is the average temperature in Kelvin units of the emitting object. The wavelength is given in nanometres. For the Sun, the wavelength at which the maximum amount of radiation is emitted is found in the visible part of the spectrum around 500 nm (Seinfeld & Pandis, 2016).

2.1.4 Changes in the solar radiation intensity

Occasionally areas of low temperature appear on the surface of the Sun. These areas are called sunspots. They appear as black, because of their relatively low temperature. The normal energy flow in the sunspot area is disturbed by changes in the magnetic field (Hartmann, 2016). Size and duration of an individual sunspot varies greatly. The periodic change in the amount of sunspots on the surface of the Sun is called sunspot cycle. The average cycle lasts approximately 11 years, which is the time between two sunspot maxima (Liou, 2002). The sunspot cycle is a result of the changes in locations of the poles of the Suns magnetic field. Every 11 years the south and north pole of the Sun's magnetic field change places. The poles are returned to their initial locations during the next 11 years. Figure 3 represents the number of sunspots from year 1993 to 2017.

Sunspots appear on the surface of the Sun at the same time with faculae, which are areas of brighter colour. These areas are relatively warmer and they emit 15 % more radiation than the surroundings. The increased electromagnetic radiation emitted by faculae compensate for the reduced emissions by sunspots. The maximum insolation is observed during the sunspot maxima due to increased emissions by faculae. Previous studies show that sunspots effect the solar constant by approximately 0.1% or 1.5 Wm^{-2} between the maximum and minimum points of sunspot cycle (Kopp & Lean, 2011).
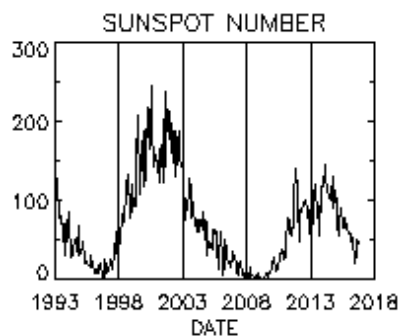
Figure 3 Number of sunspots yearly between 1993 and 2017 (NASA (National Aeronautics and Space Administration), 2017).

During the active sunspot periods solar flares and eruptive prominences can occur. These phenomena increase the amount of gamma-ray, X-ray and ultraviolet radiation. The effect on the total radiation is very small. The effects of sunspot cycle influence the life on the Earth as the increase in ultraviolet radiation affects the chemistry of the atmosphere, especially the stratospheric ozone chemistry. The

last two maxima in sunspot cycle were measured in November 2001 and in April 2014 (NASA (National Aeronautics and Space Administration), 2017). The sunspot number in the latter was clearly lower than in the former one.

2.2 The Earth

Approximately 99.98% of the total energy on the Earth comes from the Sun. The rest comes mainly from geothermal processes (Sellers, 1965). The unevenly distributed solar radiation on the globe drives sea currents, weather phenomena and the climate system.

2.2.1 The Earth's energy budget

While the system consisting of the Earth and the atmosphere receives electromagnetic radiation from the Sun, it also loses energy by emitting thermal infrared radiation back to space (Hartmann, 2016). According to blackbody approximation the warmer the temperature of the emitting surface is, the higher the frequency of the electromagnetic wave and shorter the wavelength is. Because the Earth's surface and atmosphere are much cooler than the Sun, the radiation they emit has a longer wavelength and it is often referred as longwave radiation while solar radiation as shortwave radiation. The emitted radiation is focused on the far infrared wavelength band (3-50 μm).

Figure 4 shows the average energy flows on the Earth. The figure is focused on the energy fluxes from radiation, thus latent heat flux and convective heat transfer are not shown in the figure. Incoming solar radiation is shown with the orange arrows on the left side of the figure. As was mentioned previously, the average amount of insolation at the top of the atmosphere is around 340 Wm^{-2}. Approximately 100 Wm^{-2} out of this incoming radiation is reflected back to space by the Earth's surface, clouds and the atmosphere (Loeb et al., 2009). The fraction of the solar radiation that is reflected back to space is called albedo. The average albedo on the Earth is around 30 % (Vonder Haar & Suomi, 1971). The highest values of albedo are measured in polar regions, where the snow cover, thick clouds and small zenith angles increase the amount of reflected radiation.

The terrestrial radiation is presented with the blue arrows on the right side of Figure 4. Outgoing longwave radiation is dependent on the temperature and absorbance/emitting properties of the emitting surface. The highest values of outgoing radiation are measured in desert and tropical ocean areas, where the surfaces are warm and there are not many clouds blocking the radiation transfer back to space. The lowest values are measured at poles due to the cold surface temperatures (Hartmann, 2016).
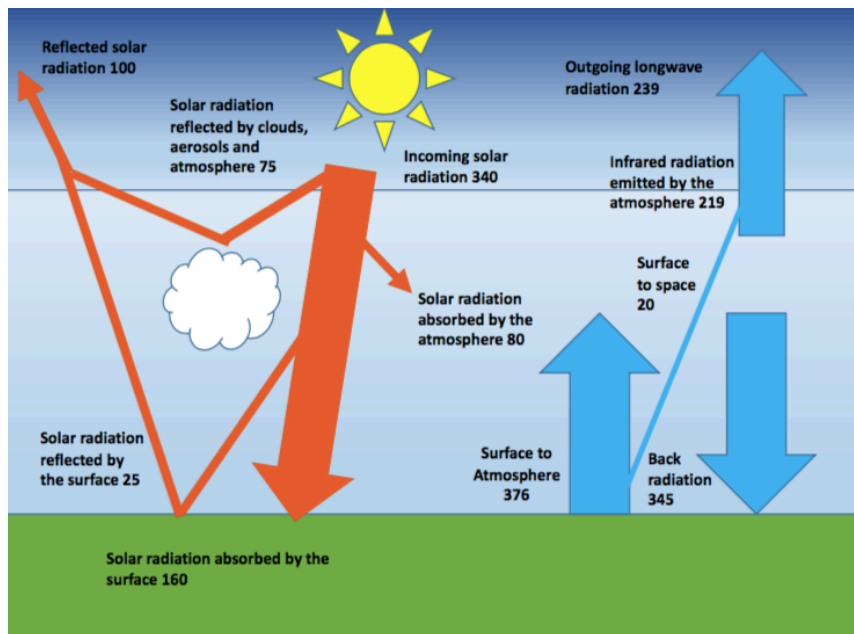
Figure 4 The average energy flows on the Earth. The units are in Wm^{-2}. The orange arrows represent solar radiation and the blue ones represent terrestrial radiation. The blue horizontal line separates atmosphere from space.

Figure 4 shows that the majority of the outgoing longwave radiation emitted by the Earth's surface is reflected back to the surface by clouds, molecules and aerosols. The sum of the radiation emitted by the atmosphere, clouds and the small amount of radiation emitted by the surface that is able to escape to space is around 239 Wm^{-2} (Hansen et al., 2011). There is a difference of about 0.6 Wm^{-2} between the incoming and outgoing radiation. This imbalance causes the mean temperature to be higher than what it would be without the atmosphere. The warming is due to greenhouse gases which absorb efficiently the thermal infrared radiation. Changes in global radiation can cause changes to atmospheric circulation, energy balance, atmospheric chemistry, ecosystems and hydrological cycle.

2.2.2 Processes affecting radiative transfer in the atmosphere

There are several interactions electromagnetic radiation can go through in the atmosphere. These interactions can be divided into transmission, absorption and scattering processes. In transmission processes the radiation moves through the atmosphere unchanged. Scattering and absorption processes are interactions that happen with aerosols, molecules, water droplets and ice crystals in clouds (Liou, 2002).

Absorption is a process, where a molecule absorbs all or parts of the incoming radiation. The energy in the radiation is transferred to internal energy of the molecule. As was stated before, in order for

absorption to happen, the energy of the photon must be equal to the difference between two energy levels of the absorber. Because the absorbing molecules differ in composition and shape, they absorb radiation in different parts of the electromagnetic spectrum. The energy gained from the absorption can be stored into translational, rotational, vibrational or electronic forms (Seinfeld & Pandis, 2016).

Before reaching the top of the atmosphere, radiation has only direct component. The indirect component can be induced when radiation enters the atmosphere and scattering particles change the direction of the radiation. In a pure scattering process, the direction of the radiation is changed, but there is no energy transfer between the electromagnetic wave and the scattering object. In the atmosphere the size of the scattering objects varies from gas molecules ($\sim 10^{-4}$ µm) to large rain drops and hail particles (~ 1 cm) (Liou, 2002). The direction of the re-emitted radiation depends on the size and shape of the scattering object. Scattering can be divided into Rayleigh scattering and Lorenz-Mie scattering. Molecules participate in Rayleigh scattering, which happens often in the shorter wavelength region. According to Rayleigh scattering the scattered intensity depends inversely on the wavelength to the fourth power. Lorenz-Mie scattering is done by aerosols, where the scattering depends on the particle size and distribution (Liou, 2002).

Scattering and absorption processes remove energy from the incident beam of radiation. The extinction of electromagnetic wave of wavelength λ due to absorption and scattering processes in the atmosphere can be represented by Beer-Lambert's law. The beam of radiation moving through an infinitesimal distance *dx* perpendicular to the beam's intensity *F(λ)* is linearly proportional to the amount of matter in the way

$$F(x+dx,\ \lambda) - F(x,\ \lambda) = -b(x,\ \lambda)F(x,\ \lambda)dx \qquad [11]$$

where *b(x, λ)* is the extinction coefficient. The extinction coefficient is proportional to the density of the matter in the medium. Both scattering and absorption processes are taken into account in the extinction coefficient. When the travelled distance *dx* approaches zero and the equation is divided by *dx*, the equation can be represented as

$$\frac{\mathrm{d}F(x,\lambda)}{\mathrm{d}x} = -b(x,\ \lambda)F(x,\ \lambda) \qquad [12]$$

Optical depth τ is a dimensionless measure of how transparent air is. If the optical depth of the air is large, the energy of the incoming radiation is reduced more than in air with low optical depth. The optical depth for a wavelength λ between two points is defined as:

$$\tau(x_1, x_2; \lambda) = \int_{x_1}^{x_2} b(x, \lambda) \, \mathrm{d}x \qquad [13]$$

As the path length of the incoming solar beam increases the optical depth increases.

2.2.3 Parameters affecting the radiative transfer in the atmosphere

2.2.3.1 Composition of the atmosphere

The amount and distribution of gas molecules, aerosols and clouds affect how radiation is transferred in the atmosphere. Nitrogen (N) covers 78.08 % of the mass of the atmosphere, oxygen (O) contributes 20.95 % and argon (Ar) 0.9 % (Hartmann, 2016). The last 0.1 % consists of various compounds like carbon dioxide (CO_2), methane (CH_4), nitrous oxide (N_2O) and ozone (O_3). The concentration of water vapour in the atmosphere shows great spatial and temporal variation. Even though the concentration of these compounds is much smaller than for the main components of the atmosphere, they play a vital role in the Earth's radiation budget as several of them are greenhouse gases. Greenhouse gases are atmospheric compounds that absorb efficiently longwave radiation. Though the natural sources of greenhouse gases are larger than the anthropogenic ones, human activities have intensified the natural greenhouse effect by increasing the concentration of greenhouse gases like carbon dioxide and methane in the atmosphere. The increased greenhouse gas concentrations are the main reason why less radiation is able to escape to space and the mean temperature of the Earth's surface is rising (Cubasch et al., 2013).

2.2.3.2 Water vapour

Water vapour has a great impact on the Earth's climate. It is an abundant greenhouse gas and it affects radiative transfer directly by absorbing, reflecting and scattering both short and longwave radiation. Water vapour can be found both in the troposphere and the stratosphere. The majority of the water vapour is located in the troposphere, where the distribution has a great variability in time and in space. Local hydrological cycle determines the water vapour concentration in the troposphere through processes like evaporation, precipitation, condensation and largescale transfer (Liou, 2002). Due to warming of the climate, there is now more water vapour in the troposphere and stratosphere. The increased stratospheric water vapour increases the ozone loss rate in the stratosphere (Stenke & Grewe, 2005). Water vapour has also an indirect effect on the radiative transfer; it contributes to the formation of clouds. The effect of clouds on the radiative transfer is discussed later on.

2.2.3.3. Ozone

Ozone (O_3) is present both in the troposphere and the stratosphere. It is formed in the atmosphere through chemical reactions involving both natural and anthropogenic precursor species. The role of ozone on radiative transfer depends on the altitude in the atmosphere.

The majority of the atmospheric ozone is located in the stratosphere. Ozone is vital for life on the Earth as it protects living organisms from the harmful ultraviolet radiation. The concentration of ozone in the stratosphere depends on the temperature, ultraviolet radiation and photochemically active trace species (Hartmann, 2016). During 1980's and early 1990's anthropogenic emission of ozone depleting substances like halocarbons caused the decrease in the stratospheric ozone concentration. The use of these substances has been restricted by international agreements and legislation. Since year 2000 the total ozone column has remained relatively unchanged and small increases are detected (WMO (World Meteorological Organization), 2014). Previous studies have proven that there is strong negative correlation between the stratospheric ozone concentration and UV-radiation reaching the surface (Kerr & McElroy, 1993). In the mid-latitudes the total ozone column has a seasonal cycle with minimum values in winter and spring time and maximum values during summer and autumn. The seasonal cycle is similar for both northern and southern hemispheres. At the northern hemisphere mid-latitudes the difference in stratospheric ozone concentration between the maximum (summer/autumn) and minimum (winter/spring) is measured to be approximately 3 % (Calbó et al., 2005).

Approximately 10 % of the total atmospheric ozone can be found in the troposphere. Tropospheric ozone acts as greenhouse gas affecting the longwave radiation transfer. It is formed in chemical reactions between volatile organic compounds (VOC), oxides of nitrogen (NO_x) and sunlight. Increased anthropogenic emissions of NO_x and VOC coming from fuel combustion have increased ozone concentration in the troposphere. Tropospheric ozone is an important greenhouse gas in highly populated areas, where the precursors are highly available (Pawson et al., 2014).

2.2.3.4 Clouds

Clouds are an important factor influencing the global energy budget as they affect both short and longwave radiation transfer. Clouds influence shortwave radiation through absorbing and scattering processes and longwave radiation through emitting and absorbing processes. Clouds also contribute (Pawson et al., 2014) to the greenhouse effect by absorbing the longwave radiation emitted by the

Earth's surface and lower atmosphere and re-emitting it back to the surface (Tzoumanikas et al., 2016).

Clouds can be formed when temperature decreases below saturation temperature and there is cloud condensation nuclei (CCN) available. Water vapour starts to condensate on the CCN and form water droplets or ice crystals. The shape, size, distribution and total mass of water droplets or ice crystals determine how the cloud affects the radiative transfer (Hartmann, 2016). Anthropogenic emissions can alter cloud properties by increasing the number of available CCN in the atmosphere. Clouds that have more CCN are brighter, because the total surface area of the droplet is larger and thus they can reflect more radiation back to the space (Hartmann, 2016). Accurate estimation of clouds effect on radiative transfer is difficult, because of their great temporal and spatial variability.

The effect that clouds have on radiation transfer depends on the cloud type. High clouds (more than 5 km above the ground), like cirrus clouds, are almost transparent to solar radiation. They absorb efficiently outgoing longwave radiation emitted by the lower atmosphere and the Earth's surface. High clouds also emit radiation to space, but because of their cold temperature the radiation they emit has lower energy than what the surface would emit without the cloud. High clouds have a warming effect on the Earth's radiation budget (Liou, 2002).

Low (less than 2 km above the ground) and mid-level (2-6 km above the ground) clouds are thick and they have high albedo. This makes them reflect efficiently incoming solar radiation. Low clouds also emit infrared radiation to the Earth's surface and to space, but because they have almost the same temperature as the surface they do not affect significantly the outgoing longwave radiation to space. Previous studies show that the cooling effect due to reflectivity of low and mid-level clouds is responsible for -50 Wm^2 and the warming effect due to high clouds for +30 Wm^2 (Boucher et al., 2013). The global net effect of clouds is cooling and approximately -20 Wm^2.

2.2.3.5 Aerosols

Aerosols are liquid or solid particles suspended in the air. The most important effect aerosols have on radiation transfer is through absorption and scattering of solar radiation and absorption, scattering and emitting of terrestrial radiation. Aerosols can also have an indirect effect on radiation as they act as CCN and contribute thus to cloud formation (Lohmann et al., 2000; Nakajima et al., 2001).

Tropospheric aerosols have both natural (e.g., sea salt, pollen) and anthropogenic sources (e.g., pollution from fossil fuel combustion). Aerosols can also be produced in the troposphere through complex chemical reactions. The lifetime of a particle depends on its size and the highest

concentrations are often found near the emission source. The scattering effect of a particle depends on the shape, size and chemical composition (Liou, 2002). For example, sulphate aerosols from natural and anthropogenic sources reduce the amount of solar radiation reaching the surface, because of their reflective properties. Black carbon, on the other hand, absorbs radiation effectively and warms the atmosphere. In the stratosphere the main source of aerosols is from volcanic eruptions (Hartmann, 2016). Volcanic eruptions can release great amounts of sulfuric dioxide into the stratosphere, which is transformed to sulphuric acid, which again condenses to sulphate aerosols. These aerosols can cause a temporary cooling of the Earth by reflecting and scattering the incoming solar radiation.

2.2.4 How radiation affects atmospheric chemistry

Radiation emitted by the Sun drives the chemistry of the atmosphere by breaking molecules into simpler compounds which can be highly reactive. In the atmosphere the most important first order reaction is photodissociation, where the chemical composition of a molecule A is changed due to absorption of a photon

$$A + h\nu \rightarrow B + C \qquad [14]$$

Where the photon is represented as $h\nu$ (Planck's constant multiplied by the frequency of the photon). The energy of a photon can be represented per mole by multiplying with Avogadro's number

$$\varepsilon = 6.022 \cdot 10^{23}\, h\nu = 6.022 \cdot 10^{23}\, \frac{hc}{\lambda} = \frac{1.19625 \cdot 10^5}{\lambda}\, \text{kJ mol}^{-1} \qquad [15]$$

The photon energies can be roughly compared to the binding energies of the absorbing molecules. If the energy of a specific bond is less than the energy of the photon, the photodissociation can happen. The loosest bonds can be broken by photons with wavelengths in the red part of the visible wavelength band. For example NO-O bond energy in NO_2 is approximately 300 kJ mol^{-1} which corresponds to photon with wavelength of 400 nm (Seinfeld & Pandis, 2016).

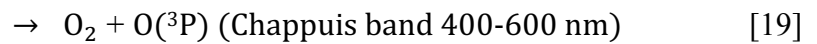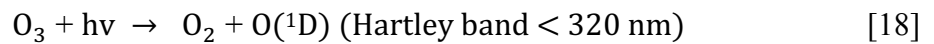2.2.4.1 Important photochemical reactions in the atmosphere

The only source of many vital molecules in the atmosphere is through photodissociation. The stratospheric ozone formation takes place approximately 30 km above the ground. The ozone formation starts with a reaction, where a photon with wavelength less than 242 nm (UV-C radiation) breaks a dioxygen molecule into two oxygen atoms

$$O_2 + h\nu \rightarrow O(^1D) + O(^3P) \qquad [16]$$

Ozone is formed in a reaction, where the produced oxygen atom reacts with a dioxygen molecule and another molecule M

$$O_2 + O + M \rightarrow O_3 + M \qquad [17]$$

where M is a bouncer molecule most likely O_2 or N_2. The ozone molecule decomposes back to oxygen molecule and oxygen atom by absorbing radiation in the wavelength band between 240-320 nm (UV-B and UV-C wavelength band)

$$O_3 + h\nu \rightarrow O_2 + O(^1D) \text{ (Hartley band} < 320 \text{ nm)} \qquad [18]$$

$$\rightarrow O_2 + O(^3P) \text{ (Chappuis band 400-600 nm)} \qquad [19]$$

Photolysis and chemical reactions can produce species that have more energy than the species would have in the ground state. These are called excited species. A first state of the electronically exited oxygen atom $O(^1D)$, produced in equation 16, is the most important excited species for the atmospheric chemistry, because it can react with unreactive species like H_2O and N_2O (Seinfeld & Pandis, 2016). The photolysis of ozone (reaction 18) is the main source of $O(^1D)$ below 40 km. Equation 18 is followed by the following reactions:

$$H_2O + O(^1D) \rightarrow OH + OH \qquad [20]$$

$$OH + O_3 \rightarrow HO_2 + O_2 \qquad [21]$$

$$HO_2 + O_3 \rightarrow OH + 2O_2 \qquad [22]$$

The previous reactions are important, because they produce hydroxyl ($\cdot OH$) and hydroperoxyl ($HO_2^{\cdot}$) radicals to the atmosphere. The OH radical is the main oxidant in the troposphere, because it is highly reactive and has a large concentration in the atmosphere (global mean concentration approximately $1 \cdot 10^6$ molecules cm^{-3} (Lawrence et al., 2001)). It can react basically with all the trace species in the atmosphere, thus the concentration of OH radical determines the concentration of many of the greenhouse gases in the troposphere. Reaction 22 results in atmospheric peroxides

$$HO_2 + HO_2 \rightarrow H_2O_2 + O_2 \qquad [23]$$

Hydrogen peroxide (H_2O_2) acts also as an oxidant in the troposphere. Hydrogen peroxide is able to oxidise SO_2 into sulphate in the aqueous phase. This process contributes to the acidification of cloud droplets and aerosol particles (Guo et al., 2014).

$O(^1D)$ can also react with nitrous oxide to produce NO

$$N_2O + O(^1D) \rightarrow NO + NO \qquad\qquad [24]$$

The previous reaction is the main source of stratospheric NO_X (NO and NO_2). These gases contribute to formation of tropospheric ozone, photochemical smog and acid rain.

Most of the incoming radiation with wavelength less than 290 nm is absorbed by O_3 and O_2. Nitrogen dioxide (NO_2) has a great influence on radiative transfer, because it can absorb radiation in the wavelength band between 300-370 nm. The wavelength band covers parts of visible and ultraviolet wavelength bands. The photolysis of nitrogen dioxide produces NO and O

$$NO_2 + hv \rightarrow NO + O \quad (\lambda < 420 \text{ nm}) \qquad\qquad [25]$$

$$NO + O_3 \rightarrow NO_2 + O_2 \qquad\qquad [26]$$

The photodissociation of NO_2 contributes to the formation of ozone according to reaction 17. Many other photochemical reactions, which are not mentioned here, are also important to the atmospheric chemistry.

3 Observations

3.1 SMEAR II

The data used in this study is from SMEAR II (Station for Measuring Forest Ecosystem-Atmosphere Relations) station (61°51′N, 24°17′E) (Hari & Kulmala, 2005). The SMEAR II station was opened in 1995. It is located in Hyytiälä, Finland approximately 220 km North-West from Helsinki (Figure 5). The near-by area is sparsely populated and the nearest large city, Tampere (more than 220 000 inhabitants), locates approximately 60 km from the station. The measurement station is located on flat land area 180 m above the sea level. The surrounding area is rather homogenous rural boreal forest area, dominated by Scots pine, Norway spruce and birches. Figures 5b-d show the measurement mast and the new measurement tower, where most of the instruments measuring radiation parameters are situated.

Finland is situated at mid-latitudes between the 60th and 70th parallel north. The location in the mid-latitudes causes the length of the day to vary between different seasons. During winter solstice the Sun is up for less than six hours, whereas during summer solstice the Sun can be up for more than 19 hours.

Finland belongs to an area where cold polar and warm subtropical air masses meet. The local climate is warmer than on average at the same latitude, because of the location in the western part of the Eurasian continent, where winds bring warm air from the North-Atlantic. The local climate has typical properties of both maritime and continental climates. Weather in the area depends mainly on the location of low and high pressure systems and the direction of the winds (FMI (Finnish Meteorological Institute), 2018a). Especially during winter time, the weather can change rapidly. The annual mean temperature is 3 °C and precipitation 700 mm.

Figure 5a) Location of SMEAR II station on the map b) The measurement mast is 127 m tall, c) the view from the top of the measurement mast during winter time and d) the new radiation tower is 35 m tall (INAR (Institute for Atmospheric and Earth System Research), 2018) .

The Baltic sea and the lakes inland influence the air humidity. The evaporated water from the sea and lakes rises the air humidity especially during summer and autumn. Winter and spring time are typically dry.

The air relatively free from pollutants, because the measurement station is located far from human activities. Tropospheric ozone is important pollutant in areas where the precursors of ozone, NO_x and VOC, are highly available. NO_x emissions increase the amount of tropospheric ozone in rural areas. The majority of these emissions come mainly from combustion processes and transportation (Pawson et al., 2014). The monthly median tropospheric ozone concentration in the area of the measurement station varies from 20 to 50 ppb, whereas the tropospheric ozone can reach values over 100 ppb during polluted periods in highly populated urban areas (Monks et al., 2015).

During autumn and winter, cloud formation is associated with the crossing frontal systems. This is a typical for cloud formation also during spring and summer, but there are also convective clouds due

to the increased solar radiation. During spring and summer the cold ocean and lakes inhibit formation of convective clouds. During autumn the sea is warmer than the land surface, which makes the convective clouds form over the ocean rather than over the land. Also the vegetation and soil affect the convective cloud formation (Venäläinen & Heikinheimo, 1997).

3.2 Cloud base height measurements

The most common instrument used for cloud base height detection from the ground is a ceilometer. At SMEAR II station cloud base height is measured with Vaisala CT25K ceilometer, which is located next to a measurement cottage surrounded by trees. The instrument uses pulsed diode laser Light Detection (LIDAR) technology to detect cloud base height and precipitation. It can measure up to three cloud layers, which are retrieved by an algorithm produced by Vaisala. The measurement range of the instrument reaches up to 7500 meters. The instrument gives NaN values during clear skies or if the cloud base height is more than 7.5 km. NaN is undefined or unpresentable value. Backscatter profiles are retrieved once every minute and the measured wavelength is 905 nm. Ceilometers are used for both research and operational purposes, especially at airports. Cloud base height measurement started in June 2014 at the SMEAR II station. The data includes both day and night time measurements.

Ceilometer gives a good temporal and vertical resolution of cloud base height. Because of the narrow horizontal resolution of ceilometer, the description of the total cloud cover can sometimes be misleading. Ceilometers tend to also underestimate higher cloud layers as low clouds can disguise them (Wagner & Kleiss, 2016). The highest clouds that are located above the detection height (7500 m) can be left undetected.

3.3 Radiation measurements

The different radiation parameters measured between years 1997 and 2017 at the SMEAR II station are described here. Over the years, there have been 20 different long-term measurements of radiation parameters. This study does not focus on the solar radiation spectrum measurement. Figure 6 shows the time periods at which each measurement has been ongoing. All the instruments at the 35 m radiation tower were previously at 18 m old radiation tower until February 2017. Snow and ice accumulation on the radiation sensors was prevented by fans placed next to the sensors.
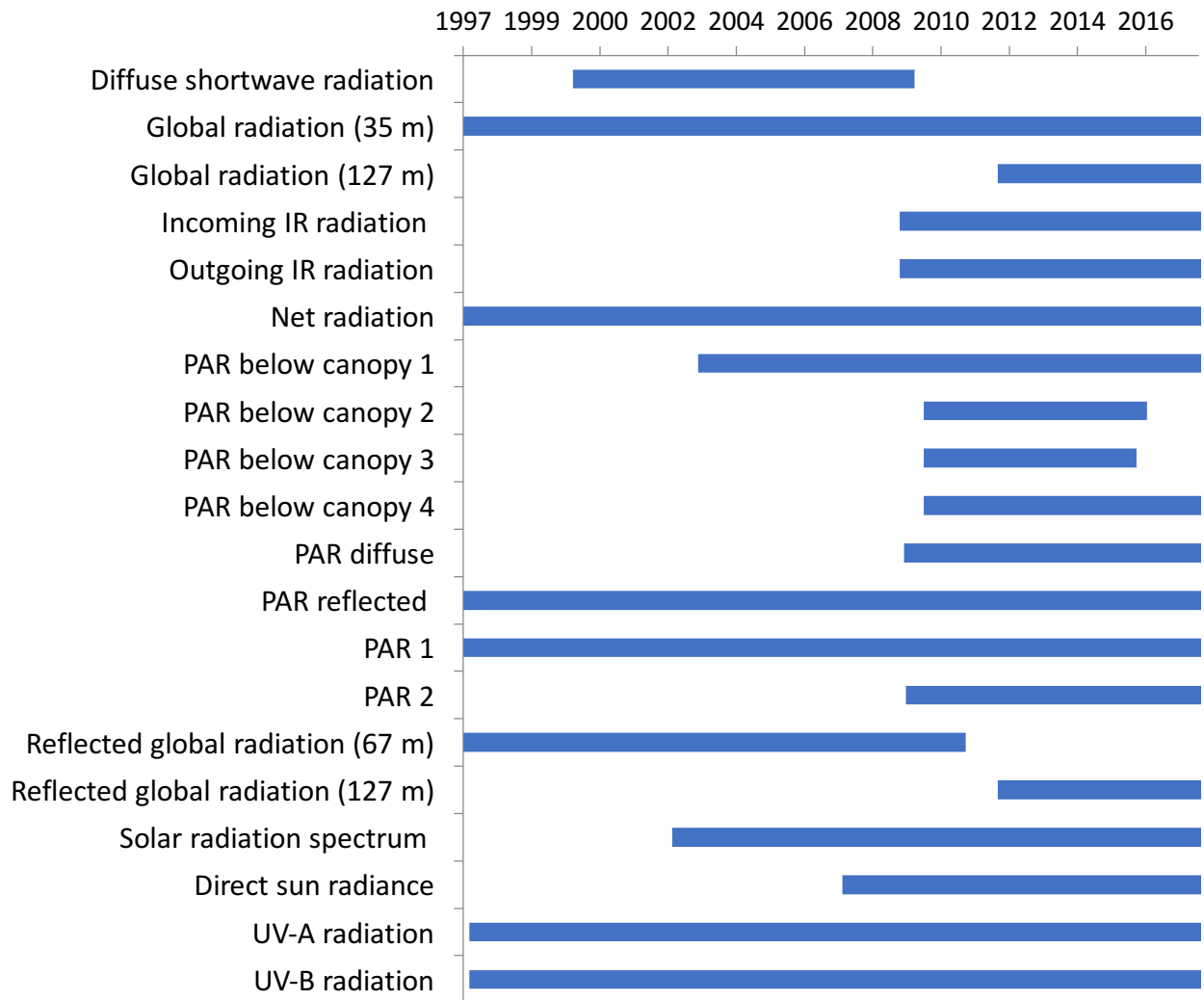
Figure 6 Different radiation parameters measured at the SMEAR II station in Hyytiälä between years 1997 and 2017. The different PAR and PAR below canopy measurements are instruments situated in different locations at the station.

More specific information about the different instruments is given in Table 1. The table shows the instrument type, how often they have been calibrated, what is the suggested calibration time by the manufacturer and where it is located at the SMEAR II station. Figure 7 represents the map of the measurement station. The suggested calibration times are from the manufacturer websites. The bookkeeping of the instrumentation and calibration information has not been consistent. Some of the old measurement diaries have been hand written and some information might have been lost.

Table 1 The long-term measurements of radiation parameters at the SMEAR II station. The suggested calibration times are from the manufacturer websites. The empty boxes in calibration and old instrument sections mean that there is no information available. Location of the different instruments on map can be seen in Figure 7.

Measured quantity	Instrument	Calibration	Suggested calibration time	Old instruments (Date of the change)	Location
Diffuse global radiation	Delta BF3 Sunshine Sensor		every two years	Reemann TP 3 pyranometer with shading ring , Delta BF3 Sunshine Sensor (12/2009)	Tower 35 m (old measurement tower 18 m until 2/2017)
Global radiation	Middleton SK08/ EQ08 pyranometer	2006, 2008,2011	once a year	Reemann TP 3 pyranometer , Delta BF3 Sunshine Sensor (12/2009)	Tower 35 m (old measurement tower 18 m until 2/2017)
Global radiation	Middleton SK08 pyranometer		once a year		Mast 127 m
Incoming IR radiation	Kipp and Zonen CNR1 net radiometer		every two years		Mast 33 m
Outgoing IR radiation	Kipp and Zonen CNR1 net radiometer		every two years		Mast 33 m
Net radiation	Kipp and Zonen NRLite2 net radiometer	Has not been calibrated	every two years	Reemann MB 1 net radiometer (old instrument removed 09/2011, new instrument started 06/2014)	Mast 67 m
PAR below canopy 1	4 x Li-Cor LI-190SZ quantum sensors on the stationary boom (Maapar)	once a year	every two years		Forest 0.6 m (northeast of REA cottage)
PAR below canopy 2	5 x Apogee SQ-100 PAR sensor (Canpar)	once a year	when needed		Forest 0.6 m (northwest of REA cottage)
PAR below canopy 3	5 x Apogee SQ-100 PAR sensor (Canpar)	once a year	when needed		Forest 0.6 m (north of tree tower)
PAR below canopy 4	5 x Apogee SQ-100 PAR sensor (Canpar)	once a year	when needed		Forest 0.6 m (between main and REA cottages)
PAR diffuse	Delta BF5 Sunshine Sensor	once a year	every two years	Delta BF3 Sunshine Sensor (11/2014)	Tower 35 m (old measurement tower 18 m until 2/2017)
PAR reflected	Li-Cor Li-190SZ quantum sensor facing down	once a year	every two years		Mast 67 m
PAR 1	Li-Cor Li-190SL quantum sensor	once a year	every two years	Li-Cor Li-190SZ quantum sensor (02/2017)	Tower 35 m (old measurement tower 18 m until 2/2017)
PAR 2	Delta BF5 Sunshine Sensor		every two years		Tower 35 m (old measurement tower 18 m until 2/2017)
Reflected global radiation	Reemann TP 3 pyranometer facing down	2002, 2011			Mast 67 m
Reflected global radiation	Middleton SK08 pyranometer facing down		once a year		Mast 127 m
UV-A radiation	Solar light SL 501A radiometer	between years 2013-2016 calibration has been done once a year	once a year		Tower 35 m (old measurement tower 18 m until 2/2017)
UV-B radiation	Solar light SL 501A radiometer	between years 2013-2016 calibration has been done once a year	once a year		Tower 35 m (old measurement tower 18 m until 2/2017)

Figure 7 Map of the SMEAR II station. The satellite image was retrieved from Google Maps on the 10th of September 2018.

3.3.1 Global radiation

Global radiation (0.3-2.8 µm) describes the total incoming solar radiation to a surface. It includes both diffuse radiation resulting from scattering or reflection and direct components. The wavelength bands included in the global radiation reaching the surface are UV-A (Ultraviolet A), UV-B (Ultraviolet B), PAR (Photosynthetically Active Radiation) and NIR (Near Infrared Radiation). The amount of global radiation reaching the Earth's surface depends on the orbital geometry between the Sun and the Earth, clouds, aerosols and the chemical composition of the atmosphere. The transfer of different wavelength bands in the global radiation are influenced partly by different factors. Because NIR (0.7-2.8 µm) wavelength band contributes 52.8 % to the global radiation at the top of the atmosphere, the changes in NIR have the greatest effect on global radiation (Frederick et al., 1989). The transfer of NIR is highly affected by absorption by water vapour molecules. Global radiation is measured at three different heights; at 35, 67 and 127 m at the SMEAR II station. At both 35 m measurement tower and at 127 m measurement mast the instrument is Middleton SK08 pyranometer. The global radiation data from 67 m is not included in this study, because the measurement only started in October 2017.

Figure 8 shows the typical hourly median values of global, diffuse and reflected global radiation at SMEAR II station in January and July. In January the maximum values of hourly median global radiation stay below 40 Wm^{-2}, whereas in June the values can rise close to 500 Wm^{-2} at the SMEAR

II station. The detection of very low values of incoming global radiation, ice and snow cover during winter time can cause errors to the measurements.

3.3.2 Diffuse global radiation

Diffuse global radiation (0.3-2.8 µm) is solar radiation that has been scattered in the atmosphere by molecules or particles before reaching the surface (Calbó et al., 2005). During clear skies, the diffuse fraction of global radiation stays small. The diffuse fraction of global radiation increases as the cloud cover or aerosol load in the atmosphere increases.

Diffuse radiation is measured with Reemann TP 3 pyranometer with shading ring at the 35 m measurement tower. Figure 8a shows that during winter time, the majority of the incoming global radiation at the SMEAR II station comes as diffuse rather than direct radiation. During summer time diffuse radiation covers approximately one third of the global radiation (Figure 8b). The variability included in the hourly median values is high both during summer and winter time.

3.3.3 Reflected global radiation

Reflected global radiation (0.3-2.8 µm) is the part of the solar radiation that is reflected back to the atmosphere by the Earth's surface. The ratio between reflected radiation $S\uparrow$ and global radiation $S\downarrow$ is called albedo α

$$\alpha = \frac{S\uparrow}{S\downarrow} \qquad\qquad [27]$$

High albedo values correspond to surfaces which reflect most of the incoming radiation back to the atmosphere and low values correspond to surfaces which are able to absorb radiation effectively. Because albedo influences how much of the incoming shortwave radiation is absorbed to the surface, it has an effect on the local surface temperatures. The reflectivity depends on the properties of the reflecting surface, frequency of the incoming radiation and solar zenith angle. Examples for typical albedo values are for coniferous forest 12 %, dry light sand 35 % and for fresh dry snow 80 %. White surfaces like clouds and snow are most reflective for the visible part of the electromagnetic spectrum. Albedo of these surface is smaller for near infrared radiation, because the water molecules in the surface absorb parts of the longwave radiation (Hartmann, 2016).

Reflected radiation has been measured at two heights; 67 m and 127 m at the measurement mast. At 67 m the instrument was Reemann TP 3 pyranometer facing down and the ongoing measurement at 127 m is done with Middleton SK08 pyranometer facing down. Figure 8 shows the hourly median

values of reflected radiation at the SMEAR II station in January and in July. Based on the figures, the fraction of reflected radiation is higher in January than in July.
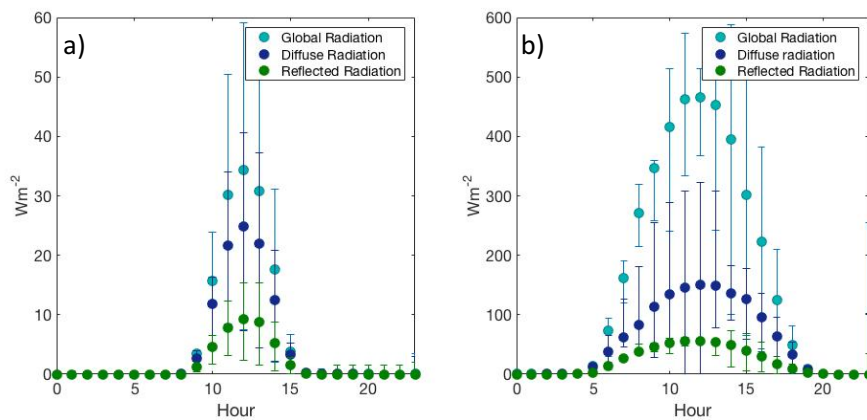

Figure 8 The diurnal patterns of global radiation (35 m), diffuse global radiation (35 m) and reflected radiation (67m) a) in January and b) in July. The hourly median values are based on the data from the whole time period when the specific measurement has been ongoing. Variability associated with the hourly median values is calculated with the 25th and 75th percentiles.

3.3.4 Photosynthetically active radiation

PAR is the visible part of global radiation covering wavelengths from 0.4 to 0.7 μm. It is measured in units $\mu mol\, m^{-2}\, s^{-1}$. PAR covers 38.9 % of the global radiation at the top of the atmosphere (Frederick et al., 1989). Plants use visible light for photosynthesis. PAR measurements are used for example to study plant physiology and biomass production (Alados et al., 1996). PAR 1 is measured with Li-Cor Li-190SZ quantum sensor and the comparison measurement PAR 2 is measured with Delta BF5 Sunshine Sensor.

Figure 9 shows the diurnal pattern of the hourly median value of PAR in January and July. The diurnal pattern is similar to that of global radiation. The hourly median values of PAR are approximately 10 times higher during summer time than during winter at the SMEAR II station. Transfer of PAR in the atmosphere is affected by Rayleigh scattering by gas molecules, Mie-scattering by particles and aerosols, reflecting by clouds and also absorbing by ozone, water vapour and carbon dioxide (Szeicz, 1974).

3.3.5 Diffuse photosynthetically active radiation

The visible light that has been scattered by an object before reaching the surface is called diffuse PAR. Similar to diffuse global radiation, the fraction of PAR diffuse remains small during clear skies. Diffuse PAR is measured with Delta BF5 sunshine sensor at the 35 m radiation tower. The diurnal pattern of the hourly median value of diffuse PAR in January and July is shown in Figure 9. Most of

the incoming PAR reaching the surface in January is diffused. In July the diffuse PAR covers approximately half of the incoming PAR.

3.3.6 Reflected photosynthetically active radiation

Reflected PAR (0.4-0.7 µm) is the part of visible radiation that is reflected back to the atmosphere. Chlorophyll in green plants can absorb almost all of the incoming visible radiation and use it for photosynthesis. Growing plants can absorb more than 90 % of the incoming PAR. The chlorophyll concentration decreases when the plants die and after which they start to reflect more visible radiation (Hartmann, 2016). Reflected PAR is measured with Li-Cor Li-190SZ quantum sensor at the 35 m radiation tower. The diurnal pattern of the hourly median value of reflected PAR is presented in Figure 9. The reflected part of the visible radiation covers approximately 20 % of the total incoming PAR at noon in January. The reflected part of the visible radiation remains very low in July.

3.3.7 Photosynthetically active radiation below canopy

The visible part of the global radiation, that is able to penetrate through the canopy is called PAR below canopy (0.4-0.7 µm). The physiological condition and texture of the canopy and solar zenith angle determine how much radiation can access through the canopy (Hartmann, 2016). PAR below canopy 1 is measured with Li-Cor LI-190SZ quantum sensors on the stationary boom. PAR below canopy 2, 3 and 4 are measured with Apogee SQ-100 PAR sensors. Figure 9 shows the diurnal pattern of the hourly median value of PAR below canopy 1 in January and in July.
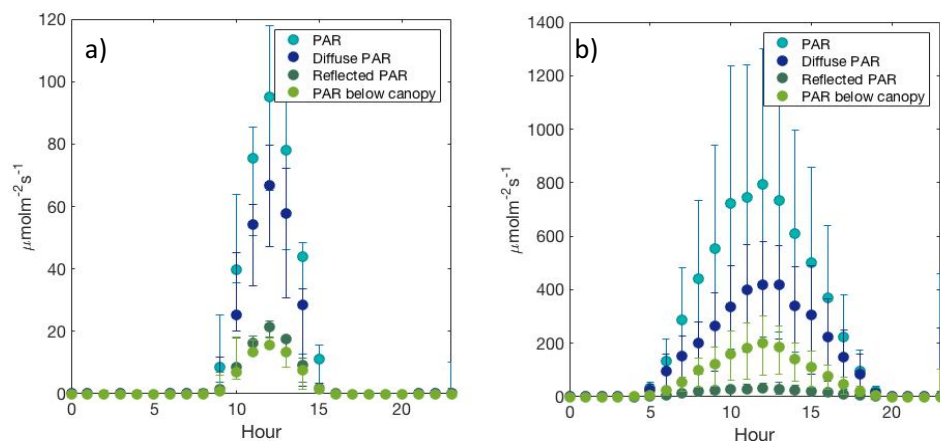

Figure 9 The diurnal patterns of the hourly median values of PAR, diffuse PAR, reflected PAR and PAR below canopy a) in January and b) in July. The hourly median values are based on the data from the whole time period when the specific measurement has been ongoing. Variability associated with the hourly median values is calculated with the 25th and 75th percentiles.

3.3.8 Ultraviolet radiation

Ultraviolet radiation is a portion of global radiation that covers the shortest wavelengths from 0.1 – 0.42 μm. Ultraviolet radiation can be divided into UV-A (0.32-0.42 μm), UV-B (0.28-0.32 μm) and UV-C radiation (0.1-0.28 μm). The limits between different parts of the UV radiation vary slightly depending on the literature. The most intense part of the UV radiation, UV-C radiation, is completely absorbed by the molecular oxygen and ozone in the stratosphere before reaching the Earth's surface. UV radiation covers approximately 8.3 % of the global radiation at the top of the atmosphere (Frederick et al., 1989).

The transfer of UV-A and UV-B radiation in the atmosphere are mostly affected by ozone concentration, the presence of other gases like sulphur dioxide and nitrogen dioxide, clouds and aerosols (Calbó et al., 2005). Changes in the stratospheric ozone concentration have the greatest impact on UV-B radiation (Frederick et al., 1989). Excessive UV-B radiation exposure is known to be harmful for living organisms; for example it can cause skin cancer and productivity losses for crops (Brash et al., 1991; Fiscus & Booker, 1995). On the other hand, UV-B radiation is involved in the production of vitamin D, which is vital for human bones (Bryant, 1997). Both UV-A and UV-B radiation are measured with Solar light SL 501A radiometer 35 m above the ground.
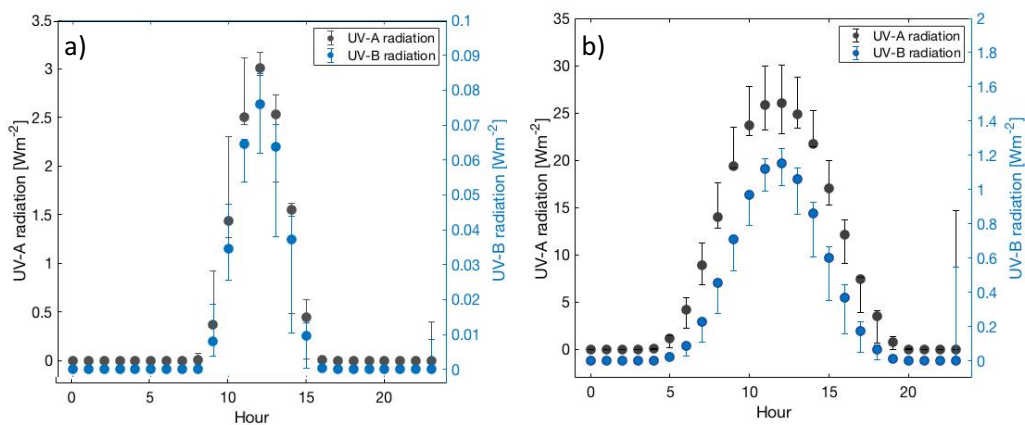

Figure 10 The diurnal patterns of hourly median values of UV-A and UV-B radiation a) in January and b) in July. Note the different y-axes for the two parameters. The hourly median values are based on the data from the whole time period when the specific measurement has been ongoing. Variability associated with the hourly median values is calculated with the 25th and 75th percentiles.

The diurnal pattern of the hourly median value of UV-A and UV-B radiation in January and in July are presented in Figure 10. Note the different y-axis for the two parameters. The figures indicate that both UV-A and UV-B radiation follow the diurnal pattern of global radiation. According to the figure, the hourly median value of UV-A radiation reaching the Earth's surface is close to ten times higher in July than in January at the SMEAR II station. The hourly median value of UV-B radiation can be

15 times higher in July compared to January at the SMEAR II station. The maximum values are measured during noon both in January and in July.

3.3.9 Incoming infrared radiation

Incoming infrared (IR) radiation (5-50 μm) describes the longwave radiation emitted by the atmosphere and clouds back to the surface. The amount depends highly on clouds, water vapour, greenhouse gas concentration and temperature in the atmosphere. Incoming IR radiation can be approximated with the following formula:

$$Q_L^{\downarrow} = \varepsilon_a \sigma T_a^4 \qquad [28]$$

where ε_a is the emissivity of the atmosphere, σ is Stefan-Boltzmann constant and T_a is the temperature of the near surface (e.g. 2 m above the ground). For water droplets, water vapour and for other greenhouse gases in the atmosphere the emissivity is close to 1, whereas for the main components of the atmosphere like oxygen molecule and nitrogen the emissivity is close to zero (Ebrahimi & Marshall, 2015). Because the weather conditions fluctuate quickly, the incoming IR radiation varies greatly.

Incoming IR radiation is measured with Kipp & Zonen CNR1 radiometer at the 33 m measurement mast. The diurnal pattern of the hourly median value of incoming IR radiation is presented in Figure 11. The variability included in the hourly median values is high in January. The diurnal pattern is more pronounced in July and it follows the diurnal pattern of global radiation with a delay. There is some variation included in the hourly median values especially during evening and night time in July.

3.3.10 Outgoing infrared radiation

Outgoing IR (5-50 μm) is the longwave radiation emitted by the Earth's surface and lower atmosphere. A large fraction of the emitted infrared radiation is absorbed by different greenhouse gases like carbon dioxide and methane in the atmosphere. Also clouds and aerosols have an effect on the radiation transfer by absorbing and reflecting the longwave radiation (Liou, 2002). Outgoing IR radiation can be approximated with the blackbody approximation:

$$Q_L^{\uparrow} = \varepsilon_s \sigma T_S^4 \qquad [29]$$

where ε_s is the emissivity of the surface, σ is the Stefan-Boltzmann constant and T_S is the temperature of the surface.

Outgoing IR radiation is measured with Kipp & Zonen CNR1 net radiometer at 33 m height in the measurement mast. The diurnal pattern of outgoing IR radiation in January and in July are presented in Figure 11. Similarly to incoming IR radiation, the variability included in the hourly median values is higher in January than in July. Outgoing IR radiation varies less than incoming IR radiation, because the emissivity properties of a surface varies less than those of the atmosphere (Ebrahimi & Marshall, 2015).
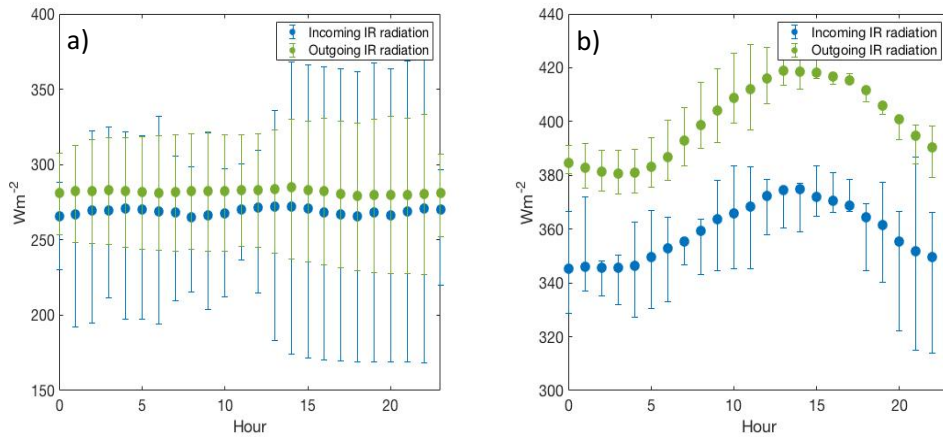
Figure 11 The diurnal patterns of the hourly median values of outgoing and incoming infrared radiation a) in January and b) in July. The hourly median values are based on the data from the whole time period when the specific measurement has been ongoing. Variability associated with the hourly median values is calculated with the 25th and 75th percentiles.

3.3.11 Net radiation

Net radiation (0.3-40 μm) is the difference between incoming and outgoing radiation. The incoming radiation includes absorbed global radiation (global radiation – reflected radiation) and incoming longwave radiation. The outgoing radiation consists of longwave radiation emitted by the Earth's surface and lower atmosphere. Net radiation can be calculated using following equation

$$Q = \downarrow S(1-\alpha) - \uparrow L + \downarrow L \tag{30}$$

where $\downarrow S$ is the global radiation, α is the albedo of the surface, $\uparrow L$ is the outgoing longwave radiation and $\downarrow L$ is incoming longwave radiation (Betts & Ball, 1997).

Net radiation is measured with Kipp & Zonen NRlite2 net radiometer at 67 m measurement mast. The diurnal pattern of the hourly median value of net radiation and the different radiation parameters contributing into net radiation are shown in Figure 12. Net radiation remains low and varies between both sides of zero during winter time. The hourly median value of net radiation can be up to 10 times

higher in July than in January at the SMEAR II station. Net radiation is typically negative during summer nights, when there is no incoming shortwave radiation and the outgoing longwave radiation is typically larger than the longwave radiation emitted by the atmosphere and clouds. Positive net radiation during day time drives the surface fluxes which again drive the formation of the atmospheric boundary layer (Betts & Ball, 1997).
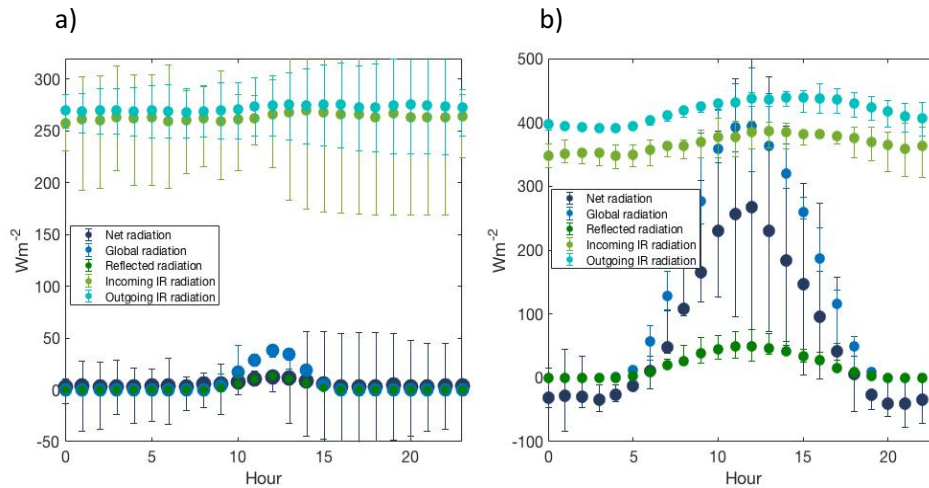

Figure 12 The median hourly values of radiation parameters contributing to net radiation a) in January and b) in July. The black dots are the median hourly net radiation. The hourly median values are based on the data from the whole time period when the specific measurement has been ongoing. Variability associated with the hourly median values is calculated with the 25th and 75th percentiles.

4. Methods

4.1 Cloud base height data

Cloud occurrence is defined as the ratio between the recorded cloud measurements (at least one of the cloud layers gives a value that is not NaN) and all the available records (Costa-Surós et al., 2013). In order to investigate the seasonal changes in cloud cover, the monthly cloud occurrence (in %) is presented. Also the distribution of the cloud base height in single layer cases are shown for January, April, July and October. Finally, the distribution of cloud base height in different cases (single layer, 2-layer and 3-layer systems) are investigated.

4.2 Radiation data

The radiation data used in this study is 30 min averaged data between 10 am and 3 pm. The time window between 10 am and 3 pm is chosen, so that the Sun is above the horizon during all of the seasons. To investigate the seasonal changes in the radiation parameters the figures are shown for

four different months representing the four different seasons; January (winter), April (spring), July (summer) and October (autumn). This is done in order to take into account the seasonal effects affecting radiation like albedo, Sun-Earth distance, solar zenith angle, cloudiness, ozone concentration and aerosol load. The months with less than 240 measurement points were removed from the plots to reduce the possibility of bias caused by data gaps. Also three-year sliding average were calculated for the monthly medians in order to reduce the effect of anomalous years. The variation for the monthly medians were calculated using 25th and 75th percentiles to study if the individual years differ statistically. The 25th and 75th percentiles were also calculated for the trend lines to investigate if the trends are statistically significant.

The relationship between different variables and their changes were also investigated. The majority of the parameters were compared to global radiation measurements, except PAR below canopy measurements which were compared to PAR measurements. Correlation between two parameters was calculated with Pearson's correlation coefficient.

5. Results and Discussion

5.1 Cloud occurrence

Figure 13 shows the cloud occurrence in percentages for years 2015, 2016 and 2017. Cloud occurrence is defined as the ratio between the recorded cloud measurements (at least one of the cloud layers is not a NaN value) and all the available records (Costa-Surós et al., 2013). Reasonably high cloud occurrence can be seen for all of the seasons. Despite the yearly variation in the cloud occurrence, some common features can be seen; the cloudiest months have occurred during winter time and the lowest cloud occurrence values have been recorded during late spring and summer time.
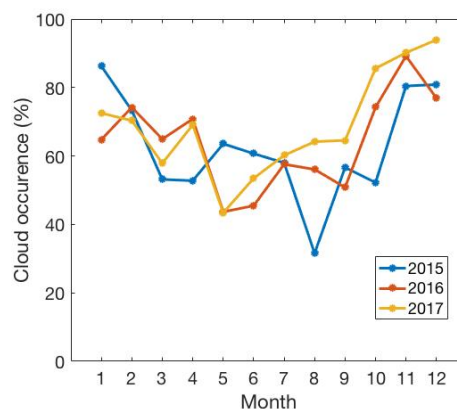

Figure 13 Cloud occurrence at the SMEAR II station in percentages during 2015, 2016 and 2017.

The studies done by Costa-Surós et al. (2013) showed similar results for Girona, though the percentages were lower for all seasons. The difference in cloud occurrence is due to climatic conditions.

For the measurement period between June 2014 and April 2018 a single layer cloud systems were detected in 89.2 % of the cases. The occurrence of specific cloud layer system is compared to the cases when at least one cloud layer was detected. 2-layered systems were detected in 10.3 % of the measurements and 3-layered systems in 0.5 % of cases. The number of higher cloud layers is expected to be underestimated by the ceilometer because the low clouds may disguise clouds above them (Costa-Surós et al., 2013).

Figure 14 represents the frequency of cloud base height for single layer cloud systems for the selected months. Each bin in the figure is 200 m wide. The seasonal patterns are clearly seen for these three investigated years. The highest frequencies are found at the bins centred at 100 and 300 m in January. The majority of the clouds detected by the ceilometer are less than 2000 m above the ground. Low clouds dominate also in April. Similarly to January, the maximum frequency is found at bins centred at 100 and 300 m. Cloud base height frequency between 1000 m and 3000 m has increased significantly from January. The highest cloud base heights are measured to be at 4000 m. In July the cloud base height is more evenly distributed among the bins. The cloud base heights are measured up
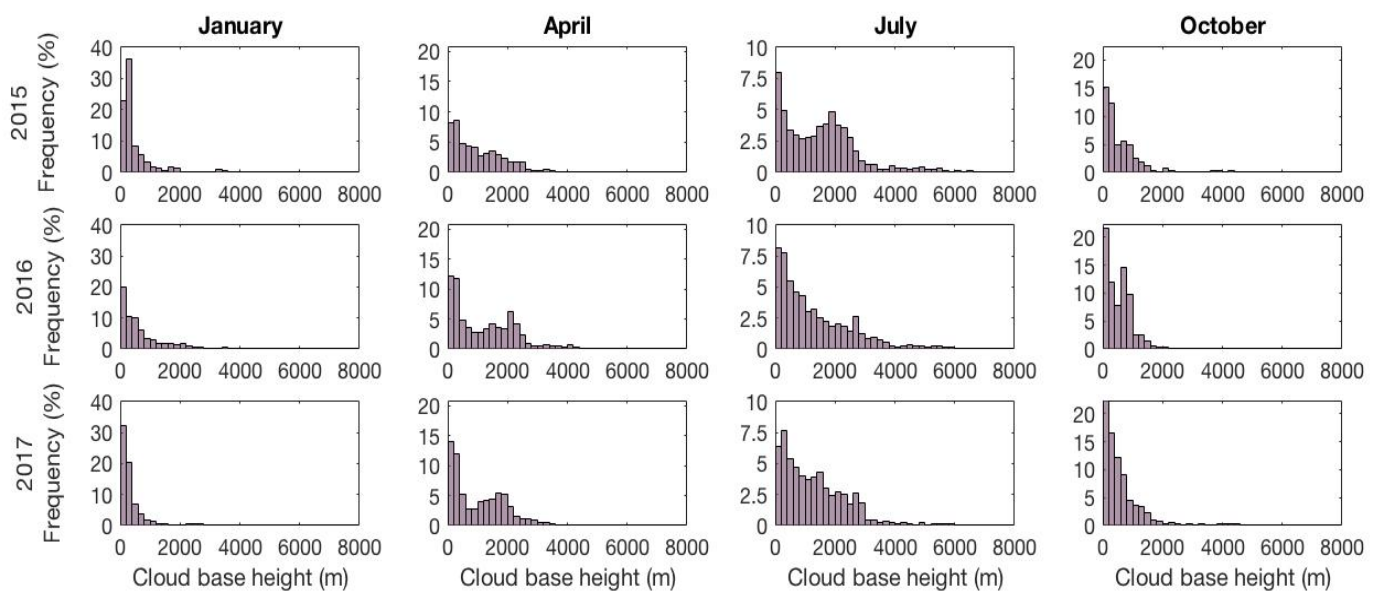

Figure 14 Frequencies of single layer cloud base height between years 2015 and 2017. Each bin is 200 m wide. Note the different y-axis for different months.

to the measurement range of the ceilometer (7700 m). The occurrence of the higher cloud base height has clearly increased from April. The maximum peaks are at the low clouds centred at the bins 100 m and 300 m. In October the maximum peaks are similarly at the low clouds centred at the bins 100

m and 300 m. The frequency typically decreases for the higher cloud base heights. The highest cloud base heights are close to 4000 m. During all of the investigated months the maximum peaks were located at the bins centred at 100 m and 300 m.

The seasonal difference in cloud base height distribution can be explained with the typical cloud type of the season. Clouds associated with the frontal systems occur year-round. The formation of convective clouds is more frequent during spring and summer due to the increased solar radiation.

Figure 15 shows the frequency distributions of the cloud base height for different cloud systems (single layer, 2-layer and 3-layer systems) between June 2014 and April 2018. The bins are now 100 m wide. Figure 15a shows the frequency of all three detected layers of cloud base height with the blue bars and the cases when only one cloud layer was detected with red bars.

Almost in 90 % of the measurements only one cloud layer was detected, which makes the two set of histograms very similar. Maximum frequency for both can be found at the bin centred at 150 m. In general, the frequency decreases as the cloud base height increases and the bins continue up to 6000 m even though the maximum frequency is found at very low height. The study done by Costa-Surós et al. (2013) showed that the maximum for the cloud base height occurrence in Girona was at a bin centred at 1400 m. The changes in the cloud base height are explained with the different climatic conditions. The seasonal pattern of typical cloud formation is similar in Spain and in Finland; clouds associated with the frontal systems occur year-round and the convective clouds dominate during spring and summer. Because the amount of incoming solar radiation is higher in Spain year-round, the season for convective clouds is longer which rises the average cloud base height.

At SMEAR II station 86.5 % of all the detected clouds are low clouds (less than 2000 m above the ground), 13.2 % are mid-level clouds (2000-6000 m) and 0.3 % are high clouds (more than 6000 m). When compared to all the data points we get a cloud occurrence of 65.1 %. For all the recorded cloud base heights mean and median were 902 m and 457 m and for single layer systems 855 m and 393 m.

Figure 15b represents the distribution of 2-layer systems. Majority (74 %) of the first detected cloud base height is measured below 1000 m. The maximum frequency for the first layer is found at the bin centred at 250 m. Figure 15c represents the cases when all three cloud layers were detected. The maximum frequency for the first layer cloud base height is found at the bin centred at 250 m. For the 2-layer systems the maximum occurrence is at the 650 m bin and for the 3-layer systems at 1250 m.
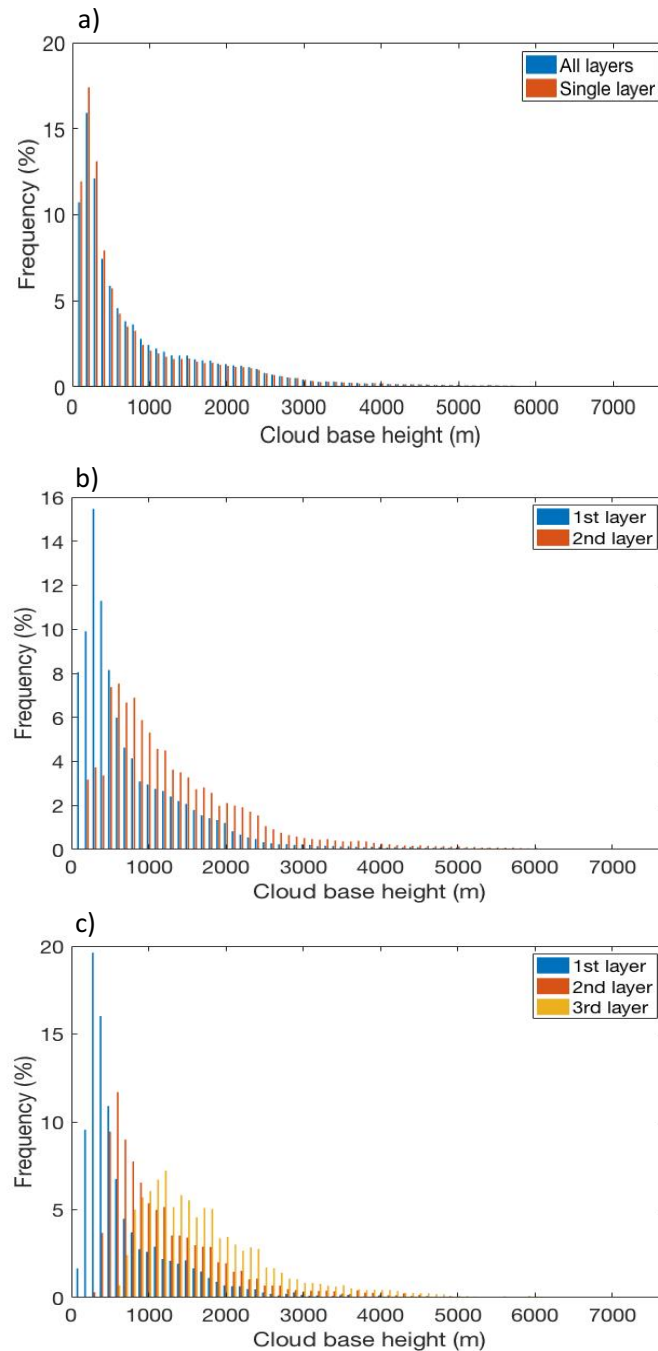
Figure 15 a) Frequency distribution for all the cases and single layer cases. b) Distribution of the lower and higher layers when two layers are detected. c) Distribution of the first, second and third layers when three layers are detected. The data is from the time between June 2014 and April 2018.

Cloud cover can be estimated from man-made observations, soundings, different instruments located at the ground like ceilometers, LIDARs and from satellites. Man-made observations and measurements from the ground often underestimate higher cloud layers, which are obscured by lower clouds. Satellite measurements include large uncertainties concerning vertical distribution of clouds and low clouds can be obscured by the higher clouds (Costa-Surós et al., 2013). New instruments on the satellites have improved over the recent years and they are able to detect the vertical structure of

clouds better than before. The use of satellite data is limited by the low temporal resolution. In order to get more informative view of the total cloud cover, different methods of detecting clouds should be coupled.

When compared to radiation data, it is good to bear in mind that the cloud data consist of both day and night time data while radiation data is only between 10 a.m. and 3 p.m. Though the horizontal resolution of ceilometer is narrow, the cloud occurrence detected by ceilometer can be used as an indicator of the cloud cover. Costa-Surós et al. (2013) studied the cloud occurrence in Girona, Spain and they showed that the cloud cover observations made in the near-by airport correlated well with the measurements done with ceilometer.

5.2 Radiation measurements

5.2.1 Global radiation

Figure 16 shows the time series of the monthly median global radiation measured at SMEAR II station between 1997 and 2017. The time series is shown for four different months; January, April, July and October. January 1999, April 1998, July 1998 and October 1998 were left out of the time series due to the insufficient amount of measurement points. Global radiation has a pronounced seasonal pattern. The maximum values are measured in July after which global radiation starts to decrease until the minimum values are reached in January. The monthly median value can be more than 15 times higher during summer than during winter time at the SMEAR II station. In April the amount of incoming solar radiation is significantly higher than in October. The mean and median values for global radiation are 41.4 Wm^{-2} and 26.1 Wm^{-2} in January, 380.6 Wm^{-2} and 396.6 Wm^{-2} in April, 457.0 Wm^{-2} and 476.4 Wm^{-2} in July and 128.3 Wm^{-2} and 99.8 Wm^{-2} in October. The Earth's rotation around the Sun causes changes to the solar zenith angle which determines the amount of incoming global radiation and explains the seasonal differences.

All of the investigated months show annual fluctuation. The fluctuation is greater during spring and summer time, when the relative error is greater due to the larger amount of incoming solar radiation. There is also fluctuation within the individual monthly median values. The 95 % confidence interval shows that the slopes do not differ from zero statistically, thus the trends are not real. The annual fluctuation for the monthly median values of global radiation are related to changes in cloudiness and aerosol load in the atmosphere (Soni et al., 2012). The local weather is highly influenced by the synoptic scale weather disturbances, which show great temporal variation during all seasons.

During the active sunspot periods solar flares and eruptive prominences can occur. These phenomena increase the amount of gamma-ray, X-ray and ultraviolet radiation. The effect on the total radiation is very small (Hartmann, 2016). Figure 4 represented the sunspot cycle during the last 24 years. The
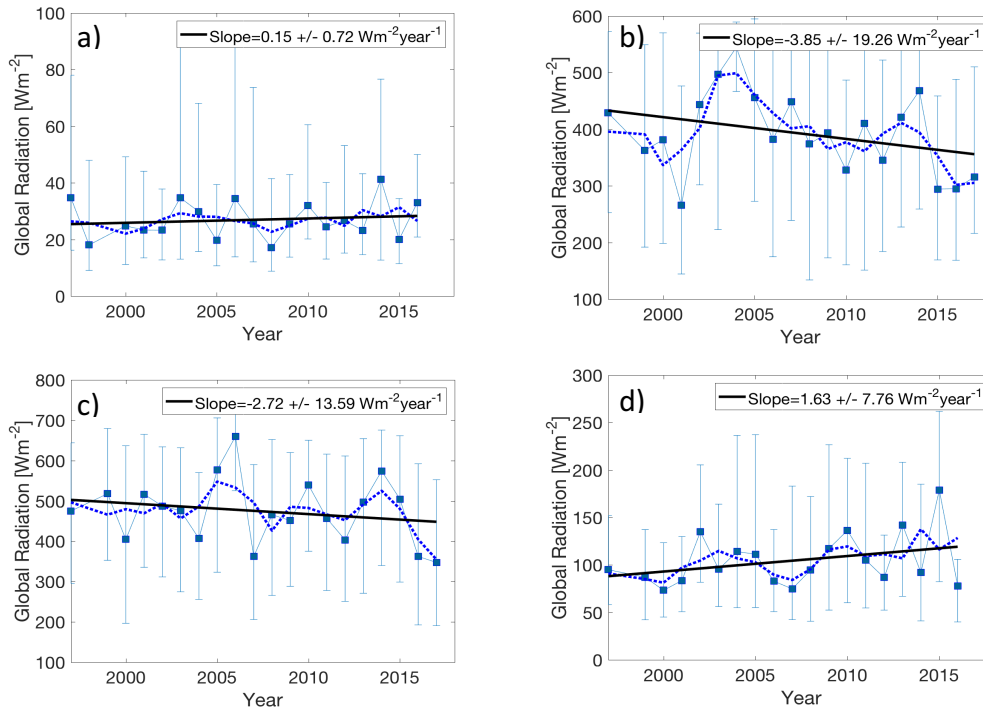

Figure 16 The time series of monthly median global radiation (measured at 35 m) between years 1997 and 2017 a) in January, b) in April, c) in July and d) in October. The blue boxes represent the monthly median values, the blue dashed line is the three-year-sliding average and the black solid line is the trend line. Variation for the monthly median values is presented with the error bars.

two last maxima in sunspots were measured in 2001 and 2014. The effect of increased solar radiation due to sunspots maxima cannot be seen in Figures 16a-d. The effect of sunspot maxima on UV radiation is studied later on.

Previous study by Wild (2009) shows that in many places around the world global radiation measurements showed decreasing trends between 1950's and 1980's. After 1980's global radiation started to increase again until the beginning of the 21st century. Wild (2009) referred to these variations as global dimming and brightening periods. The study indicates that the variations in the insolation are caused by changes in the atmosphere rather than changes in the Sun's activity. There is evidence that the changes in the insolation are due to changes in the anthropogenic emissions, which have led to changes in aerosol and cloud abundance (Mishchenko et al., 2007; Stern, 2006; Stjern et al., 2009) .

There have not been many studies in Finland concerning the analysis of long-term global radiation data. Venäläinen and Heinkinheimo (1996) studied the monthly median global radiation in different

locations around Finland. The data was based on direct measurements with pyranometer, sunshine hour measurements and cloud observations from years 1961 to 1990. Venäläinen and Heikinheimo (1996) used both day and night data, thus the measured values differ from the ones in this study. Based on the results monthly median global radiation in the region of SMEAR II station has been between 8-10 Wm^{-2} in January, 150 Wm^{-2} in April, 220 Wm^{-2} in July and 35 Wm^{-2} in October. These values correspond roughly to 50 % of the values seen in this study. This seems reasonable, because the night time radiation data decreases the values. The study did not include the changes in global radiation over the years.

5.2.2 Diffuse radiation

The dependency between the diffuse fraction of global radiation and global radiation is shown in Figure 17. The measurements are collected between 10 a.m. and 3 p.m.. The diffuse fraction of global radiation shows similar patterns in April, July and October. The fraction increases as the global radiation decreases until it reaches its maximum value. The fraction remains close to one for the
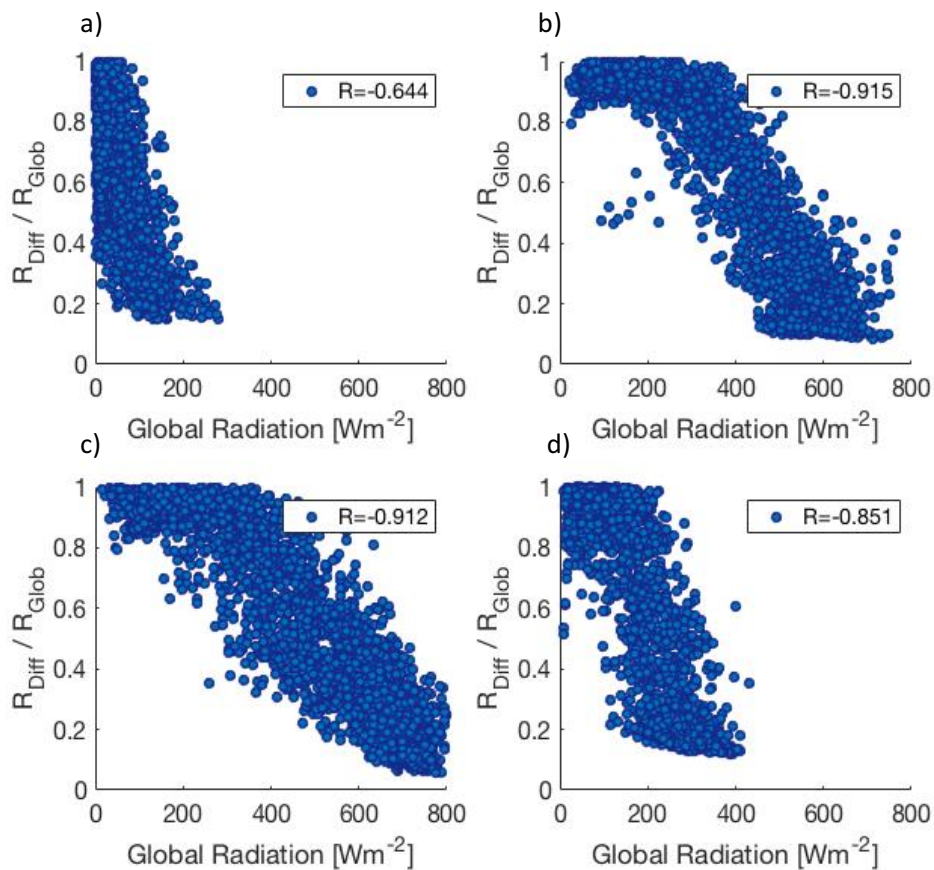
Figure 17 The dependency between diffuse fraction of global radiation and global radiation a) in January, b) in April, c) in July and d) in October.

smallest values of global radiation. These results indicate that when the sky is overcast most of the incoming radiation is diffuse radiation. In April and July there can be seen two maxima in the occurrence of measurement points; low values of global radiation corresponding to high values of the diffuse fraction of global radiation and the opposite. In October the maximum occurrence is clearly at low values of global radiation corresponding to high values of diffuse fraction of global radiation. In January the measurement points are more scattered and the pattern is not as clear as for the other investigated months. It can be seen that smaller values of global radiation lead to larger values of the diffuse fraction of global radiation. The fraction does not reach values less than 0.2 in January.

 In January and October, diffuse fraction of global radiation is detected to be above 1. This can be due to the fact that global radiation and diffuse global radiation are measured with two different instruments. The diffuse component of the global radiation may vary significantly even in near-by locations. Also the instruments are not as accurate when the incoming radiation is very low, typically during winter and autumn. Snow and ice cover can produce error to the measurements. In some cases, clouds can enhance global radiation during partly cloudy skies (Inman et al., 2016). These events are often associated with high values of global radiation and low values of the diffuse fraction of global radiation, thus these events cannot explain the values above 1 in this case.

The monthly median values of the ratio between diffuse radiation and global radiation between years 2000 and 2010 are shown in Figure 18. January and April from year 2002 are missing from the time series due to the insufficient amount of measurement points. The diffuse fraction of global radiation shows great annual fluctuation in January, April and July. Because the error bars overlap, the annual variation is not statistically significant. The fraction remains above 0.45 during the whole measurement period in January, whereas in April and in July the fraction varies between 0.2 and 0.9. October has been very cloudy on average as the ratio between diffuse global and global radiation stays between 0.9 and 1.05 during the whole time period. The fluctuation for individual years is great during all of the investigated months. The trend lines are not real, because the 95 % confidence intervals show that slopes do not differ from zero statistically.

The mean and median values for the diffuse fraction of global radiation are 0.73 and 0.76 in January, 0.57 and 0.58 in April, 0.56 and 0.54 in July, 0.83 and 0.97 in October. A seasonal pattern can be detected for the diffuse fraction of global radiation with the maximum values measured in October and the minimum values measured in July. The seasonal variation is not statistically significant, because the error bars overlap. The diffuse fraction of global radiation is an indicator of the cloudiness; small values represent clear skies and high values represent overcast skies. The seasonal

differences in the diffuse fraction of global radiation indicate that the overcast skies occur more likely during autumn and winter time than during spring and summer. These results agree with cloud occurrence estimations from ceilometer, which were previously shown in this study.
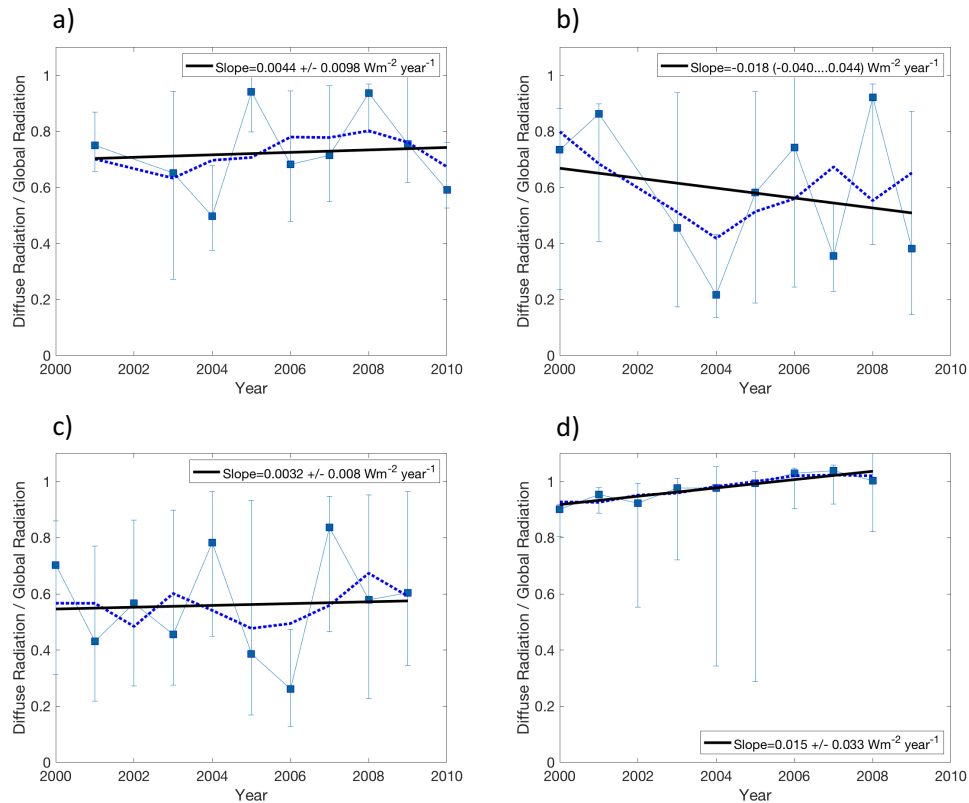

Figure 18 The monthly median value of the diffuse fraction of global radiation in a) January, b) April, c) July and d) October. The blue boxes represent the monthly median values with error bars, the blue dashed line is the three-year-sliding average and the black solid line is the trend line.

Figure 19 represents the monthly distribution of diffuse fraction of global radiation. In order to save some space, six representative years between 2001 and 2009 were chosen to show the typical distribution for each month. Each month included more than 200 measurement points, except in April 2006 there were only 191 measurement points. The figures show alteration in the distribution between different years, but some typical characteristics can be found for each month. January histograms show great alteration; some years are quite evenly distributed among the bins, but typically the peaks are located at higher values of the ratio. In April the histograms are multimodal as the peaks are found at both ends of the x-axis; at bins centred at 0.1 and 0.9 or 1.0. Smaller frequencies can be seen for the bins in between. The two maxima at the both ends of the x-axis results to the mean value of 0.57. In July the typical cloud type is light cumulus clouds, which increases the diffuse fraction of global radiation. Similarly to April, the histograms also have two maxima in July, with peaks at the both
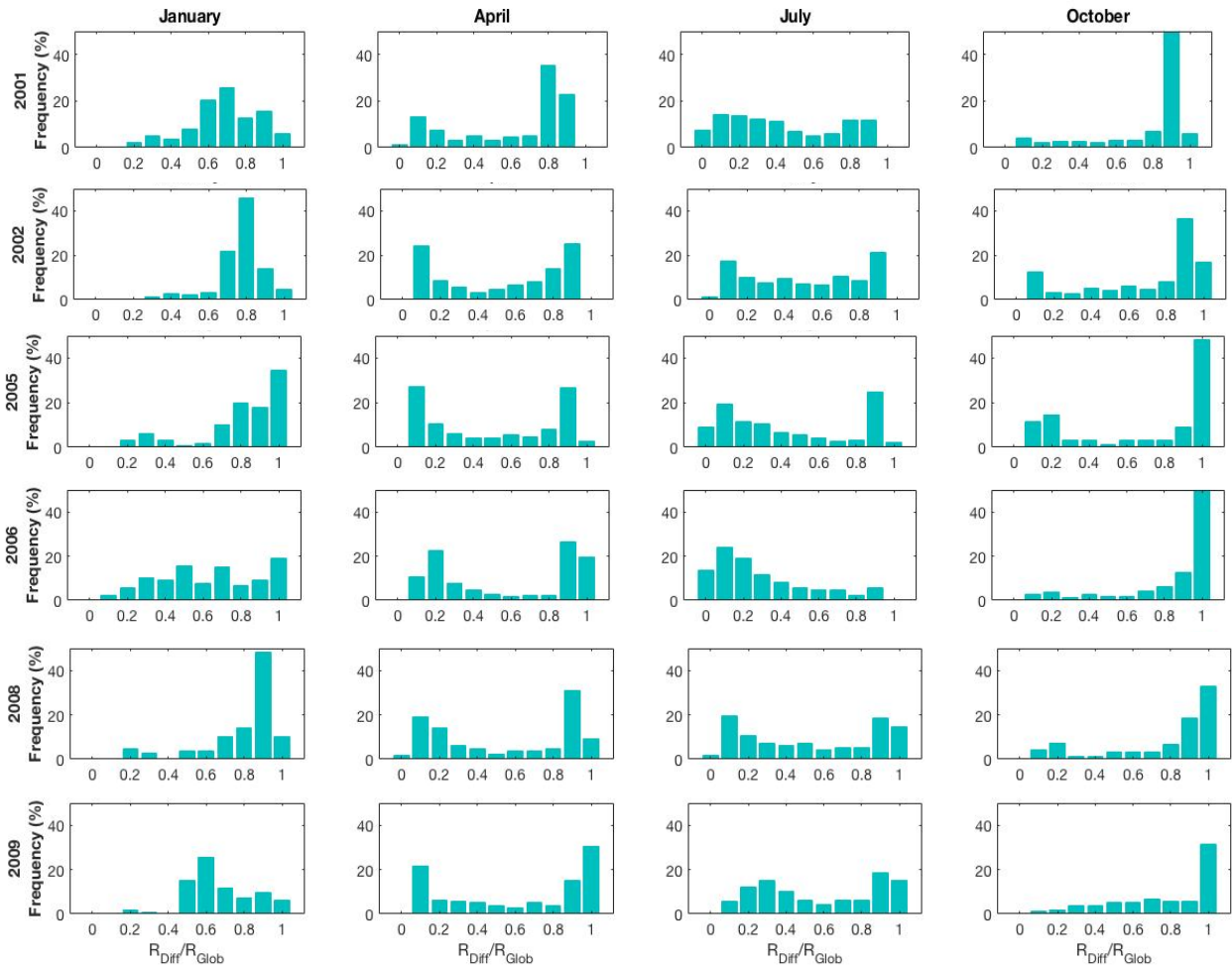
Figure 19 Distribution of the diffuse fraction of global radiation for representative years between 2001 and 2009. The distributions are shown for the representative months of all four seasons. Each bin is 0.1 wide.

ends of the x-axis. The two maxima are less pronounced than in April. Smaller frequencies are distributed quite evenly among the bins. The mean value of diffuse fraction of global radiation (0.56) results from the two maxima at the two ends of the x-axis. As was seen in Figure 18d, the monthly median value of the diffuse fraction of global radiation in October has been high for the whole measurement period. The histograms in October are rather similar with the maximum at the bins centred at 0.9 and 1.0.

5.2.3 Reflected global radiation

The ratio between reflected fraction of global radiation and global radiation is shown in Figure 20. The reflected fraction of global radiation is the albedo of a surface and it describes reflectance properties of a particular surface. The albedo values show alteration between the different seasons. In January the measurement points are well scattered and there cannot be seen any clear patterns between albedo and global radiation. The scattered measurement points in January can be explained

with the snow cover properties and distribution, which vary from year to year. The measurement error is also higher in January, when the amount of incoming solar radiation is very low. In April albedo varies between 0.095 and 0.17 for global radiation values above 200 Wm^{-2}. For smaller values of global radiation, albedo shows higher values and more variation. The low values of global radiation associated with higher values of albedo might be due to snowy surfaces. The average time when the
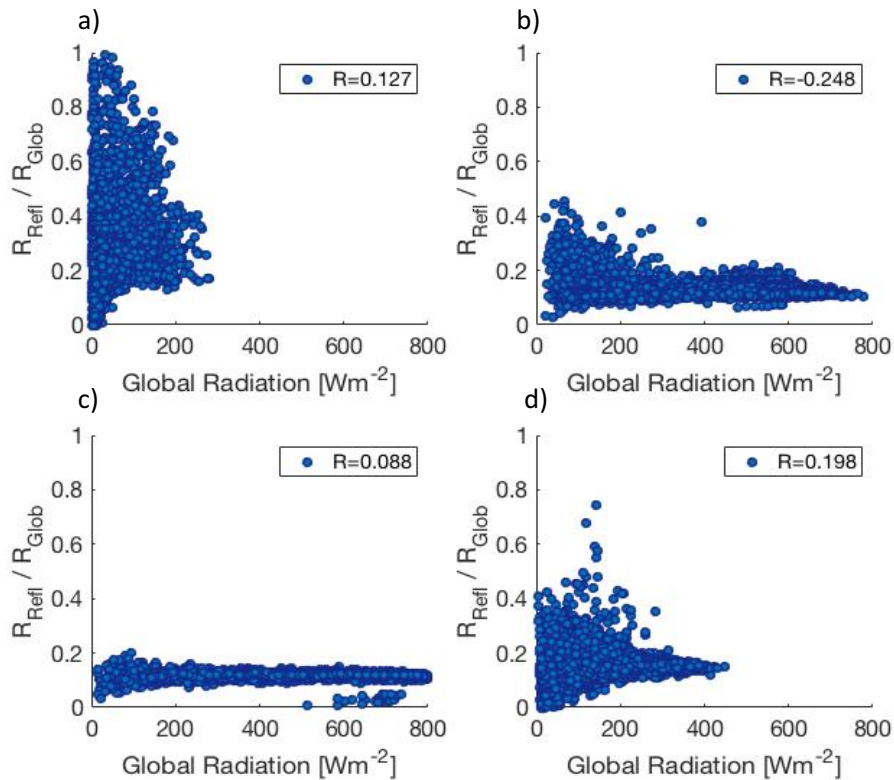

Figure 20 Relationship between reflected fraction of global radiation and global radiation in a) January, b) April, c) July and d) October. Reflected radiation is measured at 70 m measurement mast and global radiation at the 18 m old radiation tower.

snow cover melts in the region of SMEAR II station is around mid-April (FMI (Finnish Meteorological Institute), 2018b). In July albedo remains almost constant, between 0.095 and 0.13 regardless of the amount of global radiation. In October albedo shows rather constant values between 0.9 and 0.13 corresponding to higher values of global radiation. For the global radiation values below 300 Wm^{-2} the measurement points are more scattered. The variation for the measurement points with low global radiation and high values of albedo might be due to snow cover. The average time of the first snow fall in the area is around the end of October (FMI (Finnish Meteorological Institute), 2018).

The monthly median values of the ratio between reflected radiation and global radiation between years 1997 and 2011 are shown in Figure 21. January 1999, April 1998, July 1997 and 1998, October

1997, 1998 and 2011 are missing due to low amount of measurement points. The Figures 21b-d show that the annual fluctuation of the monthly median albedo at SMEAR II station is small as it varies
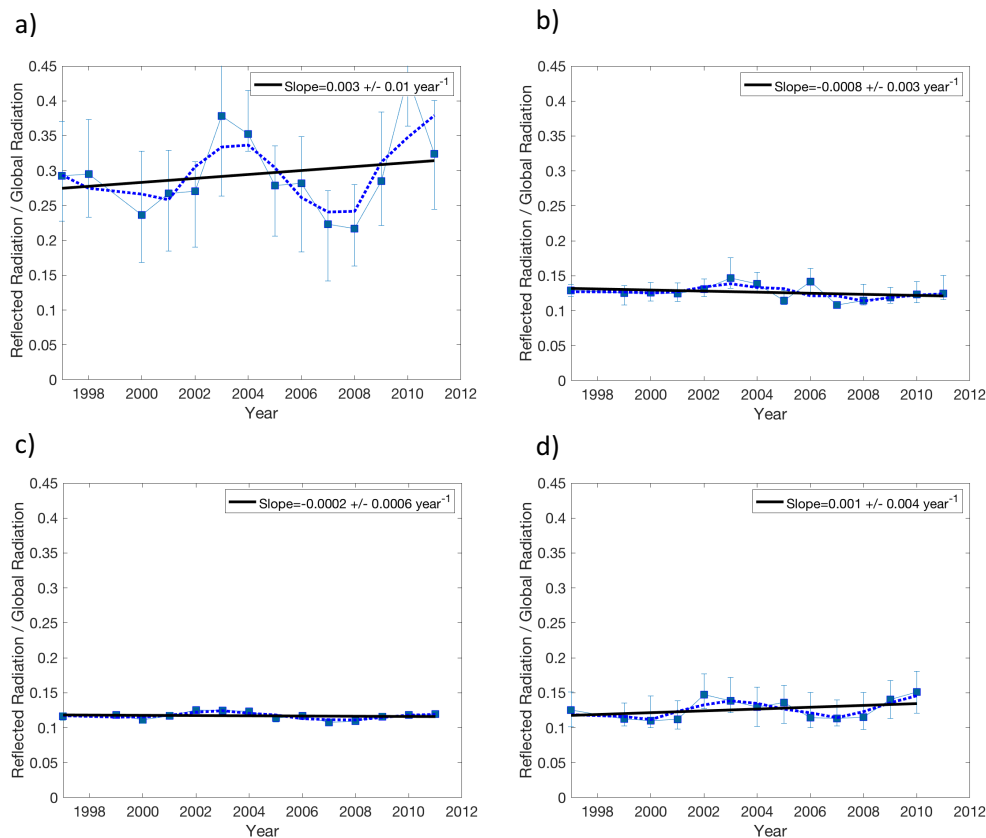

Figure 21 The monthly median value of the ratio between reflected radiation and global radiation a) in January, b) in April, c) in July and d) October. The blue boxes represent the monthly median values, the blue dashed line is the three-year-sliding average and the black solid line is the trend line. Variation for the monthly median values is presented with the error bars.

between 0.105 to 0.13 during snow free season. This means that almost 90 % of the incoming solar radiation is absorbed by the forest and the surface. The albedo increases significantly and shows more alteration when there is snow on the ground or on top of the vegetation. The maximum monthly median values of albedo are measured in January when the albedo fluctuates between 0.2 and 0.45. The annual fluctuation is not statistically significant, because the error bars overlap. The trends for the monthly median values for the albedo are not well pronounced, but the minima and maxima in April and in July coincide. The same can be seen for October and January, though the fluctuation is greater in January. This might be due to the fact that the surface properties are closer to each other in April and July and in October and January.

The mean and median values are 0.312 and 0.294 in January, 0.134 and 0.126 in April, 0.116 and 0.117 in July and 0.138 and 0.126 in October. Albedo has a seasonal pattern with the maximum during winter time and the minimum during summer time. The monthly median values show that

January differs significantly from the other investigated months. The seasonal changes in albedo are due to changes in the solar zenith angle and in the reflectance properties of the surface (e.g. snow cover and vegetation).

Kuusinen et al. (2012) studied the seasonal variation in boreal pine forest albedo at the SMEAR II station. They found that the albedo increases slightly towards the end of the growing season (May-September). The study shows also that the canopy snow cover can increase the albedo of the boreal forest by 0.2 and ground snow cover by 0.1 compared to snow free season. Winter time albedo depends on the type of snow cover and how it is distributed. The albedo of a boreal forest is lower if there is snow only on the ground than if there is snow also on top of the canopy. Also the optical properties of the snow influence the albedo of the boreal forest. This agrees with the results seen in Figure 21, when the albedo is increased up to 0.3 in January compared to July. Kuusinen et al. (2012) specified that the maximum albedos are measured during mid-winter when the cold weather enables the snow to remain on the branches and solar zenith angle is the highest. Betts & Ball (1997) show in their study that the albedo of a boreal forest is typically relatively low during all of the seasons. They measured the daily average albedo during year 1994 and 1995 at the 10 different sites in Canada. They measured albedo values of 0.2 over grass, 0.15 for aspen and 0.083 for confiner sites during summer. When there were snow below the canopy the albedo values were 0.75, 0.21 and 0.13 for the previously mentioned sites.

Boreal forests cover large areas of land in the northern hemisphere, thus the energy change associated with them is important for the global energy budget. Warming of the climate has led to changes in the vegetation which can alter the surface albedo. Additionally to the changes caused by climate change, also land use changes like deforestation have an effect on the albedo of the boreal forest. Estimating the climate effect of deforestation is a rather complex. Firstly, deforestation typically increases the forest albedo (Zhao & Jackson, 2014). Albedo increases also for snowy surfaces as the low vegetation accumulates the snow more easily than higher vegetation. This helps the snow cover to remain longer on the ground (Myhre et al., 2013). The increased amount of reflected radiation decreases the amount of net radiation, which leads to cooling of the surface temperatures. Secondly, deforestation also decreases the evaporative cooling and carbon storage in the trees. Finally, BVOC (Biogenic Volatile Organic Compounds) are emitted by the vegetation in the forests. The BVOCs have an influence on the formation of short-lived climate forcers which include ozone, methane and aerosols (Scott et al., 2018).

5.2.4 Photosynthetically active radiation

Figure 22 represents the dependency between the ratio PAR to global radiation and global radiation. These measurements correspond to instruments PAR 1 and global radiation (35 m) in Figure 6. In January the measurement points are quite scattered and there cannot be seen clear patterns as for the other investigated months. As was discussed previously with other radiation parameters, snow, ice
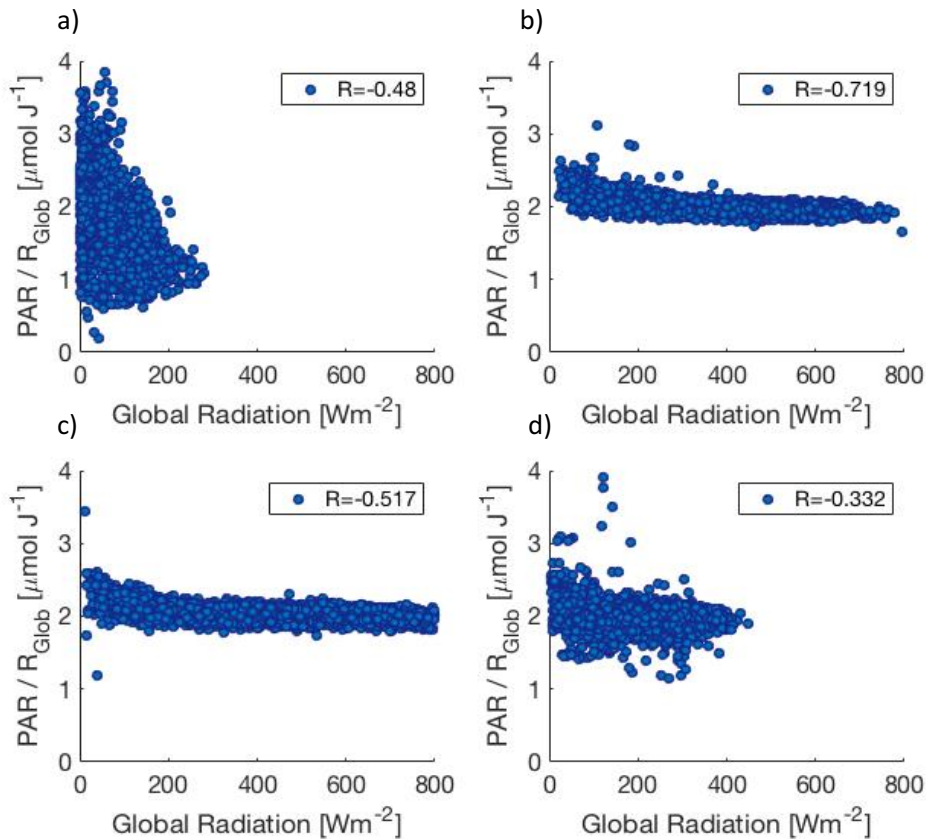

Figure 22 The relationship between the visible fraction of global radiation and global radiation a) in January, b) in April, c) in July and d) in October.

cover and low values of global radiation during winter time may cause errors to measurements. Figures 22b and 22c show similar pattern for the ratio in April and in July. The ratio between PAR and global radiation remains stable for values of global radiation above 200 $\mathrm{Wm^{-2}}$ and increases slightly for the values less than that. For larger values of global radiation, the ratio fluctuates from 1.85 $\mathrm{\mu mol\ J^{-1}}$ to 2.20 $\mathrm{\mu mol\ J^{-1}}$. For global radiation values below 200 $\mathrm{Wm^{-2}}$ the ratio PAR to global varies between 1.95 $\mathrm{\mu mol\ J^{-1}}$ and 2.6 $\mathrm{\mu mol\ J^{-1}}$. In October the measurement points are more scattered, but a similar pattern to April and July can be seen with the slight increase for the smallest values of global radiation. The increase starts at global radiation values below 50 $\mathrm{Wm^{-2}}$ and for the values above that the ratio varies between 1.85 $\mathrm{\mu mol\ J^{-1}}$ and 2.3 $\mathrm{\mu mol\ J^{-1}}$. Based on the Figures 22b-d, visible

radiation is reduced less than the total global radiation due to increased cloud cover. This agrees with previous studies, which show that water molecules and ice in the clouds absorb more efficiently in the infrared band than in the shorter wavelength band (Alados et al., 1996).

The monthly median values of the ratio PAR to global radiation are presented in Figure 23. The ratio is shown for the period from 2002 to 2017. The annual fluctuation for the monthly median values is high in January as the values vary from 1.8 µmol J^{-1} to 2.2 µmol J^{-1}, but the error bars overlap thus the annual variation is not statistically significant. Figure 23d shows similar results for October. Though the conditions are rather stable in April and in July, there is statistically significant annual variation. Even though the trend lines show increasing trends for all the seasons the trend lines are not real, because the 95 % confidence interval shows that slope does not differ from zero statistically. The annual fluctuation of the ratio between PAR and global radiation is affected by climatic conditions, precipitable water and the turbidity of the atmosphere (Alados et al., 1996). The climatic conditions vary greatly in Finland due to the active high and low pressure systems, which can explain the annual fluctuation.
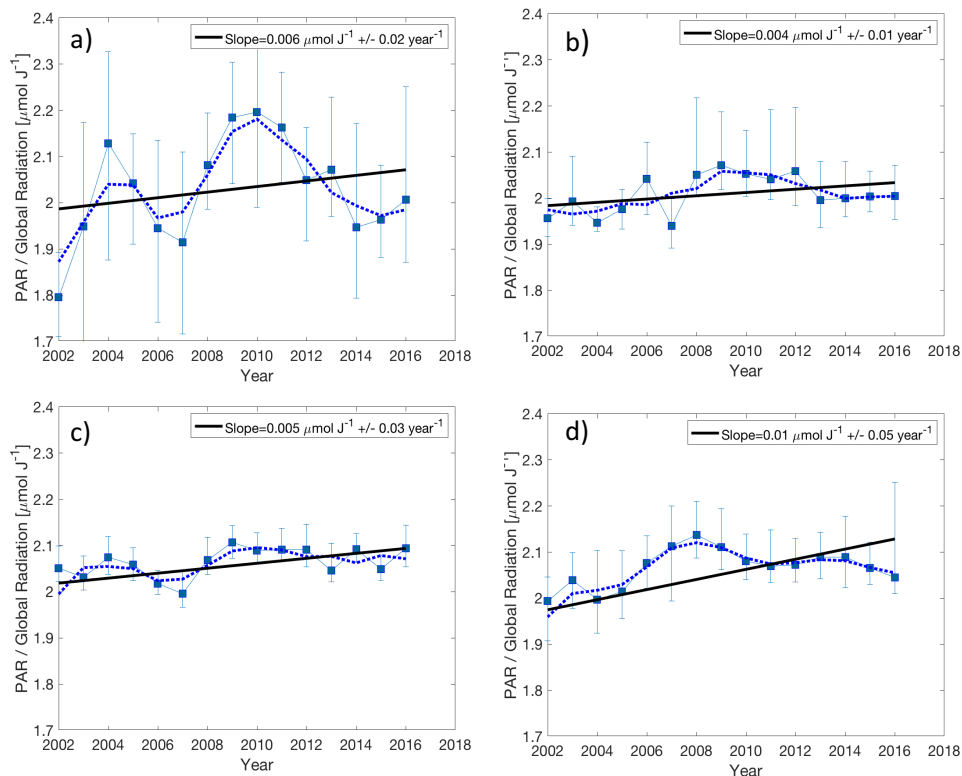

Figure 23 The monthly median value of the ratio PAR to global radiation a) in January, b) in April, c) in July and d) in October. The blue boxes represent the monthly median values with error bars, the blue dashed line is the three-year-sliding average and the black solid line is the trend line.

The mean and median values for the ratio in January are 1.97 µmol J^{-1} and 2.00 µmol J^{-1}, April 2.03 µmol J^{-1} and 2.00 µmol J^{-1}, in July 2.06 µmol J^{-1} and 2.05 µmol J^{-1} and in October 2.04 µmol J^{-1} and 2.05 µmol J^{-1}. The seasonal variation is not statistically significant for the ratio PAR to global radiation. The monthly median values are typically higher in January than during other investigated months, but the error bars are also greater. Based on the mean and median values the relative amount of visible radiation is higher during summer time than during winter. The smaller values of global radiation correspond to times when the sky is overcast. The seasonal differences of the ratio are mainly due to the changes in the solar zenith angle. The path length of the incident radiation increases due to smaller solar zenith angle. The increased path length enhances scattering which mainly affects the shorter wavelengths of the radiation spectrum.

Alados et al. (1996) studied the ratio PAR to global radiation in Almeria, South-eastern Spain. They used data from June 1990 to December 1992. Their study showed similar results to the ones shown here for the seasonal pattern of the ratio PAR to global radiation with the highest values measured during summer and the lowest values during winter time. They also calculated the first and third quartile for the monthly mean values. They show similar results that the variability associated with the monthly mean values are high during winter, spring and autumn and that the conditions are rather stable during summer months. Alados et al. (1996) also studied the effect of dew point temperature on the ratio PAR to global radiation. They found out that the ratio increased, when the dew point temperature increased. This is due to the increased extinction in the infrared part of the radiation spectrum.

5.2.5 Photosynthetically active radiation below canopy

Figure 24 shows the dependency between the fraction of PAR below canopy and PAR. The fraction of PAR below canopy is the ratio between PAR below canopy and PAR and it describes how much visible radiation is able to penetrate into the canopy. The measurements are marked as PAR below canopy 1 and PAR 1 in Figure 6. The pattern of measurement points shows some seasonal differences, but similarities can be seen in April, July and October. In April and in July the values of the fraction corresponding to higher values of PAR show more alternation than values corresponding lower values. In April the highest values of the fraction of PAR below canopy are measured between 12 a.m. and 2 p.m. and the lowest values between 10 a.m.-11 a.m. and 2 p.m.-3 p.m. In July the highest values of the fraction are recorded 11 a.m.-12 a.m. and the lowest values are recorded 2 p.m.- 3 p.m.
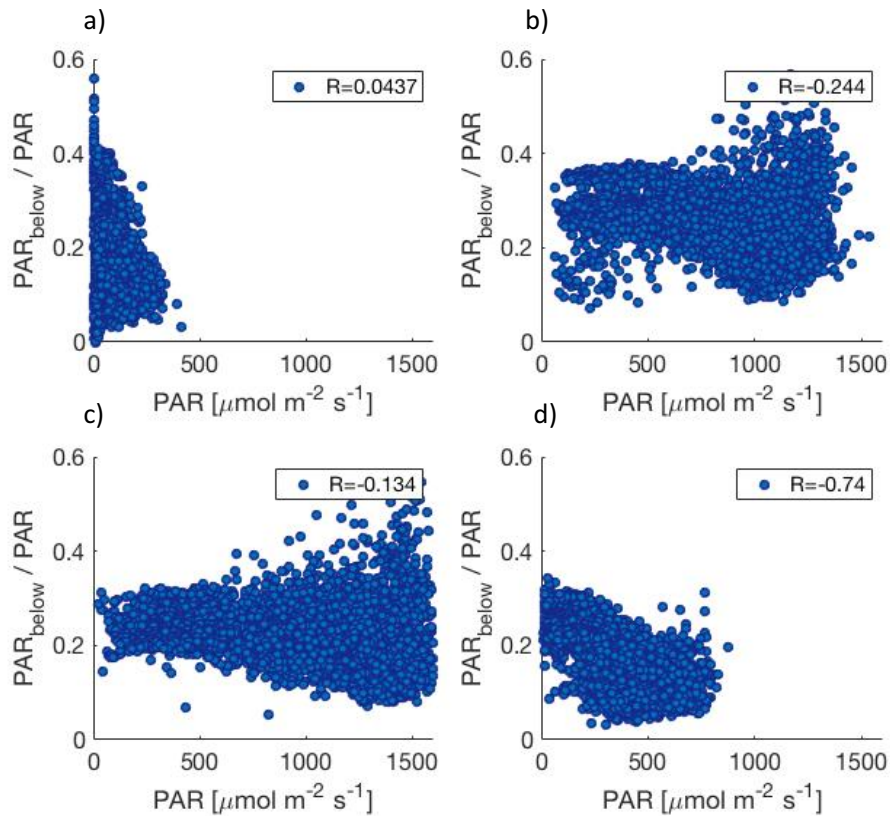
Figure 24 The relationship between fraction of PAR below canopy and PAR a) in January, b) in April, c) in July and d) in October.

In October there is a clear negative correlation between the two variables. The higher values of PAR result in lower values of fraction PAR below canopy. The measurement point corresponding to different hours are rather evenly distributed. In January the measurement points are very scattered and the ratio shows values between zero and 0.55. The radiation measurement errors are larger in January, when there is only very low amount of incoming solar radiation and snow and ice can bias the results.

The monthly median values for the fraction PAR below canopy to PAR are shown in Figure 25. April 2016 is missing because of the insufficient amount of measurement points. Figure 25 shows great annual variation in January as the monthly median values fluctuate between 0.1 to 0.27. The amount of visible radiation that is able to penetrate into the canopy during winter time is dependent on the snow cover. There can be seen some statistically significant annual variation also in April and in October. In July the error bars overlap thus the annual variation is not statistically significant. The evolution of the fraction PAR below canopy is very similar in April and in July with the maximum values measured in 2010 and 2011. Both of the previously mentioned years were exceptionally warm in July. Also April 2010 was about 1 Celsius degree and April 2011 about 2 Celsius degrees warmer

than on average between years 1981-2010 (FMI (Finnish Meteorological Institute), 2018c). Similar patterns of monthly median values can also be seen for January and October.
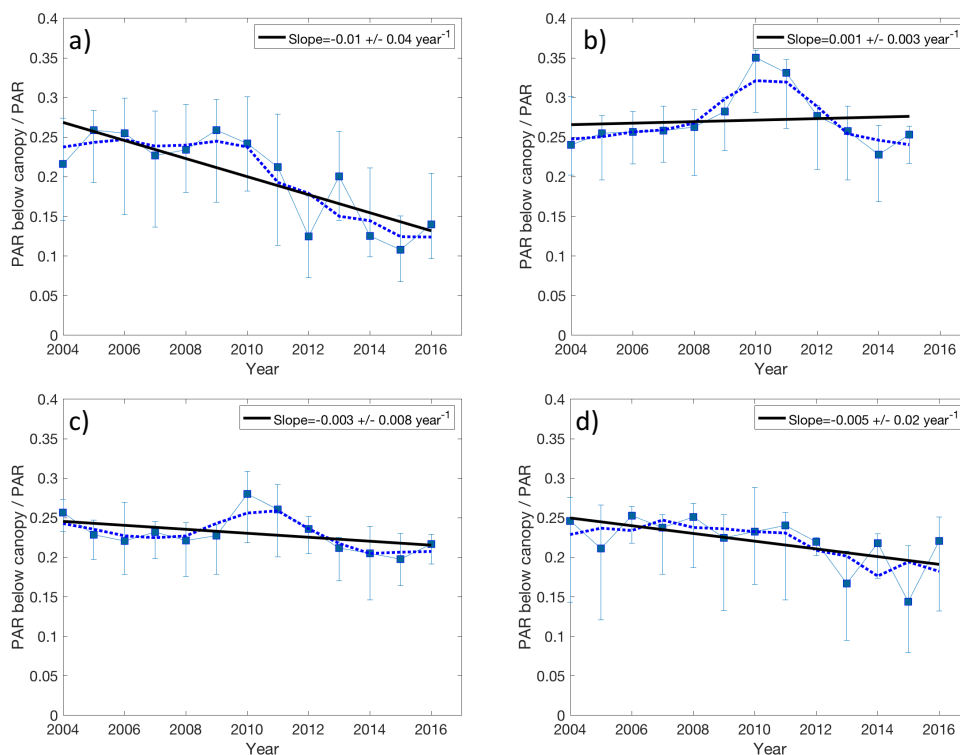

Figure 25 The evolution of the ratio between PAR below canopy and PAR a) in January, b) in April, c) in July and d) in October. The blue boxes represent the monthly median values, the blue dashed line is the three-year-sliding average and the black solid line is the trend line. Variation for the monthly median values is presented with the error bars.

The mean and median values of the ratio are 0.196 and 0.197 in January, 0.258 and 0.260 in April, 0.224 and 0.224 in July and 0.198 and 0.219 in October. The error bars show that the seasonal variation is not statically significant. Based on the mean and median values, the maximum values are measured during spring time and minimum values during winter time. Growing plants can absorb up to 90 % of the incoming visible radiation. During winter time, snow increases the albedo and less radiation is absorbed to the surface.

The dependency between the fraction of PAR below canopy and the diffuse fraction of global radiation is shown in Figure 26. The measurements correspond to PAR below 1, PAR 1 and global radiation at 35 m in Figure 6. The lower values of the fraction PAR below canopy show a linear trend in April, June and July indicating that the fraction of PAR below canopy increases as the cloud cover blocking the solar radiation increases. Similar results can be seen be seen for the other PAR below canopy measurements. When the sky is clear or when there are only some clouds, the higher values of the fraction PAR below canopy show more variation. In January the measurement points are more scattered.
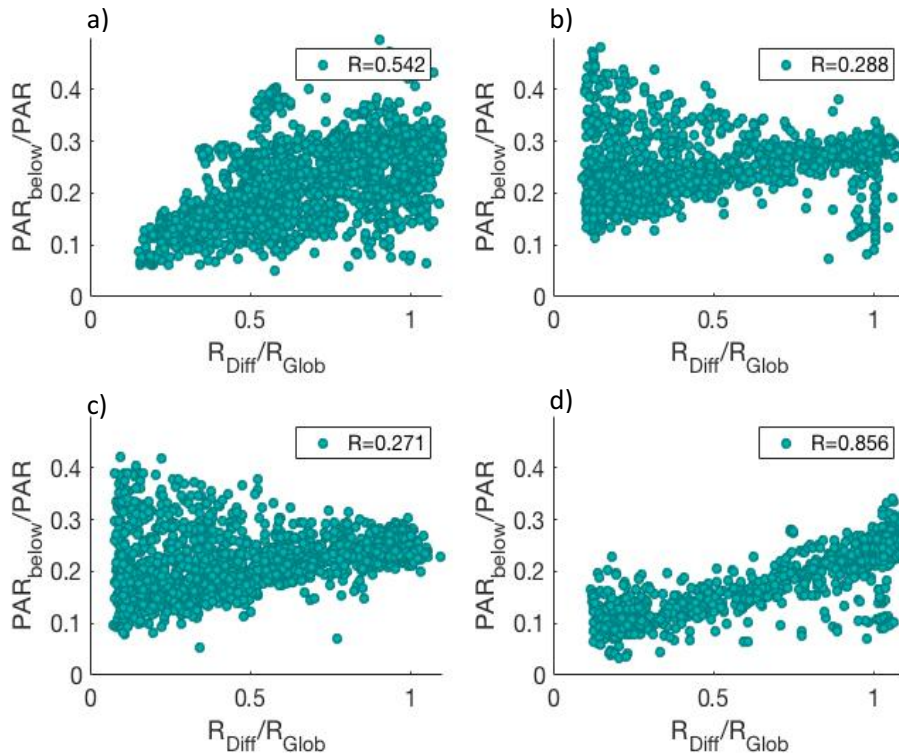
Figure 26 The dependency between the fraction of PAR below canopy and the diffuse fraction of global radiation a) in January, b) in April, c) in July and d) in October.

The physiological condition and texture of the canopy determines how much radiation can access through the canopy (Hartmann, 2016). Thus the measurements of PAR below canopy are highly dependent on the location and the surrounding vegetation. The instruments measuring PAR below canopy at the SMEAR II station are located in a pine forest, where the trees have needles year-round. The majority of the below canopy vegetation is deciduous vegetation, for example blueberries and smaller trees. Growth of the foliage may explain why the fraction shows slightly decreasing values. Also the climatic conditions affect how much of the incoming visible radiation comes as direct radiation. The different PAR below canopy instruments show differing patterns for the monthly median values because the location has a great impact on the fraction of PAR below canopy (see appendices). The dependency between different PAR below canopy measurements is shown also in the appendices. The values from differ especially in April and in July for larger values of PAR. The scattering is due to the different type of vegetation around the instruments and the effect of solar zenith angle.

As was discussed previously in the analysis of reflected radiation (section 5.2.3), the changes in land use and vegetation will influence the surface albedo. In the case of visible radiation, the effect of vegetation is very important.

5.2.6 Total UV-radiation

Figure 27 represents the dependency between the UV fraction (UV-A and UV-B radiation) of global radiation and global radiation. It should be noted that global radiation measurement (0.3-4.8 µm) does not cover UV-B radiation completely (0.28-0.32 µm). Similar pattern can be seen for all the four investigated months; the fraction of total UV-radiation increases when global radiation decreases similarly to the ratio PAR to global radiation. The highest values of the ratio (close to 0.2) are measured in January. The pattern for the fraction of UV radiation is clear also in January, which was not the case for PAR. The instruments accuracy is not as reliable during winter time as during summer time. This is due to the very low amounts of incoming radiation and snow and ice cover. The fraction of the total UV radiation varies between 3-20 % in January, 4.7-10 % in April, 5.2-11 % in July and 4-12 % in October. The mean and median values for the fraction of UV radiation are 7.89 % and 8.04 % in January, 6.37 % and 6.07 % in April, 6.87 % and 6.63 % in July and 6.73 % and 6.86 % in October.

The lowest values of the global radiation correspond to overcast skies. The longer wavelengths in the global radiation are more reduced due to absorption by the water droplets and ice in clouds than the shorter UV radiation. Jacovides et al. (2006) showed that during the hazy days and when there were lot of aerosols in the air, the fraction of UV radiation reached its minimum values. The shorter wavelengths are more affected by the absorption and scattering processes in hazy or dusty conditions than the longer wavelengths, which leads to larger reduction in the amount of UV radiation than in the global radiation. The diffuse radiation spectrum is shifted towards the infrared part of the radiation spectrum due to the scattering processes. Compared to previously shown figures for PAR (Figures 23a-d), the fraction of total UV-radiation increases almost constantly when global radiation starts to decrease. The fraction of visible radiation remained stable first or increased only a little and the greatest increase was seen for the smallest values of global radiation. The albedo corresponding to UV radiation is relatively small for most surfaces (approximately 4 %), but the albedo increases significantly when there is snow on the ground (Kerr, 2005).
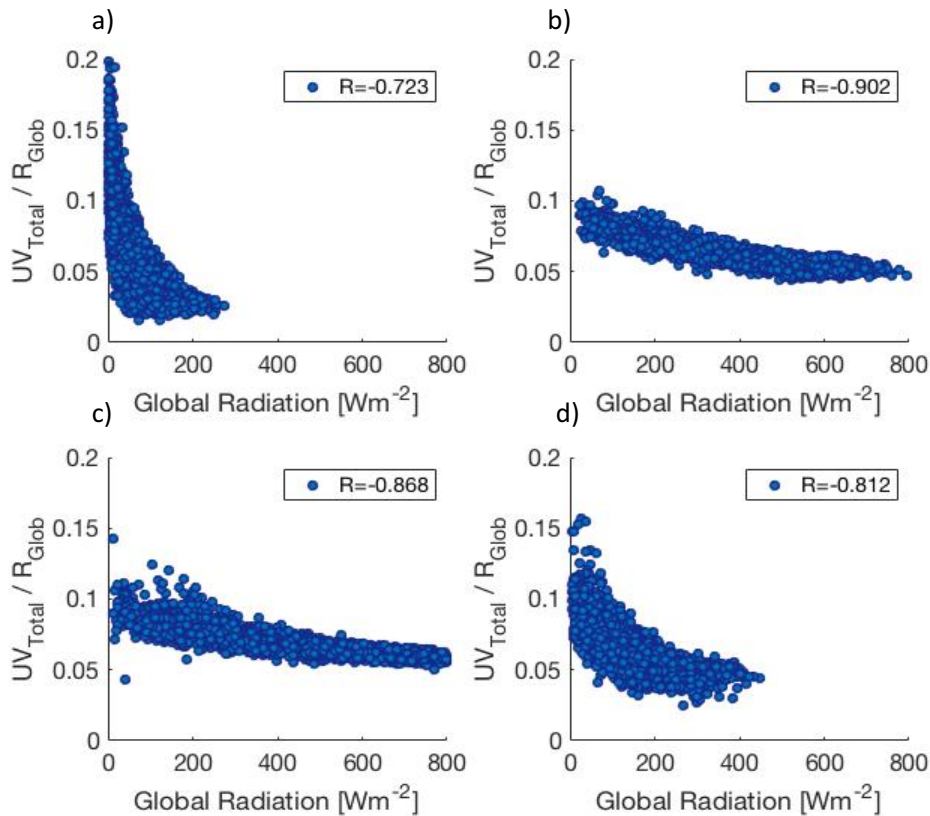
Figure 27 The relationship between the ratio total UV-radiation/ global radiation and global radiation a) in January, b) in April, c) in July and d) in October.

Jacovides et al. (2006) studied the ratio of UV to global radiation in Cyprus during the year 2004. The wavelength band for UV radiation which they measured is narrower (280-380 nm) than the one measured at the SMEAR II station (280-400 nm). The study by Jacovides et al. (2006) showed that the mean values of UV fraction in Cyprus were 3.09 % in January, 3.31 % in April, 2.98 % in July and 3.57 % in October. Other studies done in the Mediterranean area show similar results. The results indicate that the fraction of UV radiation is almost or more than twice as high at the SMEAR II station compared to the measured values in Cyprus. The alternation between different locations can be explained with the effect of solar zenith angle and climatic conditions. Also the fact that the global radiation measurement at SMEAR II station does not cover the complete wavelength range of UV-B radiation bias the results higher. In the following sections the time series of the fraction of UV-A and UV-B radiation and the parameters that influence their transfer in the atmosphere are investigated separately.

5.2.7 UV-A radiation

Figure 28 shows the monthly median ratio of UV-A to global radiation for the time period between 1999 and 2016. January 1999 and 2002 and April 2002 and 2006 did not have sufficient amount of

measurement points. The annual fluctuation is great in January, April and October. The fluctuation within each year is high in January and in October. However, the error bars from different years overlap and the variation is not statistically significant. The monthly median values of the fraction of UV-A radiation have remained relatively stable in July.

The ratio of UV-A radiation to global radiation has mean and median values of 7.66 % and 7.82 % in January, 6.10 % and 5.80 % in April, 6.52 % and 6.28 % in July and 6.48 % and 6.60 % in October. Based on these values the maximum values of the fraction of UV-A radiation are measured in January and the minimum values in April. The seasonal variation is not statistically significant for the fraction of UV-A radiation. The monthly median values are typically higher in January than during other investigated months, however the error bars are also greater. The cloud occurrence at the measurement station is the highest during winter time which coincides with the time when the highest values of the fraction of UV-A radiation are measured. On the other hand, in April the cloud occurrence is lower and the water vapour content of the atmosphere is very low after winter, which explains the low values of the fraction in April.
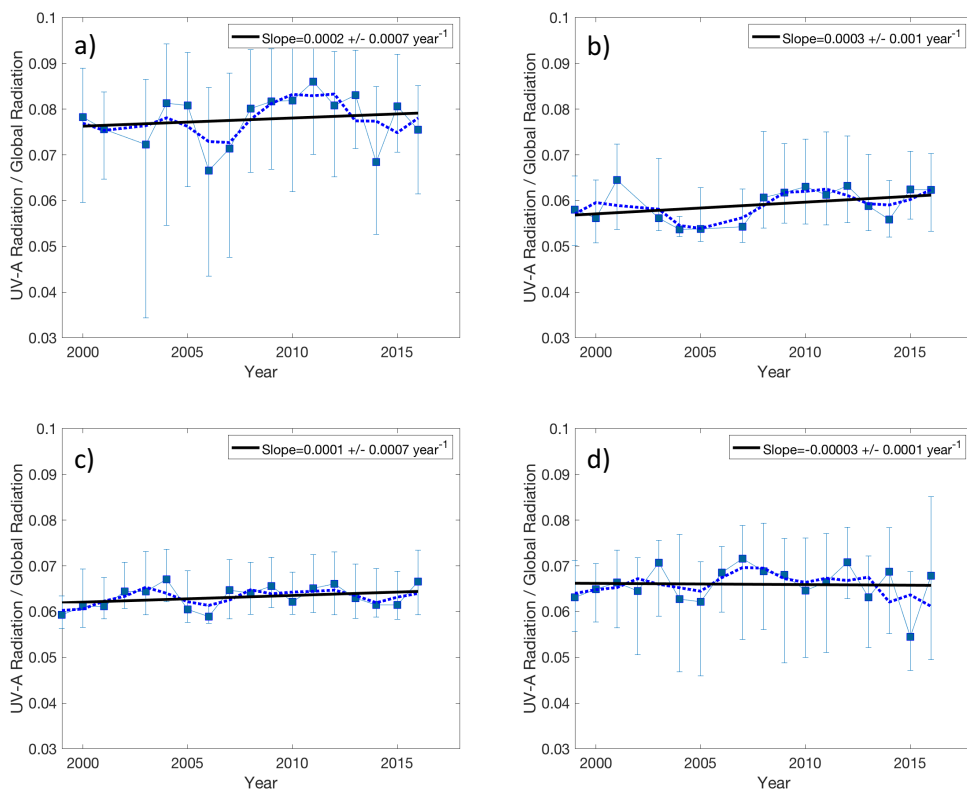

Figure 28 The time series representing monthly median fraction of UV-A radiation from global radiation a) in January, b) in April, c) in July and d) in October. The blue boxes represent the monthly median values, the blue dashed line is the three-year-sliding average and the black solid line is the trend line. Variation for the monthly median values is presented with the error bars.

Atmospheric gases absorb only little UV-A radiation (Kerr, 2005). The seasonal trends of the cloud occurrence may explain why the fraction of UV-A radiation has its maximum in January. The changes in the cloud cover between years 2015 and 2017 at SMEAR II station were shown in Figures 13 and 14. The figures show that December and January have been the cloudiest months during the measurement period. There is annual fluctuation in cloud occurrence, but all the investigated years show cloudier winter than summer time. Atmospheric water vapour and water droplets and ice crystals in the clouds absorb more efficiently in longer wavelength bands rather than in the shorter UV radiation bands. Even though the absolute amount of UV radiation is reduced global radiation is reduced relatively more, which increases the fraction of UV radiation (Ambach et al., 1991). The minimum values for the fraction UV-A radiation are measured in April, because both the atmospheric water vapour content and cloudiness are low. The water vapour content of the atmosphere increases towards the summer, which leads to increased values of the fraction of UV-A radiation.

5.2.8 UV-B radiation

Figure 29 shows the monthly median values of the ratio UV-B to global radiation between years 1997 and 2017. January 1997, 1999, 2002 and 2007, April 1998, 2002, July 1998 and 1999 and October 1998 are missing due to the insufficient amount of measurement points. All of the investigated months show increasing trends and the slopes are rather steep in January and October, but the uncertainties of the trend lines are higher than the slopes. There is statistically significant annual variation in January and April. In October and in April, the error bars overlap therefor the annual variation is not significant.

The mean and median values for the fraction of UV-B radiation are 0.18 % and 0.18 % in January, 0.27 % and 0.26 % in April, 0.36 % and 0.35 % in July and 0.25 % and 0.24 % in October. Because global radiation does not cover the total UV-B wavelength range, the real fractions are smaller. The seasonal variation is more pronounced before year 2005. After that the increasing monthly median values in January and October reduces the seasonal differences. The maxima and minima of the fraction of UV-B radiation in April and in July occur approximately during the same periods of time.

The time series of UV-B radiation is represented in Figure 30 to further investigate if the actual amount of UV-B radiation has increased. The figures show similar results to the previously shown figures for the fraction of UV-B radiation. All of the months show increasing trend lines and the slopes are steep during January and October. There is small annual fluctuation in the monthly median values during all seasons. The trend lines are not statistically significant, because the 95 % confidence interval shows that slope does not differ from zero statistically. For the relationship between UV-B

radiation and global radiation the maxima and minima were found during the same years in April (Figure 29b) and in July (Figure 29c). This cannot be seen in the time series of UV-B radiation (Figure 30b-c).
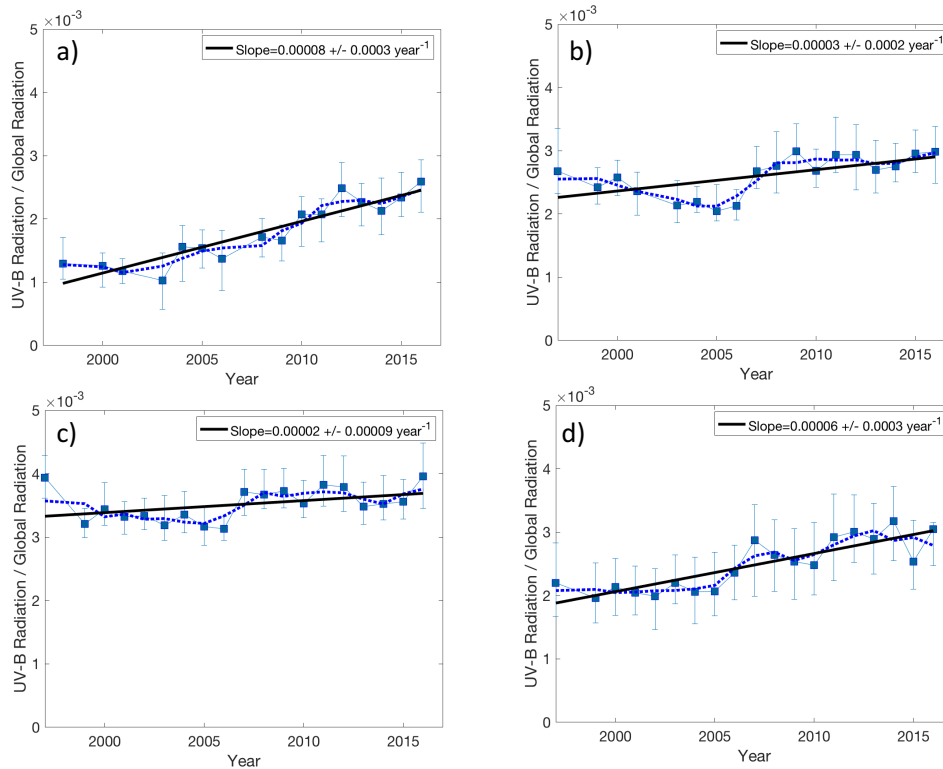

Figure 29 The time series representing monthly median fraction of UV-B radiation from global radiation a) in January, b) in April, c) in July and d) in October. The blue boxes represent the monthly median values, the blue dashed line is the three-year-sliding average and the black solid line is the trend line. Variation for the monthly median values is presented with the error bars.

The mean and median values of UV-B radiation are 0.06 Wm^{-2} and 0.04 Wm^{-2} in January, 0.95 Wm^{-2} and 0.96 Wm^{-2} in April, 1.56 Wm^{-2} and 1.63 Wm^{-2} in July and 0.28 Wm^{-2} and 0.24 Wm^{-2} in October. The seasonal trends for the fraction of UV-B radiation differ from the trends for the fraction of UV-A radiation. The maximum values of the fraction of UV-A radiation were measured in January and minimum values in April, whereas the maximum values for the UV-B radiation and fraction of UV-B radiation are measured in July and minimum values in January. The fraction of UV-B and UV-B radiation follow the seasonal pattern of global radiation.

The last two sunspot cycle maxima were measured in 2001 November and in 2014 April (NASA (National Aeronautics and Space Administration), 2017). During the sunspot maxima the incoming radiation in the shorter wavelengths is increased due to the solar flares and eruptive prominences. The increase due to the active sunspot period cannot be clearly seen in the time series during any of the investigated months.
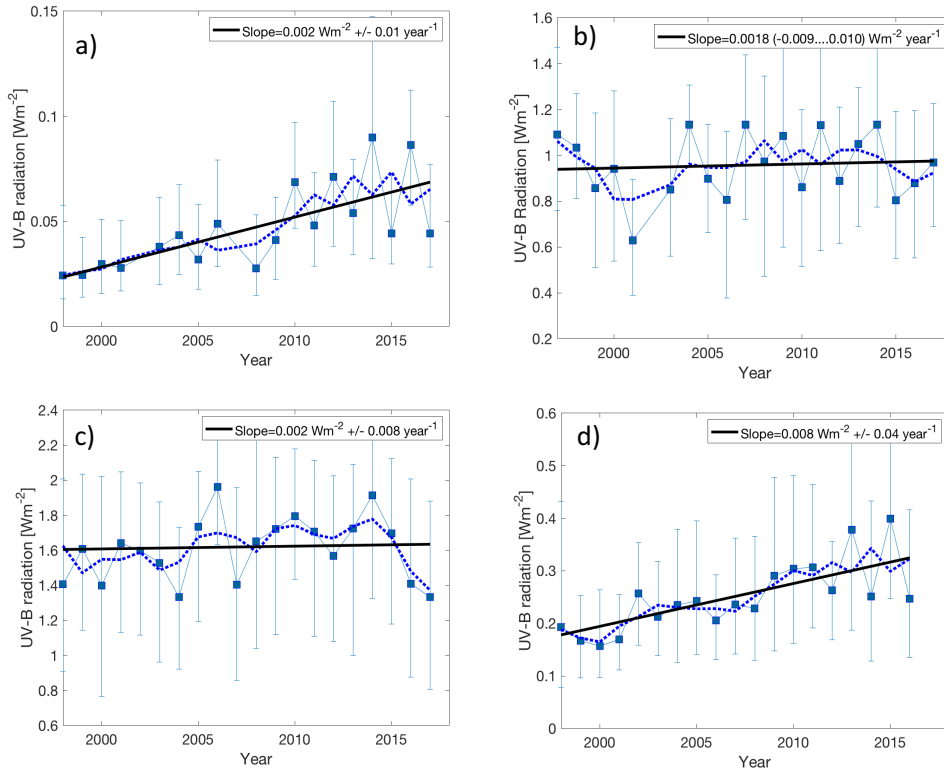
Figure 30 The time series of UV-B radiation a) in January, b) in April, c) in July and d) in October. The blue boxes represent the monthly median values, the blue dashed line is the three-year-sliding average and the black solid line is the trend line. Variation for the monthly median values is presented with the error bars.

UV-B radiation is effectively absorbed in the atmosphere by ozone, nitrogen dioxide and sulphur dioxide. The strong correlation between lower stratospheric ozone concentration and higher amounts of UV-B radiation has been extensively shown in previous studies (Kerr & McElroy, 1993). The stratospheric ozone depletion started from the 1980's due to the usage of ozone depleting substances. In the mid-latitudes the stratospheric ozone concentration decreased approximately 6 % between years 1979 and 1995. According to the WMO assessment of ozone depletion (Pawson et al., 2014) from year 2014 the observations between years 2000 and 2013 show only small decreases in the stratospheric ozone concentration between the latitudes 30°N and 80°N. The decreases are observed at height below 32 km. The study shows that the decreases in the stratospheric ozone concentration are not statistically significant. According to the assessment the ozone concentration is 3.5 % lower than 1964 -1980 average concentration. The stratospheric ozone concentration is lowest during winter and spring time and highest during summer and autumn in the northern mid-latitudes.

UV-B radiation measured at the SMEAR II station does not seem to follow the seasonal trends of stratospheric ozone concentration. The maximum values for UV-B radiation and for the fraction of UV-B radiation are measured in July, when the stratospheric ozone concentration is also high and the minimum values of UV-B radiation are measured in January when the stratospheric ozone

concentration is low. According to the previous studies the high ozone concentration should lead to lower values of UV-B radiation.

Brühl & Crutzen (1989) studied the role of tropospheric ozone on UV-B radiation. They show in their study that the increased tropospheric ozone concentration could compensate the increased UV-B radiation due to lower stratospheric ozone concentration. This enhancement could especially be seen during summer, when most of the UV-B radiation comes as diffuse radiation. The aerosols and particles in the air increase the optical path of UV-B radiation in the troposphere (Brühl & Crutzen, 1989). The tropospheric ozone concentration is the highest during spring and the lowest during winter at the SMEAR II station, thus the seasonal cycle of tropospheric ozone does not explain the seasonal cycle of UV-B radiation.

Brühl & Crutzen (1989) state also that the increased concentration of NO_x enhances the production of tropospheric ozone. The main source of NO_x in Finland is the transport, industrial combustion and power plants (Karvosenoja & Johansson, 2003). The life time of NO_x in the troposphere is approximately one day. Majority of the NO_x emission are produced in the southern parts of Finland. The air masses coming from the west and south directions passing over St. Petersburg or the Baltic countries are the main reasons for high concentrations of NO_x at the SMEAR II station (Riuttanen et al., 2013). These transported polluted air masses can act as a source of ozone in the spring time when there is enough incoming solar radiation. The highest concentrations of NO_x are measured during winter and spring at the SMEAR II station. The increased emissions are due to closer sources of emissions for example due to the increased heating during winter time. NO_x concentration is very low during summer (Kulmala et al., 2000). The seasonal cycle of NO_x cannot explain the seasonal cycle of UV-B radiation.

The influence that clouds have on the UV-B radiation can vary from small increments to nearly total reduction. Geometry and location with respect to the Sun are the factors which influence the effect clouds have on UV-B radiation (Calbó et al., 2005). Cloud occurrence is highest during winter time, when the minimum values for the fraction of UV-B radiation are measured. The minimum cloudiness is measured during summer time, when the maximum values of the fraction of UV-B radiation are measured. Based on the fact that clouds reduce effectively longer wavelengths of the global radiation, it is expected that the fraction of UV-B radiation would reach higher values during winter time when the cloud occurrence is high and lower values during summer and spring time when the cloud occurrence is lower.

Because UV-B radiation drives many photochemical reactions in the troposphere, it is important to know how it behaves and how it has changed over the years. Though the trends for UV-B radiation were not statistically significant, the monthly median values are higher at the end of the time series in January. UV radiation has enough energy to break chemical bonds and the increased UV radiation enhances the chemical reactivity in the troposphere. Higher concentrations of OH radical would lead to shorter life times of many tropospheric gases and ultimately faster production of peroxides. In low NO_x areas the destruction of tropospheric ozone has increased (Madronich & Flocke, 1999; Romer et al., 2018) .

There are large uncertainties associated with estimation of global UV-radiation trends due to lack of long term measurements and globally distributed measurements. The masking effects of changes in the cloud cover and aerosol load due to anthropogenic emissions may increase the difficulties in estimating the UV-radiation trends (Calbó et al., 2005).

5.2.9 Incoming infrared radiation

Figure 31 shows the dependency between the ratio of incoming IR radiation and global radiation vs global radiation. The patterns of measurement points are similar during all of the investigated months. The highest values of the ratio are measured in overcast situations. The lowest values of global radiation correspond to overcast skies, indicating that clouds emit effectively IR radiation to the surface. Because the water droplet is clouds absorb effectively in the infrared part of the solar spectrum, the global radiation is reduced. During clear skies (high values of global radiation) the incoming IR radiation remains lower. In January and in October incoming IR radiation is close to hundred times higher than incoming global radiation in overcast situations at the SMEAR II station. Very low values of incoming solar radiation may bias the results in January.

Figure 32 represents the monthly median values of the ratio incoming IR radiation to global radiation for the four investigated months. The time series covers years 2010 to 2016. January 2012 and 2013 and April 2012 and 2016 are missing due to the insufficient amount of measurement points. The annual fluctuation of monthly median values is high in January (Figure 32a) with the minimum value of the ratio being 5 and the maximum value being 14. The annual variation is not statistically significant. The measurement errors are greater in January, when there can be snow and ice cover which can bias the results. Similar results can be seen for October, though the annual fluctuation is significantly smaller than in January. The conditions have remained very stable in April and in July as the ratio is close to 1.
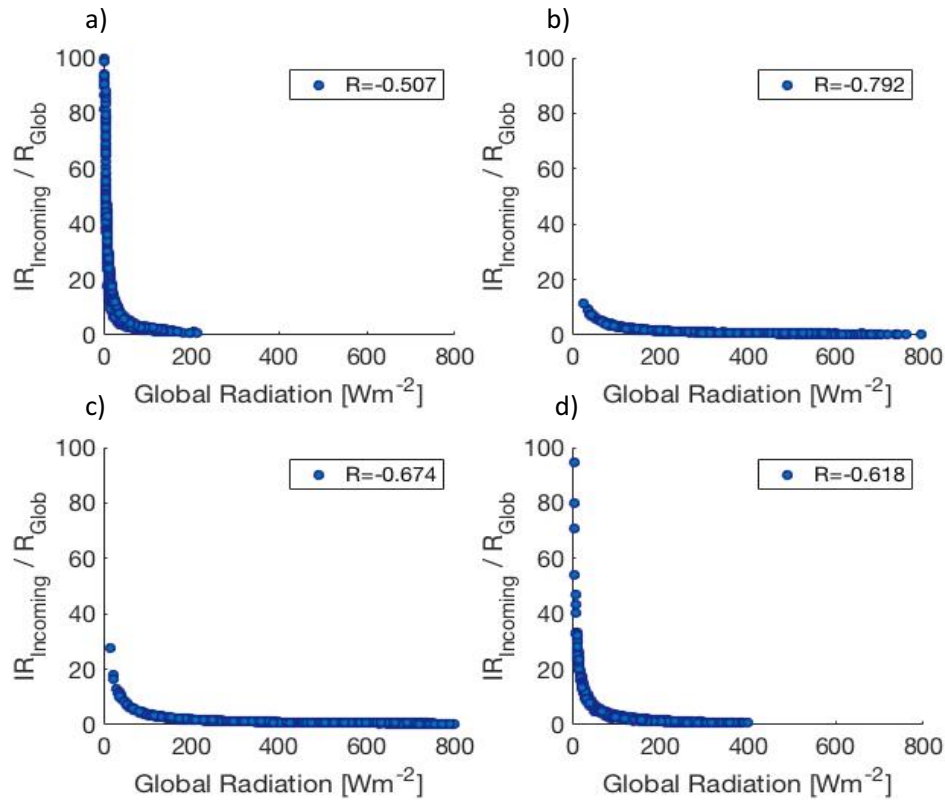
Figure 31 The dependency between the ratio of incoming infrared radiation and global radiation vs global radiation a) in January, b) in April, c) in July and d) in October.

The mean and median values of the ratio between incoming IR radiation and global radiation are 15.21 and 9.03 in January, 1.34 and 0.81 in April, 1.22 and 0.79 in July and 4.95 and 2.57 in October. The maximum values of the ratio are measured in January and the minimum values in July. The monthly median values of the ratio in January and October differ significantly from the values in April and in July. Incoming IR radiation is significantly higher than global radiation during winter time. This means that more radiation is emitted by the atmosphere and clouds than is received from the Sun. During summer time incoming IR radiation remains on average lower than global radiation.

The increment of incoming IR radiation due to clouds depend on several factors. The cloud temperature, which depends on the height of the cloud, determines how much radiation is emitted according to blackbody approximation. Low and mid-level clouds are warmer than high clouds, because of their lower height. The cloud opacity also influences the emission rate. Low and mid-level clouds are usually more opaque than high clouds, because of their high water vapour content. Also the water vapour distribution below the cloud effects the downward longwave radiation reaching the surface. The water vapour below the clouds can reduce the effect of clouds by absorbing and re-emitting the radiation with a warmer temperature. The area of the cloud influences the amount of

emitted radiation (Stephens et al., 2012). Under clear sky conditions incoming IR radiation depends mainly on the temperature and humidity profiles of the lower atmosphere (Wang & Dickinson, 2013).
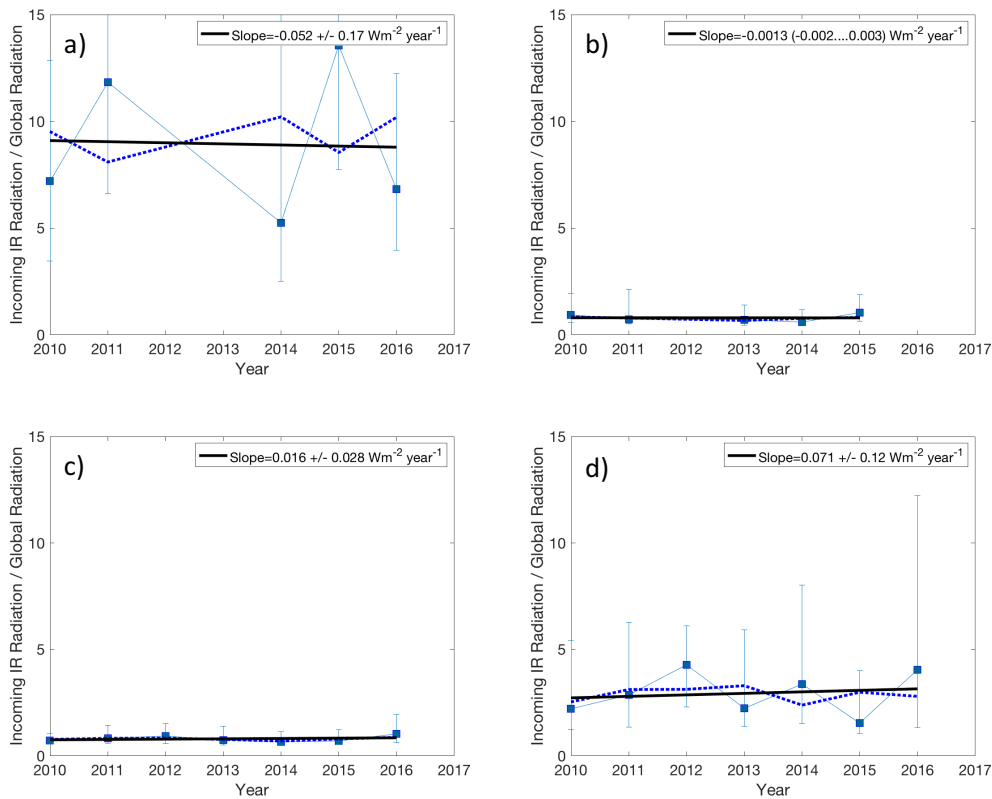

Figure 32 The monthly median value of the ratio between incoming IR radiation and global radiation a) in January, b) in April, c) in July and d) in October. The blue boxes represent the monthly median values, the blue dashed line is the three-year-sliding average and the black solid line is the trend line. Variation for the monthly median values is presented with the error bars.

Water vapour is the dominant gas affecting radiation transfer in the wavelength band above 15 μm. CO_2 absorbs only efficiently in the high frequency part of this wavelength band. The absorption by other atmospheric gases is low compared to absorption by water vapour. Because there is so much absorption of longwave radiation in the lower troposphere, the atmosphere is basically opaque in this region and no radiation is able to escape to space. The result is that the majority of the longwave radiation escaping to space is from the upper troposphere and stratosphere. The temperature of these regions is lower than at the Earth's surface.

In order to investigate the effects of water vapour and carbon dioxide on incoming infrared radiation, the mean and median values at SMEAR II station (at 33 m measurement mast) for the two parameters are calculated for the time period 2010-2017. The water vapour concentration is given in unit parts per thousand in volume (ppth). The mean and median values for water vapour concentration are 3.53 ppth and 3.39 ppth in January, 5.33 ppth and 5.54 ppth in April, 13.15 ppth and 13.12 in July and 7.58 ppth and 7.63 ppth in October. The water vapour concentration has a pronounced seasonal cycle.

The highest values are measured during summer time and autumn. Winter and spring time are typically drier. The seasonal cycle of water vapour agrees with the seasonal cycle of incoming IR radiation. The highest values of incoming IR radiation are measured during July and October, when the water vapour concentration is the highest.

The mean and median values of CO_2 are 407.5 ppm and 407.0 ppm in January, 401.9 ppm and 402.3 ppm in April, 386.8 ppm and 386.7 ppm in July and 397.0 ppm and 397.1 ppm in October. CO_2 has a seasonal cycle with the maximum values measured in January and minimum values during summer. Because CO_2 is less abundant greenhouse gas than water vapour, the seasonal cycle of CO_2 and incoming IR radiation do not correlate.

According to previous studies the estimated changes in the climate are going to have the greatest effect on downward longwave radiation out of all the parameters in the energy budget. As the atmospheric concentration of the greenhouse gases like carbon dioxide increases, the atmosphere gets warmer. The warmer atmosphere can hold more water vapour, which radiates more longwave radiation back to the Earth's surface. The incoming longwave radiation warms the surface temperatures. This is called the water vapour feedback of the atmosphere (Stephens et al., 2012). Both moistening and warming of the lower atmosphere contribute to the increase of water vapour feedback, which again increases the downward longwave radiation. Changes in the downward longwave radiation will cause changes in the global precipitation (Stephens et al., 2012).

5.2.10 Outgoing infrared radiation

Figure 33 shows the dependency between the ratio of outgoing IR radiation and global radiation vs global radiation. The pattern of measurement points is similar to the previously shown figure for incoming IR radiation (Figure 31). The highest values of the ratio are measured in overcast situations, when the outgoing IR radiation can be up to hundred times higher than global radiation in January. The measurements are not as reliable during winter time, when snow and ice and very low amounts of global radiation can cause error to the measurements. The influence of clouds remains smaller in April and in July. For higher values of global radiation, the ratio remains stable during all of the investigated months.
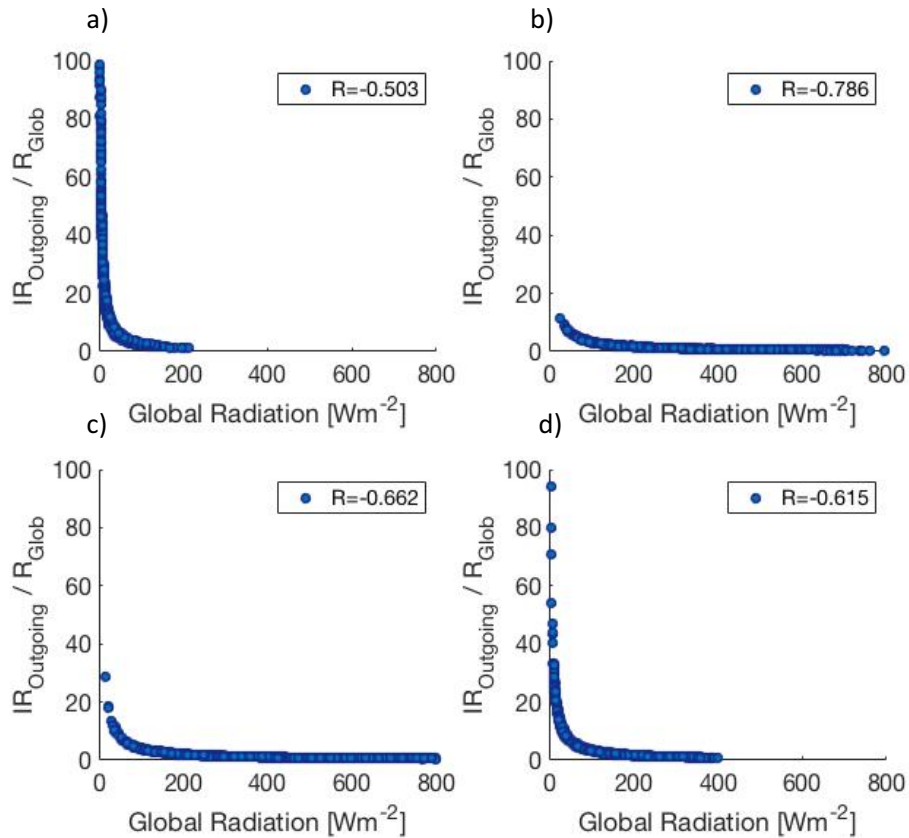
Figure 33 The dependency between the ratio of outgoing infrared radiation and global radiation vs global radiation a) in January, b) in April, c) in July and d) in October.

Figure 34 represents the monthly median values of the ratio between outgoing IR radiation and global radiation. The time series covers years 2010 to 2016. Because the incoming and outgoing IR radiation are measured with the same instrument also the January 2012 and 2013 and April 2012 and 2016 are missing for outgoing IR radiation due to the insufficient amount of measurement points. Similarly to the previously shown figure for incoming IR radiation (Figure 32), the annual fluctuation is great in January and in October, but the variation is not statistically significant because the error bars overlap. The conditions are very stable in April and in July as the ratio remains close to 1. The mean and median values of the ratio are 15.81 and 9.45 in January, 1.46 and 0.93 in April, 1.33 and 0.91 in July and 5.19 and 2.83 in October. The monthly median values in January and October differ significantly from the values in April and July.

The infrared radiation emitted by the surface depends on the temperature, emissivity and absorbance properties of the surface (Pashiardis et al., 2017). Temperature of the Earth's surface follows the surface air temperature with a delay. The emissivity term of a surface is unity for a blackbody, but in reality the surface emissivity terms are less than unity. The accurate estimation of surface emissivity

terms is difficult, because of the surface reflections, microscopic heterogeneity and surface geometry. The emissivity term shows also both angular and wavelength dependence (Feldman et al., 2014).
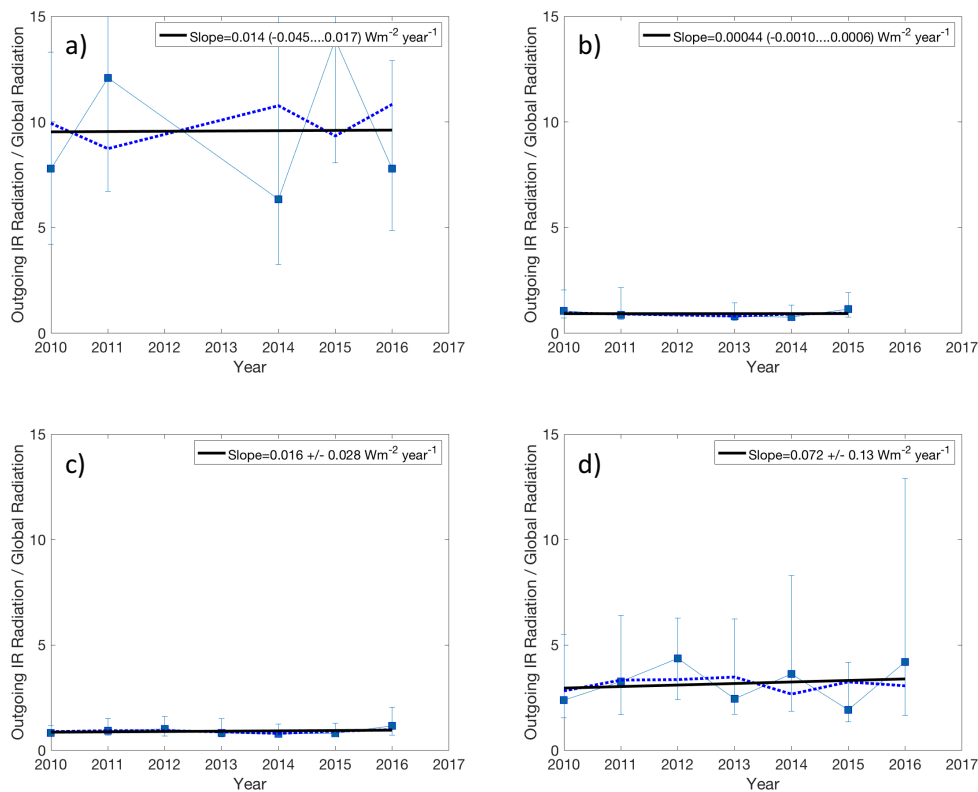

Figure 34 The monthly median value of the ratio between outgoing IR radiation and global radiation a) in January, b) in April, c) in July and d) in October. The blue boxes represent the monthly median values, the blue dashed line is the three-year-sliding average and the black solid line is the trend line. Variation for the monthly median values is presented with the error bars.

The radiation emitted by the Earth's surface and lower atmosphere is higher than the radiation emitted by the atmosphere and clouds during all of the seasons. This means that net longwave radiation (downward longwave radiation – upward longwave radiation) is negative during all seasons. There is more variation between the minimum and maximum monthly median values for incoming than outgoing IR radiation. Incoming IR radiation is highly dependent on clouds, which show great spatial and temporal variability whereas outgoing IR radiation depends on the properties of the surface which do not vary that much in time. Majority of the longwave radiation emitted by the Earth's surface and lower atmosphere is absorbed by molecules and clouds above. Especially ice clouds have been proven to have a large effect on infrared radiation (Harries et al., 2008). They re-emit it to space and back to the Earth's surface. Because their temperature is lower than the objects that initially emitted the radiation, less radiation is able to escape to space.

Upward longwave radiation is the main term balancing incoming shortwave radiation in the Earth's radiation balance. The role of upward infrared radiation on radiation budget, cooling rates and effects

on other climate variables has not been studied as much as the other parameters in the radiation budget (Feldman et al., 2014). Because Earth's surface, atmosphere and clouds emit infrared radiation and greenhouse gases and clouds absorb it, the wavelength band is used for remote sensing to study the composition of the atmosphere (Harries et al., 2008).

6. Conclusions

This study is an analysis of the different radiation parameters and cloud occurrence measured at SMEAR II station in Hyytiälä, Finland. Seasonal and annual trends of different radiation parameters were compared with cloud occurrence at the station based on the cloud base height measurements from a ceilometer.

6.1 Cloud occurrence

Even though the measurement period is short, typical pattern in the cloud occurrence can be seen for investigated years. Monthly cloud occurrence at the measurement station varied from 50 % to 90 %. The lowest cloud occurrences are measured during late spring and summer (May to August) and the highest during winter time. The minimum value of 31 % was found measured in August 2015 and the maximum valued of 94 % in December 2017. Low clouds (located less than 400 m above the ground) dominate during all of the seasons. The frequency of higher cloud base height systems increases towards the summer. The frequency of higher clouds is underestimated, because ceilometer cannot detect higher clouds that are disguised by the lower clouds. Out of the cases when at least one cloud layer was detected, around 90 % were recorded as single layer, 10 % were 2-layered and 0.5 % were 3-layered systems.

6.2 Radiation parameters

6.2.1 Trend lines

The radiation parameters and the ratios of the radiation parameters investigated in this study did not show any statistically significant trend lines. For some of the parameters like the fraction of UV-B radiation, the slopes are rather steep in January and in October, but the 95 % confidence intervals did not show any statistically significant trends.

6.2.2 Annual variation

The time series of all the individual radiation parameters in this study show annual fluctuation year-round. The fluctuation is greater in April and in July due to the higher values of the incoming solar radiation. The annual variation is not statistically significant. All of the radiation parameters in this

study are dependent on the incoming global radiation, which shows annual fluctuation year-round at the SMEAR II station.

Cloud occurrence is the key factor causing the annual fluctuation of the diffuse fraction of global radiation and of the ratios PAR, UV-A radiation and incoming IR radiation to global radiation. The ratios PAR, UV-A radiation and incoming IR radiation to global radiation are also influenced by the water vapour content of the atmosphere. The annual fluctuation of the diffuse fraction of global radiation is great during spring and summer, when the increased solar radiation contributes to the formation of convective clouds. The fraction varies between 0.2 and 0.9 during in April and July while it remains above 0.45 in January. October has been very cloudy on average as the fraction alters between 0.9 and 1.05 during the whole time period. The monthly fluctuation around the monthly median values is great during all of the investigated months. The ratio PAR to global radiation shows great annual fluctuation in January. Similar results can be seen for October. However, the error bars overlap thus the annual variation is not statistically significant. Though the conditions are rather stable in April and in July, there can be seen statistically significant annual variation.

For the fraction of UV-A radiation the annual fluctuation is great in January, April and October. The monthly fluctuation around monthly median values within each year is also high in January and in October. However, the variation is not statistically significant. The monthly median values of the fraction of UV-A radiation have remained relatively stable in July. Incoming IR radiation shows annual fluctuation in January. The conditions are more stable in April July and October.

The changing surface properties especially snow cover during winter time has a great influence on albedo, the fraction of PAR below canopy and the ratio outgoing IR to global radiation. The foliage growth is also important for albedo and the fraction of PAR below canopy during growing season. Albedo at the SMEAR II station shows statically significant variation between 0.20-0.46 in January. The conditions are more stable in April, July and October as the albedo varies between 0.095 and 0.13 during snow-free season. The fraction of PAR below canopy shows annual fluctuation year-round, but the variation is not statistically significant. The different instruments measuring PAR below canopy show slightly differentiating results, because of the surrounding vegetation is different for different instruments. Though there is annual fluctuation in January and in October, the annual variation is not statistically significant for any of the investigated months for the ratio between outgoing IR radiation and global radiation.

The annual variation of the fraction of UV-B radiation is due to changing aerosol load, cloudiness, stratospheric and tropospheric ozone concentration. The annual variation is statistically significant in

January, April and July. In October the error bars overlap therefor the annual variation is not significant. Fluctuation within each year is rather small for the fraction of UV-B radiation.

6.2.3 Seasonal variation

The individual radiation parameters show that April and July differ statistically from January and October due to the higher values of incoming solar radiation during spring and summer. Seasonal pattern of global radiation is pronounced in Finland. The monthly median values for global radiation at the SMEAR II station are 26.1 Wm^{-2} in January, 396.6 Wm^{-2} in April, 476.4 Wm^{-2} in July and 99.8 Wm^{-2} in October.

The seasonal variation of diffuse fraction of global and the ratios UV-A radiation and incoming IR radiation to global radiation are mainly due to the same reasons as annual variation; the occurrence of clouds and the frequency of specific cloud types. The fractions of incoming IR and UV-A radiation depend also on the water vapour content of the atmosphere. Some of the investigated years show statistically significant seasonal variation for the diffuse fraction of global radiation. During autumn and winter the majority of clouds are associated with frontal systems, which lead to high values of the diffuse fraction of global radiation are more frequent in January/October than in April/July. The median values for the diffuse fraction of global radiation at the SMEAR II station are 0.76 in January, 0.58 in April, 0.54 in July and 0.97 in October. The seasonal variation is not statistically significant for the fraction of UV-A radiation. The monthly median values are typically higher in January than during other investigated months, however the error bars are also greater. The cloud occurrence at the measurement station is the highest during winter time which coincides with the time when the highest values of the fraction of UV-A radiation are measured. On the other hand, in April the cloud occurrence is lower and the water vapour content of the atmosphere is very low after winter, which explains the low values of the fraction in April. The monthly median values of the ratio between UV-A radiation and global radiation are 7.82 % in January, 5.80 % in April, 6.28 % in July and 6.60 % in October. The ratio incoming IR to global radiation shows that January and October differ significantly from April and July. The high values of the ratio in January and October are explained with the high cloud occurrence and on the other hand low values of global radiation. The mean and median values of the ratio between incoming IR radiation and global radiation are 15.21 and 9.03 in January, 1.34 and 0.81 in April, 1.22 and 0.79 in July and 4.95 and 2.57 in October.

The seasonal cycle of the ratio of PAR and UV-B radiation to global radiation are dependent on the solar zenith angle and climatic conditions. The smaller wavelengths are more influenced by the scattering processes when the solar zenith angle is high. The seasonal variation is not statistically

significant for the ratio PAR to global radiation. The monthly median values are typically higher in January than during other investigated months, but the error bars are also greater. The median values for the ratio PAR to global are 2.00 μmol J^{-1} in January, 2.00 μmol J^{-1} in April, 2.05 μmol J^{-1} in July and 2.05 μmol J^{-1} in October. The seasonal variation of the fraction of UV-B radiation is more pronounced before year 2005. After that the increasing monthly median values in January and October reduces the seasonal differences. The seasonal pattern of UV-B radiation is also influenced by stratospheric and tropospheric ozone, clouds and scattering processes. The median values for the fraction of UV-B radiation are 0.18 % in January, 0.26 % in April, 0.35 % in July and 0.24 % in October. Because global radiation measured at the SMEAR II station does not cover the wavelength band of UV-B radiation completely, the actual fractions are somewhat smaller.

The seasonal cycles of albedo, the fraction of PAR below canopy and outgoing IR are also dependent on the snow cover and foliage growth in the forest. For all of the three ratios the monthly median values of albedo show that January differs significantly from the other investigated months. The median values of albedo are 0.294 in January, 0.126 in April, 0.117 in July and 0.126 in October. The median values of the fraction PAR below canopy are 0.197 in January, 0.260 in April, 0.224 in July and 0.219 in October. The ratio outgoing IR to global radiation differs significantly in January and October. The mean and median values of the ratio are 15.81 and 9.45 in January, 1.46 and 0.93 in April, 1.33 and 0.91 in July and 5.19 and 2.83 in October. The dependency between the fraction of PAR below canopy and the diffuse fraction of global radiation showed a linear trend in April, July and October indicating that the fraction of PAR below canopy increases as the cloud cover blocking the solar radiation increases.

6.3 Future work

The importance of long-term radiation measurements around the globe is crucial to study the changes in the Earth's radiation budget. It was shown in this study that many of the radiation parameters show great annual variability, thus even longer time series are needed to investigate the possible changes in radiation parameters. The instrumentation measuring radiation should be improved so that the measurements are reliable during winter when the incoming solar radiation is very low at high latitudes.

Better detection of different cloud types and their occurrence is crucial for climatological issues. Ground measurement should be used together with man-made and satellite observations in order to detect all cloud types. It is important to know more specifically the climatology of different cloud

types as their effect on radiation transfer varies. Better knowledge of the processes in which clouds participate and the possible masking effect of clouds should be studied more.

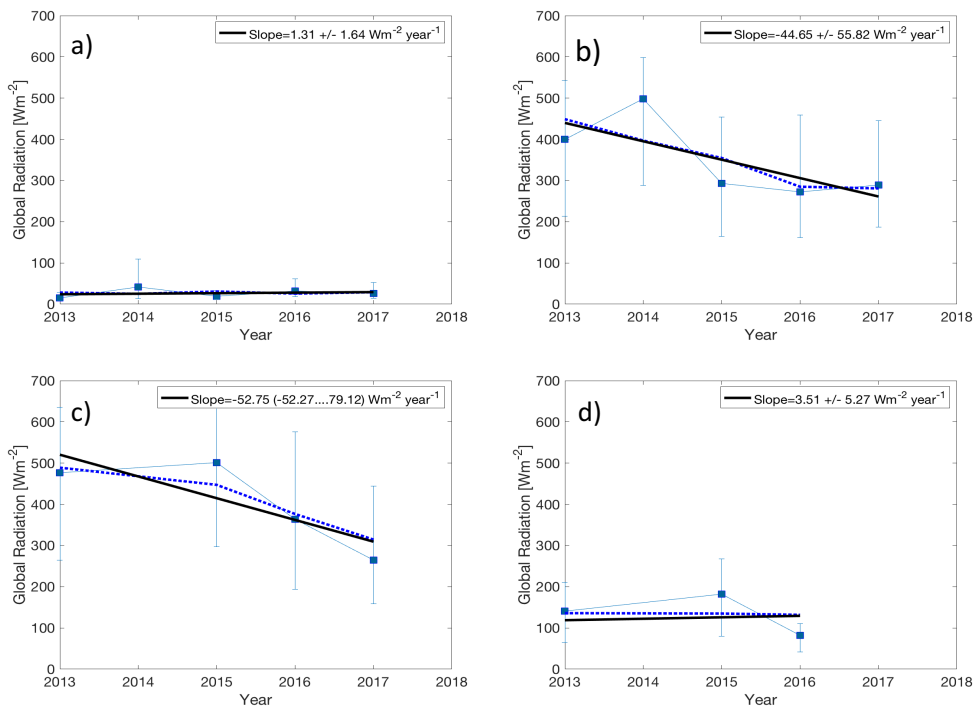# 7. Appendices

7.1 Global Radiation

Figure 34 The time series of global radiation measured 127 m above the ground a) in January, b) in April, c) in July and d) in October. The blue boxes represent the monthly median values, the blue dashed line is the three-year-sliding average and the black solid line is the trend line. Variation for the monthly
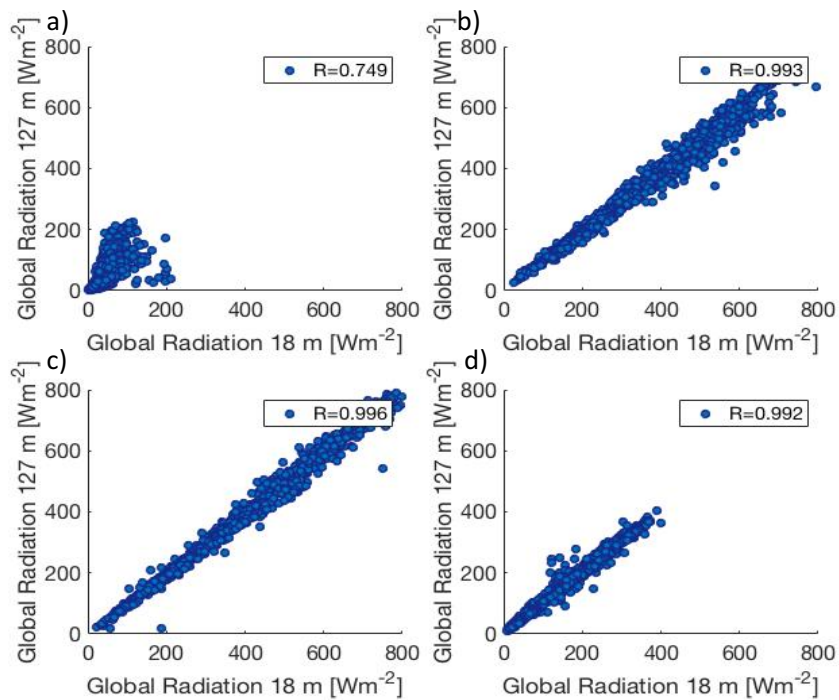

Figure 35 The dependency between global radiation measured at 18 m (x-axis) and 127 m (y-axis) a) in January, b) in April, c) in July and d) in October.

7.2 Diffuse global radiation
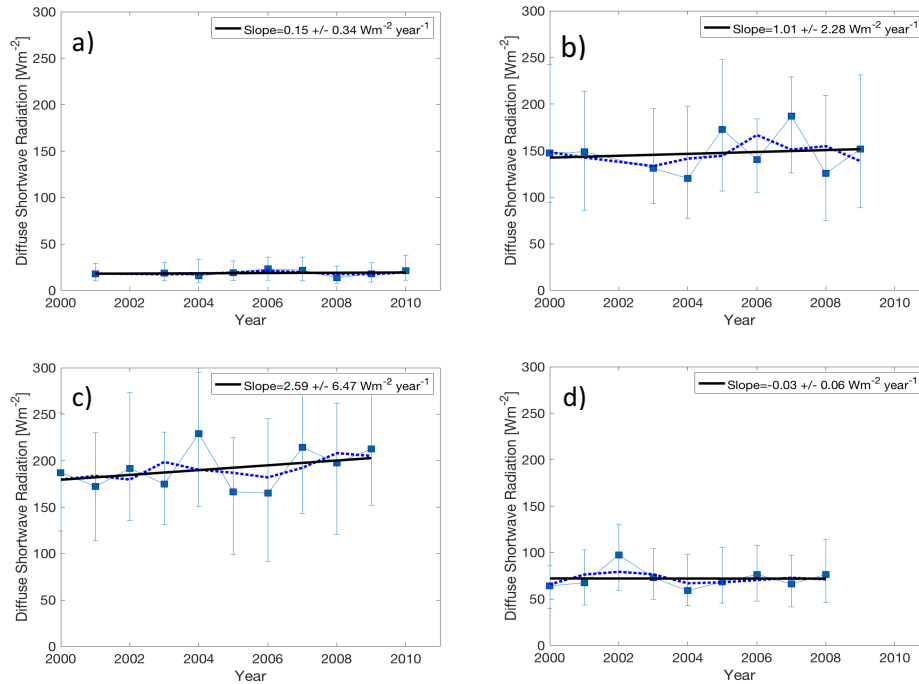
Figure 36 The time series of diffuse global radiation a) in January, b) in April, c) in July and d) in October. The blue boxes represent the monthly median values, the blue dashed line is the three-year-sliding average and the black solid line is the trend line. Variation for the monthly median values is presented with the error bars.

7.2 Reflected global radiation
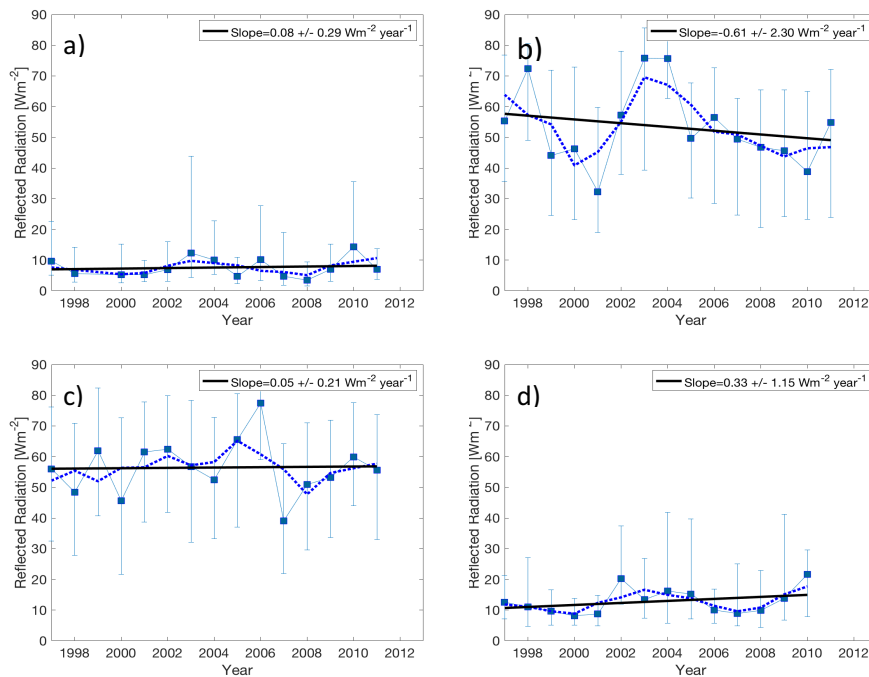
Figure 37 The time series of reflected global radiation measured at 127 m a) in January, b) in April, c) in July and d) in October. The blue boxes represent the monthly median values, the blue dashed line is the three-year-sliding average and the black solid line is the trend line. Variation for the monthly median values is presented with the error bars.
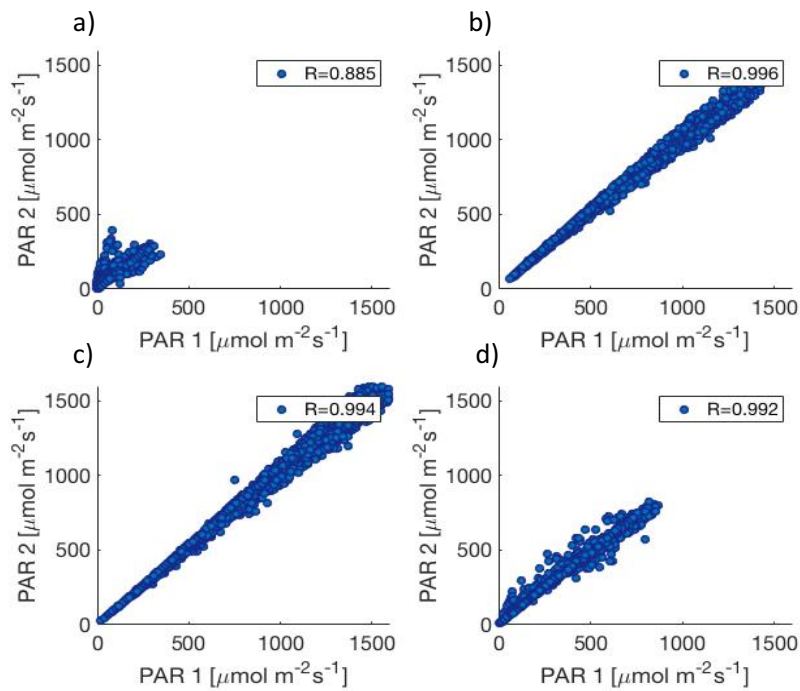
7.4 Photosynthetically Active Radiation
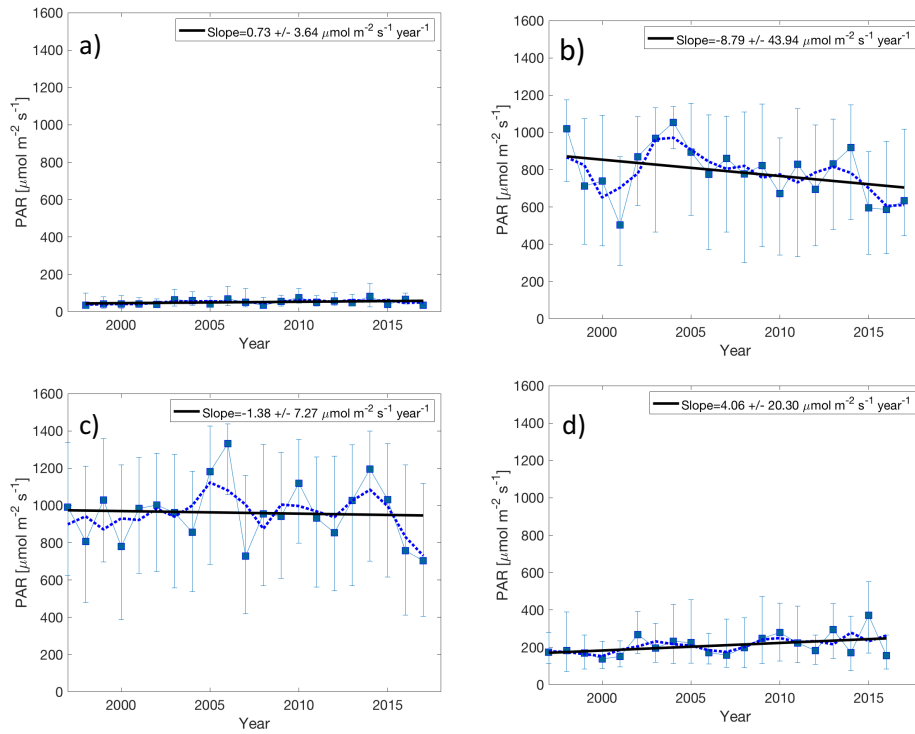
Figure 38 Time series of PAR a) in January, b) in April, c) in July and d) in October. The blue boxes represent the monthly median values, the blue dashed line is the three-year-sliding average and the black solid line is the trend line. Variation for the monthly median values is presented with the error bars.
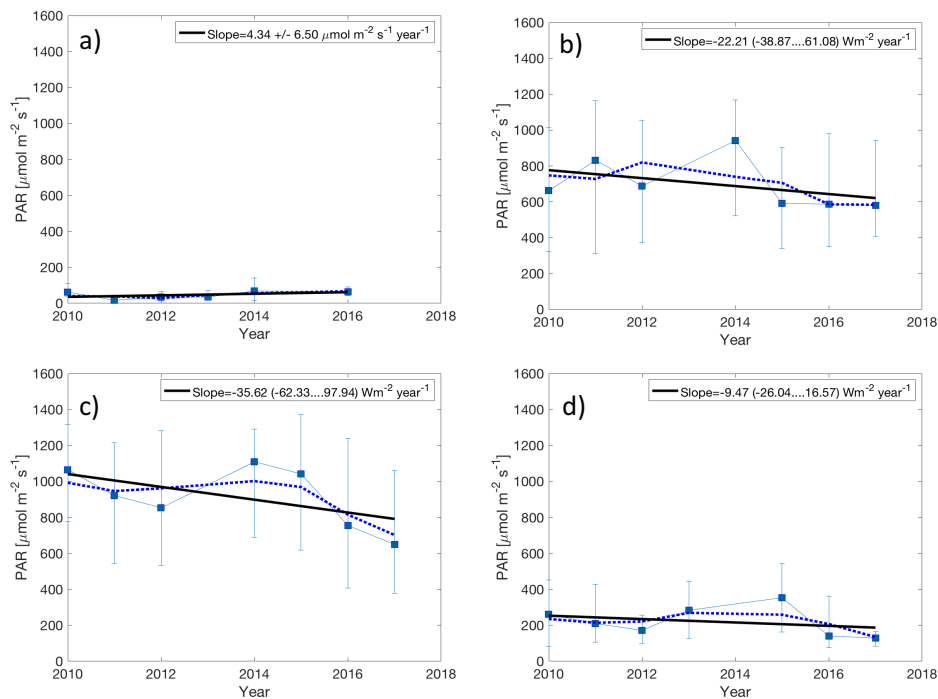
Figure 39 Time series of PAR 2 a) in January, b) in April, c) in July and d) in October. The blue boxes represent the monthly median values, the blue dashed line is the three-year-sliding average and the black solid line is the trend line. Variation for the monthly median values is presented with the error bars.

Figure 40 The dependency between instruments PAR 1 (x-axis) and PAR 2 (y-axis) a) in January, b) in April, c) in July and d) in October.

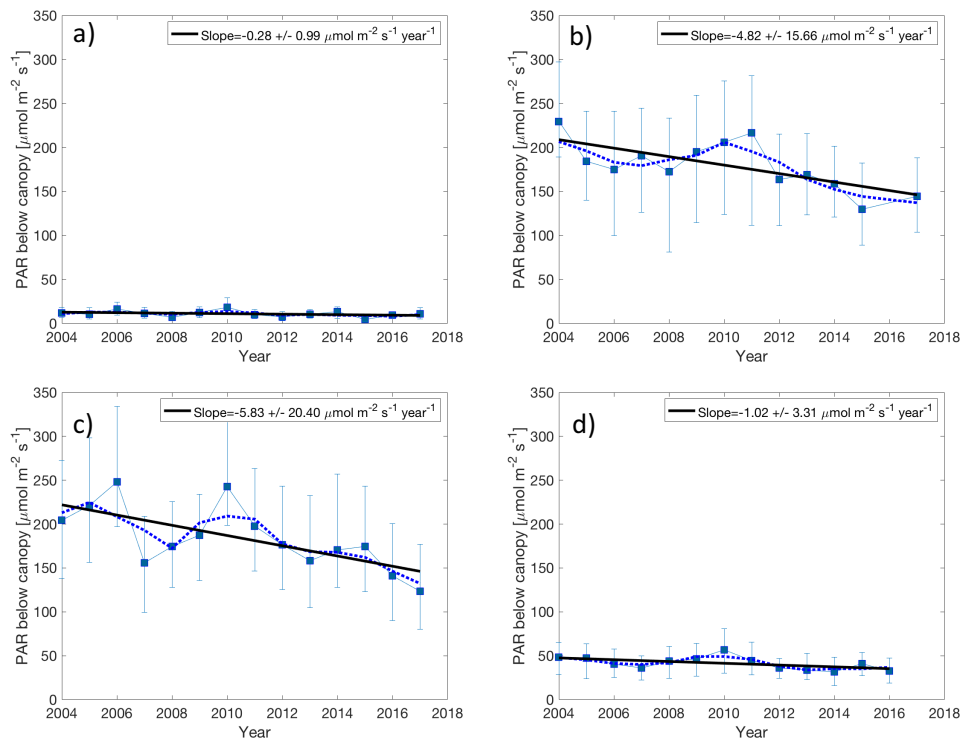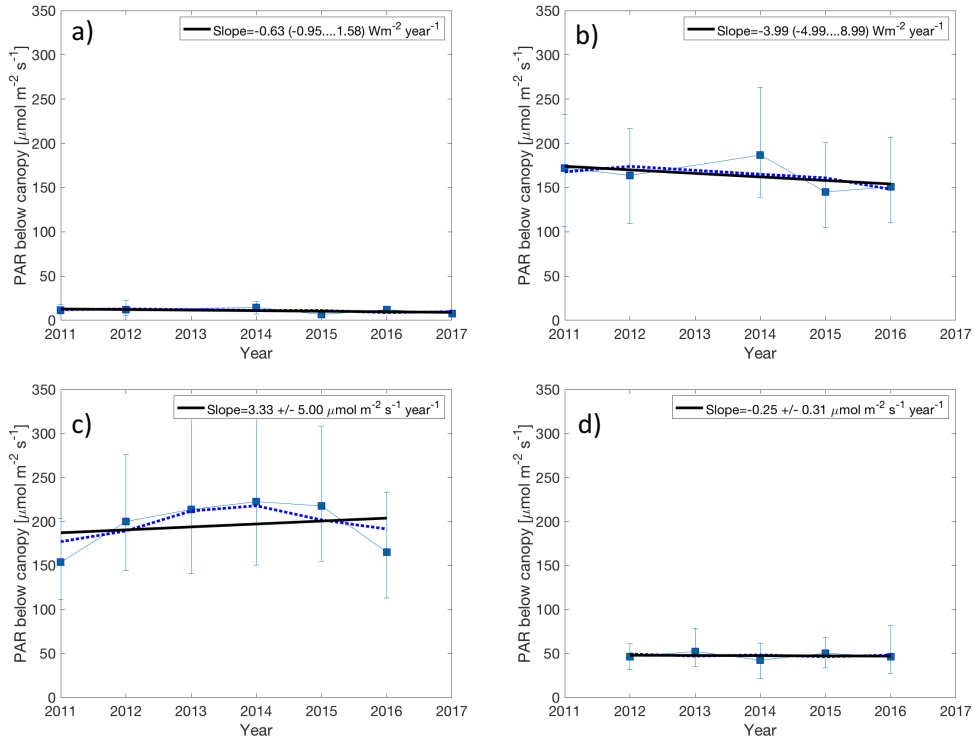## 7.5 Photosynthetically Active Radiation below canopy

Figure 41 The time series of PAR below canopy a) in January, b) in April, c) in July and d) in October. The blue boxes represent the monthly median values, the blue dashed line is the three-year-sliding average and the black solid line is the trend line. Variation for the monthly median values is presented with the error bars.
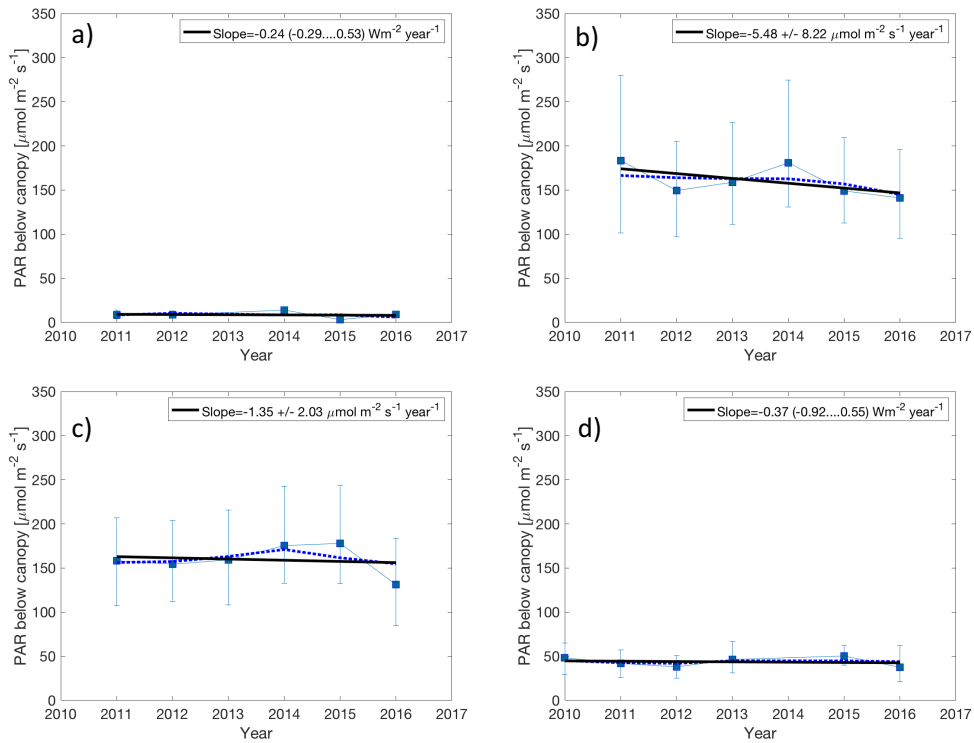
Figure 42 The time series of PAR below canopy 2 a) in January, b) in April, c) in July and d) in October. The blue boxes represent the monthly median values, the blue dashed line is the three-year-sliding average and the black solid line is the trend line. Variation for the monthly median values is presented with the error bars.
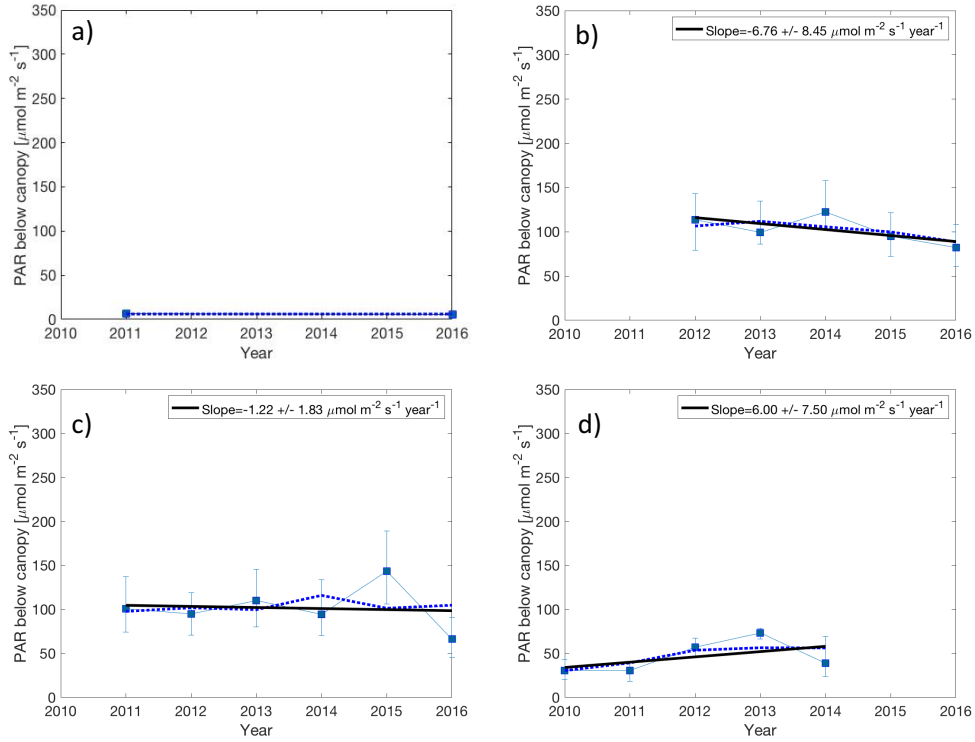

Figure 43 The time series of PAR below canopy 3 a) in January, b) in April, c) in July and d) in October. The blue boxes represent the monthly median values, the blue dashed line is the three-year-sliding average and the black solid line is the trend line. Variation for the monthly median values is presented with the error bars.

Figure 44 The time series of PAR below canopy 4 a) in January, b) in April, c) in July and d) in October. The blue boxes represent the monthly median values, the blue dashed line is the three-year-sliding average and the black solid line is the trend line. Variation for the monthly median values is presented with the error bars.
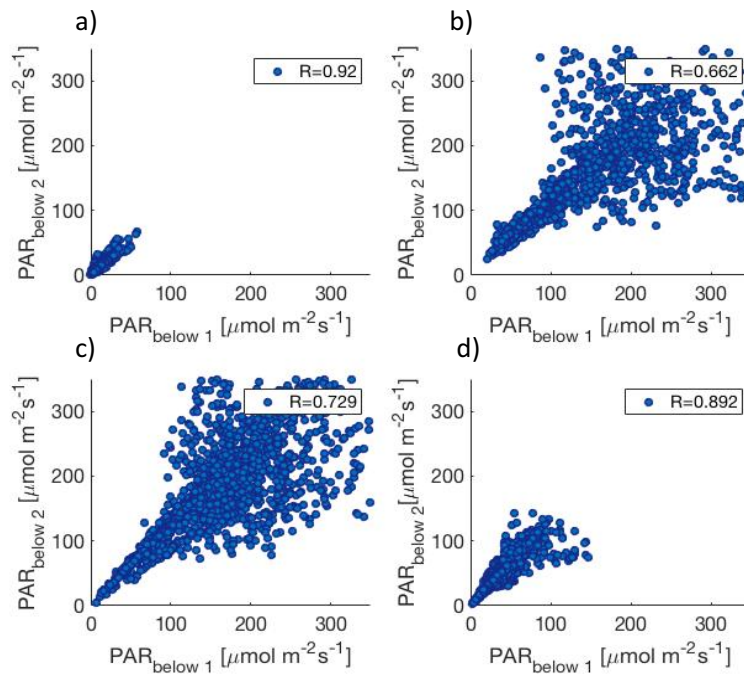

Figure 45 The dependency between instruments PAR below canopy 1 (x-axis) and PAR below canopy 2 (y-axis) a) in January, b) in April, c) in July and d) in October.
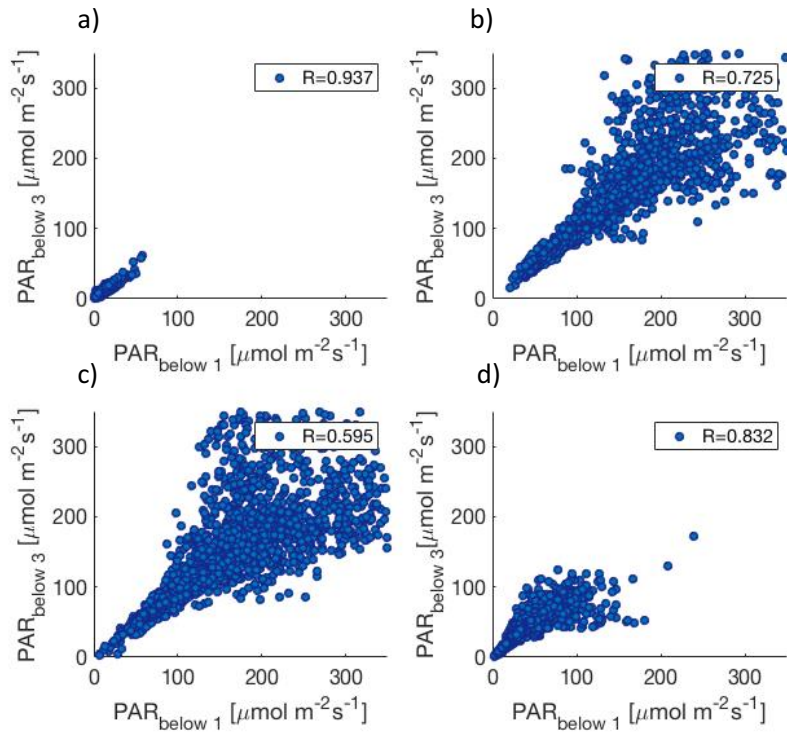
Figure 46 The dependency between instruments PAR below canopy 1 (x-axis) and PAR below canopy 3 (y-axis) a) in January, b) in April, c) in July and d) in October.
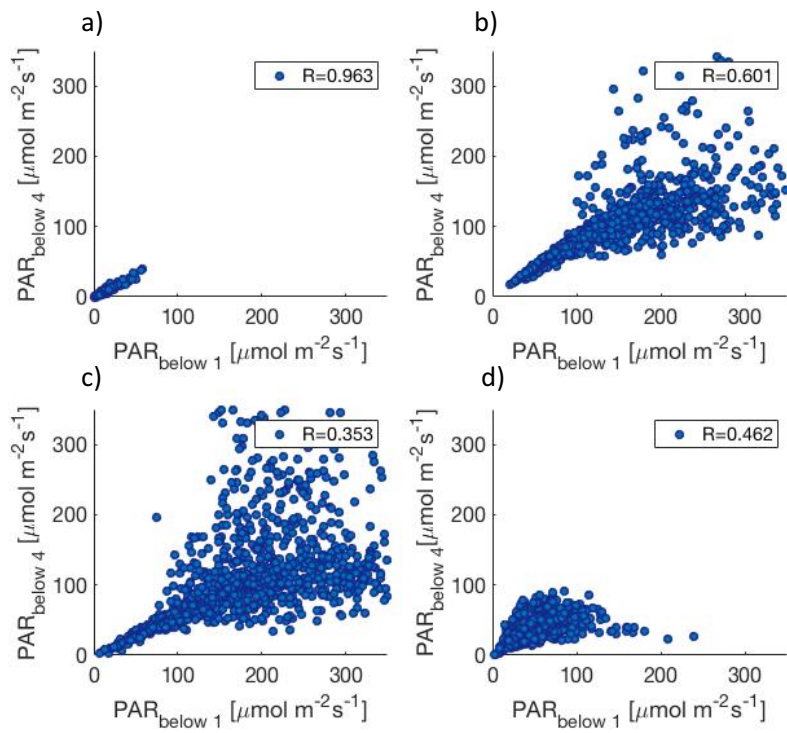

Figure 47 The dependency between instruments PAR below canopy 1 (x-axis) and PAR below canopy 4 (y-axis) a) in January, b) in April, c) in July and d) in October.
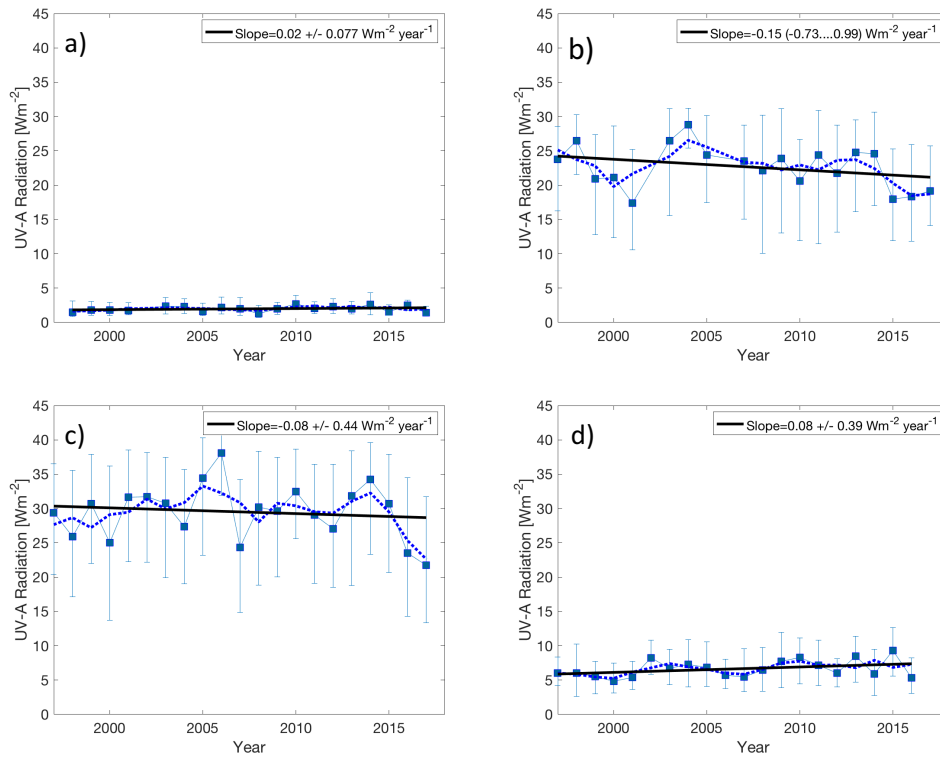
7.6 UV-A Radiation

Figure 48 The time series of UV-A radiation a) in January, b) in April, c) in July and d) in October. The blue boxes represent the monthly median values, the blue dashed line is the three-year-sliding average and the black solid line is the trend line. Variation for the monthly median values is presented with the error bars.
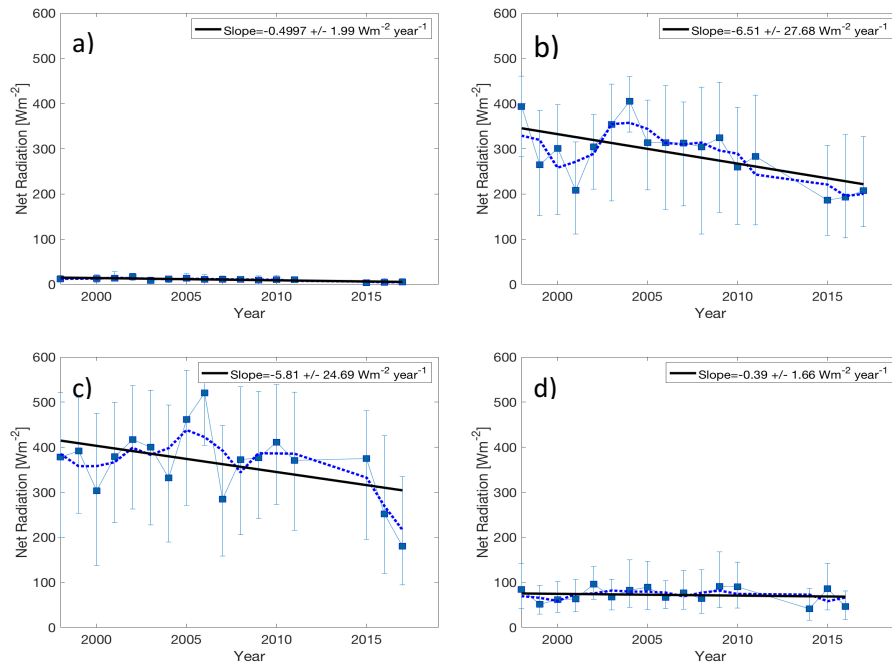
7.7 Net Radiation

Figure 49 The time series of net radiation a) in January, b) in April, c) in July and d) in October. The blue boxes represent the monthly median values, the blue dashed line is the three-year-sliding average and the black solid line is the trend line. Variation for the monthly median values is presented with the error bars.

References

Alados, I., Foyo-Moreno, I., & Alados-Arboledas, L. (1996). Photosynthetically active radiation: Measurements and modelling. *Agricultural and Forest Meteorology, 78*, 121-131.

Ambach, W., Blumthaler, M., & Wendler, G. (1991). A comparison of ultraviolet radiation measured at an arctic and an alpine site. *Solar Energy, 47*(2), 121-126.

Betts, A. K., & Ball, J. H. (1997). Albedo over the boreal forest. *Journal of Geophysical Research, 102*(28), 901-909.

Boucher, O., Randall, D., Artaxo, P., Bretherton, C., Feingold, G., Forster, P., . . . Zhang, X. Y. (2013). *Contribution of Working Group I to the Fifth Assessment Report of the Intergovernmental Panel on Climate Change. [Stocker, T. F., D. Qin, G.-K. Plattner, M. Tignor, S. K. Allen J. Boschung, A. Nauels, Y. Xia, V. Bex and P. M. Midgley (eds.)]* Cambridge University Press, Cambridge, United Kingdom and New York, NY, USA.

Brash, D., Rudolph, J., Simon, J., Lin, A., McKenna, G., Baden, H., . . . Pontén, J. (1991). A role for sunlight in skin cancer: UV-induced p53 in squamous cell carcinoma. *Proceedings of the National Academy of Sciences of the United States of America, 88*, 10124-10128.

Brühl, C., & Crutzen, P. J. (1989). On the disproportionate role of tropospheric ozone as a filter against solar UV-B radiation. *Geophysical Research Letters, 16*(7), 703-706.

Bryant, E. (1997). *Climate processes and change* Cambridge Univ. Press, New York.

Calbó, J., Pagès, D., & González, J. (2005). Empirical studies of cloud effects on UV radiation: A review. *Reviews of Geophysics, 43*

Costa-Surós, M., Calbó, J., González, J. -., & Martin-Vide, J. (2013). Behaviour of cloud base height from ceilometer measurements. *Atmospheric Research, 127*, 64-76.

Cubasch, U., Wuebbles, D., Chen, D., Facchini, M. C., Frame, D., Mahowald, N., & Winther, J. (2013). Introduction. in: *climate change 2013: The physical science basis. Contribution of Working Group I to the Fifth Assessment Report of the Intergovernmental Panel on Climate Change [Stocker, T. F., D. Qin, G.-K. Plattner, M. Tignor, S. K. Allen J. Boschung, A. Nauels, Y. Xia, V. Bex and P. M. Midgley (eds.)]* Cambridge University Press, Cambridge, United Kingdom and New York, NY, USA.

Ebrahimi, S., & Marshall, S. J. (2015). Parametrization of incoming longwave radiation at glacier sites in the Canadian Rocky Mountains. *Journal of Geophysical Research: Atmospheres, 120*, 12,536-12,556.

Feldman, D., Collins, W., Pincus, R., Huang, X., & Chen, X. (2014). Far-infrared surface emissivity and climate. *Earth, Atmospheric and Planetary Sciences, 111*(46), 16297–16302.

Fiscus, E., & Booker, F. (1995). Is increased UV-B a threat to crop photosynthesis and productivity? *Photosynthesis Research, 43*(2)

FMI (Finnish Meteorological Institute). (2018a). Climate guide. Retrieved from https://ilmasto-opas.fi/en/ilmastonmuutos/suomen-muuttuva-ilmasto/-/artikkeli/1c8d317b-5e65-4146-acda-f7171a0304e1/nykyinen-ilmasto-30-vuoden-keskiarvot.html

FMI (Finnish Meteorological Institute). (2018b). Snow statistics. Retrieved from http://en.ilmatieteenlaitos.fi/snow-statistics

FMI (Finnish Meteorological Institute). (2018c). Temperature and precipitation maps from 1961 onwards. Retrieved from http://en.ilmatieteenlaitos.fi/maps-from-1961-onwards

Frederick, J. E., Snell, H. E., & Haywood, E. K. (1989). Solar ultraviolet radiation at the earth's surface. *Photochemistry and Photobiology, 50*(8), 443-450.

Guo, J., Tilgner, A., Yeung, C., Wang, Z., Louie, P. K. K., Luk, C. W. Y., . . . Wang, T. (2014). Atmospheric peroxides in a polluted subtropical environment: Seasonal variation, sources and sinks, and importance of heterogeneous processes *Environmental Science and Technology, 48*, 1443-1450.

Hansen, J., Sato, M., Kharecha, P., & von Schuckmann, K. (2011). Earth's energy imbalance and implications. *Atmos. Chem. Phys, 11*, 13421-13449.

Hari, P., & Kulmala, M. (2005). Station for measuring ecosystem-atmosphere relations (SMEAR II). *Boreal Environment Research, 10*

Harries, J., Carli, B., Rizzi, R., Mlynczak, M., Palchetti, L., Maestri, T., . . . Masiello, G. (2008). The far-infrared earth. *Rev. Geophys., 46*.

Hartmann, D. L. (2016). *Global physical climatology* (2.th ed.). Amsterdam, Netherlands and Oxford, UK: Elsevier.

Inman, R., Chu, Y., & Coimbra, C. (2016). Cloud enhancement of global horizontal irradiance in California and in Hawaii. *Solar Energy, 130*, 128-138.

Iqbal, M. (1983). *Introduction to solar radiation*. New York and London: ACADEMIC PRESS, INC.

Karvosenoja, N., & Johansson, M. (2003). Primary particulate matter emissions and the Finnish climate strategy. *Boreal Environment Research, 8*, 125-133.

Kerr, J. B. (2005). Understanding the factors that affect surface ultraviolet radiation. *Optical Engineering, 44*(4)

Kerr, J. B., & McElroy, C. T. (1993). Evidence for large upward trends of ultraviolet-B radiation linked to ozone depletion.*262* (Science)

Kopp, G., & Lean, J. L. (2011). A new, lower value of total solar irradiance: Evidence and climate significance. *Geophysical Research Letters, 38*(1).

Kulmala, M., Rannik, Ü, Pirjola, L., Dal Maso, M., Karimäki, J., Asmi, A., . . . Vesala, T. (2000). Characterization of atmospheric trace gases and aerosol concentrations at forest sites in southern and northern Finland using back trajectories. *Boreal Environment Research, 5*, 315-336.

Lawrence, M. G., Jöckel, P., & von Kuhlmann, R. (2001). What does the global mean OH concentration tell us? *Atmos. Chem. Phys, 1*, 37-49.

Liou, K. N. (2002). *An introduction to atmospheric radiation* (2nd ed.). San Diego, California, USA and London, UK.: Academic Press.

Loeb, N., Wielicki, B., Doelling, D., Smith, L., Keyes, D., Kato, S., . . . Wong, T. (2009). Toward optimal closure of the earth's top-of-atmosphere radiation budget. *Journal of Climate, 22*, 748-766.

Lohmann, U., Leichter, J., Penner, J. E., & Leaitch, R. (2000). Indirect effect of sulphate and carbonaceous aerosols: A mechanism treatment. *J. Geophys. Res, 105*, 12,193-12,206.

Madronich, S., & Flocke, S. (1999). The role of solar radiation in atmospheric chemistry. in: Boule P. (eds) Environmental photochemistry. The handbook of environmental chemistry (reactions and processes). (2nd ed.). Berlin: Springer.

Mishchenko, M. I., Geogdzhayev, I. V., Rossow, W. B., Cairns, B., Carlson, B. E., Lacis, A. A., . . . Travis, L. D. (2007). Long-term satellite record reveals likely recent aerosol trend. *Science, 315*, 1543.

Monks, P. S., Archibald, A. T., Colette, A., Cooper, O., Coyle, M., Derwent, R., . . . Williams, M. L. (2015). Tropospheric ozone and its precursors from the urban to the global scale from air quality to short-lived climate forcer. *Atmos. Chem. Phys, 15*, 8889-8973.

Myhre, G., Shindell, D., Bréon, F., Collins, W., Fuglestvedt, J., Huang, J., . . . Zhang, H. (2013). Anthropogenic and natural radiative forcing. in: *Climate Change 2013: The Physical Science Basis. Contribution of Working Group I to the Fifth Assessment Report of the Intergovernmental Panel on Climate Change [Stocker, T. F., D. Qin, G.-K. Plattner, M. Tignor, S. K. Allen J. Boschung, A. Nauels, Y. Xia, V. Bex and P. M. Midgley (eds.)]* Cambridge University Press, Cambridge, United Kingdom and New York, NY, USA.

Nakajima, T., Higurashi, A., Kawamoto, K., & Penner, J. E. (2001). A possible correlation between satellite-derived cloud and aerosol microphysical parameters. *Geophys.Res.Lett., 28*(7), 1171-1174.

NASA (National Aeronautics and Space Administration). (2017). The sunspot cycle. Retrieved from https://solarscience.msfc.nasa.gov/images/Zurich_Color_Small.jpg

Pashiardis, S., Kalogirou, S. A., & Pelengaris, A. Characteristics of longwave radiation through the statistical analysis of downward and upward longwave radiation and inter-comparison of two sites in Cyprus. *Journal of Atmospheric and Solar-Terrestrial Physics, 164* (2017), 60-80.

Pawson, S., Steinbrecht, W. (A., Fujiwara, M., Karpechko, A. Y., Petropavlovskikh, I., Urban, J., & Weber, M.) (2014). Update on global ozone: Past, present, and future. *Chapter 2 in Scientific Assessment of Ozone Depletion: 2014, Global ozone research and monitoring project – report no. 55*. World Meteorological Organization, Geneva, Switzerland.

Riuttanen, L., Hulkkonen, M., Dal Maso, M., Junninen, H., & Kulmala, M. (2013). Trajectory analysis of atmospheric transport of fine particles, SO_2, NO_x and O_3 to the SMEAR II station in Finland in 1996-2008. *Atmos. Chem. Phys, 13*, 2153-2164.

Romer, P. S., Duffey, K. C., Wooldridge, P. J., Edgerton, E., Baumann, K., Feiner, P. A., . . . Cohen, R. C. (2018). Effects of temperature-dependent NO_x emissions on continental ozone production. *Atmos. Chem. Phys, 18*, 2601-2614.

Scott, C. E., Monks, S. A., Spracklen, D. V., Arnold, S. R., Forster, P. M., Rap, A., . . . Wilson, C. (2018). Impact on short-lived climate forcers increases projected warming due to deforestation. *Nature Communication, 9*, 157.

Seinfeld, J., & Pandis, S. (Eds.). (2016). *Atmospheric chemistry and physics: From air pollution to climate change* (3rd ed.) Hoboken, New Jersey: Wiley.

Sellers, W. D. (1965). *Physical climatology* The University of Chicago Press.

Soni, V. K., Pandithurai, G., & Pai, D. S. (2012). Evaluation of long-term changes of solar radiation in India. *International Journal of Climatology, 32*, 540-551.

Stenke, A., & Grewe, V. (2005). Simulations of stratospheric water vapour trends: Impact on stratospheric chemistry. *Atmos. Chem. Phys, 5*, 1257-1272.

Stephens, G., Wild, M., Stackhouse Jr, P., L'Ecuyer, T., Kato, S., & Henderson, D. (2012). The global character of the flux downward longwave radiation. *Journal of Climate, 25*, 2329–2340. doi://doi.org/10.1175/JCLI-D-11-00262.1

Stern, D. I. (2006). Reversal of the trend in global anthropogenic sulfur emissions. *Global Environmental Change, 16*, 207-220.

Stjern, C. W., Kristjánsson, J. E., & Hansen, A. W. (2009). Global dimming and global brightening − an analysis of surface radiation and cloud cover data in Northern Europe. *International Journal of Climatology, 29*, 643-653.

Szeicz, G. (1974). Solar radiation for plant growth. *Journal of Applied Ecology, 11*(2)

Tzoumanikas, P., Nikitidou, E., Bais, A. F., & Kazantzidis, A. (2016). The effect of clouds on surface solar irradiance, based on data from an all-sky imaging system. *Renewable Energy, 95*, 314-322.

Venäläinen, A., & Heikinheimo, M. (1997). The spatial variation of long-term mean global radiation in Finland. *International Journal of Climatology, 17*, 415-426.

Vonder Haar, T. H., & Suomi, V. (1971). Measurements of the Earth's radiation budget from the satellites during a 5-year period. I. Extended time and space measurements. *Journal of Atmospheric Science, 28*, 305-314.

Wagner, T. J., & Kleiss, J. M. (2016). Error characteristics of ceilometer-based observations of cloud amounts. *Journal of Atmospheric and Oceanic Technology, 33*, 1557-1567.

Wang, K., & Dickinson, R. E. (2013). Global atmospheric downward longwave radiation at the surface from ground-based observations, satellite retrievals, and reanalyses. *Rev. Geophys., 51*, 150-185.

WMO (World Meteorological Organization). (2014). *Assessment for decision-makers: Scientific assessment of ozone depletion* (Global Ozone Research and Monitoring Project- Report No. 56 ed.). Geneva, Switzerland:

Zhao, K., & Jackson, R. B. (2014). Biophysical forcing of land-use changes from potential forestry activities in North America. *Ecological Monographs, 84*(2), 329-353.